Semiclassical theory of nonlocal plasmonic excitation in metallic nanostructures

Giuseppe Toscano
Ph.D. Thesis
August 2013

Semiclassical theory of nonlocal plasmonic excitation in metallic nanostructures

Giuseppe Toscano
Ph.D. Thesis
19. august 2013

Supervisors:

Professor N. Asger Mortensen,
Technical University of Denmark

Associate Professor Martijn Wubs,
Technical University of Denmark

Professor Antti-Pekka Jauho,
Technical University of Denmark

This thesis is submitted in partial fulfillment of the requirements for obtaining the Philosophiæ Doctor (Ph.D.) degree at the Technical University of Denmark. The work presented in this thesis was carried out at DTU Fotonik, Department of Photonics Engineering, between September 2009 and January 2013.

Abstract

This thesis deals with the theoretical study of plasmonic excitations in metallic nanostructures. The main issue that we address is the description of the free-electron gas when the size of metallic structures is of the order of 10 nm, that is comparable with the Fermi wavelength of the gas. These are the typical sizes of the nanoplasmonics structures, that can be fabricated nowadays. The model we propose is the hydrodynamic Drude model, a semiclassical model that describes the free-electron gas in a metal as a Fermi gas subject to the electromagnetic force, as defined by the Navier-Stokes like equation. New in this model is the presence of pressure waves, analogous to sound waves, that give rise to a spatially non-local optical response. We provide a theoretical derivation of the hydrodynamic equations, and we point out the main differences between the hydrodynamic model and the classical Drude model, that is commonly used in plasmonics. In particular, we show that the surface charge density has a finite thickness in the hydrodynamic model, and we discuss the correct form of the boundary conditions in the case of no electron spill-out. We present the numerical implementation of the hydrodynamic equations in COMSOL, and we apply this code to the study of a cylindrical nanowire, a cylindrical nanowire dimer, and a bow-tie dimer. The final results reveal the blueshift of the surface plasmon resonances with respect to the ones calculated with the Drude model. In a metallic dimer, much of the electromagnetic energy is confined in the gap between the structures, and this gives rise to the phenomenon of field enhancement. We show that the hydrodynamic model causes the enhancement factors to decrease significantly. The finite thickness of the surface charge layer allows us to calculate the electric field near sharp tips, where the classical model gives divergent results. We apply this concept to the study of a groove structure for SERS applications, and we evaluate the maximum enhancement factor that is possible to achieve with this structure. Finally, we present a new formulation of the hydrodynamic equation, that has the same form of the ordinary wave equation in the local model. This formulation allows us to study the propagation in plasmonic waveguides

in the hydrodynamic model. We calculate the dispersion relations for the cylindrical, V-groove, and Λ-groove waveguides. We evaluate the ultimate surface mode area for both the V-groove, and the Λ-groove, that has important implications for the understanding of the Purcell effect in spontaneous emission.

Resumé

Denne afhandling beskriver et teoretisk studie af plasmoniske excitationer i metalliske nanostrukturer. Hovedproblemet som vi adresserer, er beskrivelsen af den frie elektron gas når størrelsen af de metalliske strukturer er i omegnen af 10 nm som er sammenlignelig med gasens Fermi bølgelængde. Disse størrelser er typiske for nanoplasmoniske strukturer som kan fabrikeres på nuværende tidspunkt. Modellen vi foreslår, er en hydrodynamisk Drude model, en semi-klassisk model som beskriver den frie elektron gas af et metal som en Fermi gas påtrykt en eletromagnetisk kraft, defineret ved hjælp af et Navier-Stokes lignende udtryk. Det nye i modellen er tilstedeværelsen af trykbølger, en analog til lydbølger, som medvirker til en rumlig ikke-lokal optisk respons.

Vi fremlægger en teoretisk udledning af de hydrodynamiske ligninger og vi illustrerer hovedforskellene mellem den hydrodynamiske model og den klassiske Drude model, som ofte bliver brugt indenfor plasmoner. Særligt viser vi at overfladeladningstætheden har en endelig tykkelse i den hydrodynamiske model og vi diskuterer den korrekte form af grænsebetingelserne i tilfældet, hvor der ikke er noget elektron spill-out.

Vi præsenterer en numerisk implementering af de hydrodynamiske ligninger i COMSOL og vi anvender denne kode til at studere en cylindrisk nanowire, en cylindrisk nanowire dimer og en butterfly dimer. Resultatet viser et blåskifte af overflade plasmon resonansen i forhold til beregningen med Drude modellen. I en metallisk dimer er meget af den elektromagnetiske energi begrænset til tomrummet mellem strukturerne og det fører til fænomenet feltforstærkning. Ved at bruge den hydrodynamiske model viser vi at denne feltforstærkning reduceres betydeligt.

Den endelige tykkelse af overflade ladningslaget gør det muligt at beregne det elektriske felt nær skarpe kanter hvor den klassiske model giver divergerende resultater. Vi anvender dette koncept til at studere groove strukturer til SERS applikationer og vi evaluerer den maksimale forstærkningsfaktor, som er mulig af opnå med denne struktur.

Til sidst præsenterer vi en ny formulering af den hydrodynamiske ligning som har den samme form som den normale bølgeligning i den lokale model. Denne formulering gør det muligt at studere formering i plasmoniske bølgeledere med den hydrodynamiske model. Vi beregner dispersionsrelationen for cylindriske, V-groove og Λ-groove bølgeledere. Vi evaluerer den endelige overflade mode arealet for både V-groove og Λ-groove som har nogle vigtige implikationer for at forstå Purcell effekten i spontan emission.

Publication list

Journal papers

[A] S. Raza, **G. Toscano**, A. -P. Jauho, M. Wubs, and
N. A. Mortensen,
"Unusual resonances in nanoplasmonic structures due to non-local response",
Phys. Rev. B **84**, 121412(R) (2011).

[B] **G. Toscano**, S. Raza, A.-P. Jauho, N. A. Mortensen, and
M. Wubs,
"Modified field enhancement and extinction by plasmonic
nanowire dimers due to nonlocal response",
Opt. Express **20**, 4176 (2012).

[C] **G. Toscano**, S. Raza, S. Xiao, M. Wubs, A.-P. Jauho,
S. I. Bozhevolnyi, and N. A. Mortensen,
"Surface-enhanced Raman spectroscopy (SERS):
nonlocal limitations",
Opt. Lett. **37**, 2538 (2012).

[D] **G. Toscano**, S. Raza, W. Yan, C. Jeppesen, S. Xiao,
M. Wubs, A. -P. Jauho, S. I. Bozhevolnyi, and
N. A. Mortensen,
"Nonlocal response in plasmonic waveguiding with extreme
light confinement",
Nanophotonics **2**, 161 (2013).

[E] S. Raza, **G. Toscano**, A.-P. Jauho, N. A. Mortensen, and
M. Wubs,
"Refractive-index sensing with ultra-thin plasmonic nano-tubes",
Plasmonics **8**, 193 (2013).

Conference proceedings

[F] M. Wubs, S. Raza, **G. Toscano**, A.-P. Jauho, and
N. A. Mortensen,
"Are there novel resonances in nanoplasmonic structures due
to nonlocal response?",
Proc. SPIE **8260**, 82601E (2012).

[G] N. A. Mortensen, **G. Toscano**, S. Raza, N. Stenger, W. Yan,
and A.-P. Jauho, S. Xiao, M. Wubs,
"Nanoplasmonics beyond Ohm's law",
AIP Conf. Proc. **1475**, 28 (2012).

[H] **G. Toscano**, M. Wubs, S. Xiao, M. Yan, Z.F. Öztürk,
A.-P. Jauho, N. A. Mortensen,
"Plasmonic nanostructures: local versus nonlocal response",
Proc. SPIE **7757**, 77571T (2010).

All papers were written and published during my Ph.D. project.
Paper A, B, C, D are included and discussed in the thesis.

List of Abbreviations

HD	Hydrodynamic Model
NL	Nonlocal
LRA	Local Response Approximation
NC	Condition of Numerical Consistency
RPB	Reactive Power Balance
APB	Active Power Balance
SPP	Surface Plasmon Polaritons
HDW	Hydrodynamic wave equation
HDP	Hydrodynamic motion equation for $\mathbf{P}$
EIM	Effective-index method

Simulation Hardware and Software

All the results presented in this thesis are obtained on a personal computer equipped with four Intel 2 Ghz processors and 24 Gb of RAM.

The software used for FEM simulations is COMSOL Multiphysics 4.1a.

The software used for computing the analytical solutions is MAT-LAB.

Foreword

I remember the first time I saw Maxwell's equations on a blackboard. It was spring 2002, the sun was shining outside, and I was attending a physics class at the University of Naples. The professor wrote the equations down, and all the people in the class looked astonished. A moment of silence followed, then he turned to his four-hundred people class and said, laughing: "When I go out of the door, I will not see them anymore. Many of you will see them for the rest of their lives from now on". I felt like I was included in that group of people. Love at first sight, and from that moment Maxwell's equations followed me everywhere, at least in my mind.

At some point during my studies, I was at the University of Rome and I encountered two other beautiful subjects: "Solid State Physics" and "Fluid Dynamics". I loved those subjects too, but it seemed I could not find anything traveling at velocity of light in them! Electrons and holes looked slow, and fluids were fast, but not so fast. Thus, I said to myself: "If I find a subject that merges electromagnetism, solid state physics and fluid dynamics, this will become the research topic of my PhD!" Luckily enough, I had a friend, Jure Grgić, who was a PhD at DTU Fotonik, and he told me that his supervisor could maybe help me. I wrote to his supervisor, and he proposed me this topic straightaway: plasmonics. I was really enthusiastic! I left everything, also a PhD position at EPFL, in order to come to Denmark, and work on this topic. Jure's supervisor became my supervisor, Prof. N. Asger Mortensen, and Jure became my collegue, of course.

I still feel this enthusiasm nowadays, while writing these words, smiling, in a dark winter day. Plasmonics is a real multi-faceted topic, where you can find electromagnetism, solid state physics, fluid dynamics, quantum physics, and even chemistry at once. As we will discover, it is a new field and it is still a realm full of wonders, waiting to be explored. Everyday there are new findings, and this keeps feeding my curiosity.

If you are a student, and you are reading these pages, then I have an advice to give you: keep always your curiosity, and intellectual interests alive. Keep your mind open all the time: you can

find inspiration almost in everything. If you have these elements, motivation will follow, and your work will show the path naturally.

I have had the fortune of working in a group where all these elements are continuously nourished and nurtured. It is a very young group, and everybody is so full of energy and curiosity. There are always interesting discussions, either during ordinary meetings or just in the corridors, by the coffee machine. The doors are always open, people are always smiling and available. These are all the ingredients of a healthy scientific environment, where ideas can be born and grown.

My big thanks go to my daily supervisors Prof. N. Asger Mortensen, and Assoc. Prof. Martijn Wubs. It is mainly due to their efforts that my PhD studies flourished. Knocking on their doors could really make my day. They provided me with scientific support, but also with human support and understanding during my ups and downs, typical of our lives. It is quite rare to find people that show both scientific knowledge and humanity.

I would also like to thank my third supervisor, Prof. Antti-Pekka Jauho, for his wise suggestions, his interesting lectures on many-body quantum physics, and human support as well. I thank Søren Raza, with whom I collaborated on my project. I thank Sergey Bozhevolnyi for his great insights, for his help, and the fruitful collaborations. I would like to thank Jure Grgić, who made all this possible. I thank Sanshui Xiao, and Claus Jeppesen for the conversation we had on SERS and waveguiding. I thank Christian Agger, for his help with COMSOL and Linux.

I would like to thank Peter Norlander, Javier García de Abajo and Kristian Thygesen for taking time out of their activities for serving as evaluation committee of my thesis. I thank my colleagues Aikaterini Argyraki, and Lukasz Brewka for their helpful comments on the thesis manuscript.

Finally, I thank my parents for supporting my crazy ideas and for teaching me to live life with trust and a smile on the face.

Kongens Lyngby,
January 2013

Giuseppe Toscano

Contents

1

Motivation and plot

Everything should be made as simple as possible,
but not simpler.

Ockham's razor

"Light cannot be confined to dimensions much smaller than $\lambda/2$" (Abbe 1873 [1, 2]). This is the sentence you can read if you open your favorite classic book on optical microscopy, and it sounds like a rule carved in stone. The usual demonstration is the well-known "single-slit" experiment, that is actually very convincing: if you squeeze the slit down to a characteristic width, the light beam is not focused on the screen anymore, but it spreads into very distinct directions. This characteristic width where this occurs is actually $\lambda/2$, and the phenomenon is known as *diffraction.*

However, there is perhaps a flaw in the single-slit example..... is $\lambda/2$ the only fundamental limit to light confinement? Of course, this was the case at Abbe's time, but it is not like that any longer. In fact, in 1957, Richie predicted the existence of self-sustained collective excitations of electrons at metal surfaces, while studying energy loss of fast electrons passing through thin metal films [3, 4]. Two years later, Powell and Swan demonstrated experimentally the existence of these excitations [5, 6], that were later called *surface plasmons* [7]. We know from classical electrodynamics, that if a charge oscillates, it generates an electromagnetic field. Thus,

there is *always* an electromagnetic wave coupled with a surface plasmon, and this coupling is called *surface plasmon polariton*. Luckily enough, the electromagnetic radiation associated with a surface-plasmon excited in a metal particle of nanometer size falls into the visible or infrared spectrum region, and this gives us the answer to the previous question: focusing light beyond the diffraction limit can be achieved by means of surface-plasmons! [8,9].

Why do we want to overcome this limit? Obviously, there is a fundamental interest, and in addition there are numerous technological implications. Nowadays optical devices and interconnects are limited by the diffraction limit. The wavelength of the light is of the order of hundreds of nanometers, so the size of the optical devices is bigger than their electronic counterparts, and this limits the amount of data that can be transferred on a chip. However, the fabrication process of metallic devices allows to design structures that are crucial for the realization of fast on-chip optical communication in nanoscale integrated circuits [10]. An example of these structures is a waveguide that has been fabricated recently [11], and it is able to drive and focus light to a spot of sub-100nm scale by means of a 3D tapered geometrical structure. Squeezing light to such small areas means increasing the energy density, that is linked to the field strength. This phenomenon is called "field enhancement", and the focusing spots are known as "hot-spots".

Mathematical modeling of surface plasmon propagation is important in order to understand the fundamental processes and to support the design of the plasmonic nanostructures. Plasmon propagation can be studied by using a classical approach based on Maxwell's equations, and the dielectric function used for describing the free electrons in the metal is obtained by means of the well-known Drude model [12, 13]. This relatively simple model gives reliable results, and can be safely applied if the sizes of the metal particles D are bigger than $10\,\mathrm{nm}$ [14]. However, for smaller particle sizes, the electrons start to "feel" the boundaries of the particle, and the quantum effects due to their wave nature are anticipated. The term *"Quantum Plasmonics"* has even been introduced [15–22], and very recent experiments support new exciting physics in this regime [23–25].

In principle, a full quantum mechanical calculation is called for in this new regime [15, 26], but in practice this could involve at

most a few hundreds of atoms, that are definitely not enough to describe the behavior of more realistic plasmonic devices. Another perhaps more practical approach would be the introduction of a correction term to the Drude model that takes into account for the wave nature of the electrons. This is what actually comes out of the application of the *hydrodynamic model* of the electron gas, that was developed by Bloch in the 30s [27], and applied to optics in the 70s and 80s by Boardman [28], Fuchs [29, 30], Halevi [31] and others.

Recently, the hydrodynamic model has received considerable attention from the plasmonic research community because of its simple, yet more accurate way of describing the subnanometric features of plasmon excitations [14, 32]. Our work is based on this model, and we took an active part into the scientific discussions and investigations, that have grown rapidly in the last two years [17, 33–50] . One of our main contributions to this field was the clarification of the correct form of the hydrodynamic equation, and of the correct boundary conditions, that gave new insight into the application of this model to plasmonics [32]. Another important contribution was the implementation of a numerical code in COMSOL Multiphysics for solving 2D scattering problems with the hydrodynamic model [47, 48]. This code is open source, and the source is available to the research community at the website `www.nanopl.org`. Finally, we have just recently reported a generalized nonlocal wave equation that (without approximations) brings the hydrodynamic model onto a form closely resembling the common local response approximation wave equation [51]. This new "master wave equation" has the potential to become the new workhorse in plasmonic simulations as nonlocal effects can be included at almost no increase in computational complexity.

Last year, some behaviors predicted by the hydrodynamic model were observed experimentally, and reported in two important papers [46, 52]. The results obtained with our numerical code for scattering provided an important theoretical support for these experiments.

This thesis summarizes my PhD work, but it is also written with future students in mind, who want to continue my work on the hydrodynamic model as their Master's or PhD projects. I have made an effort to include the ideas, methods, and numerical tests,

that were not described in detail in the published papers. The style is linear and essential, in order to provide a clear message to the readers. I hope that both this thesis and the numerical codes available online are able to provide enough information to understand my work and perhaps to follow my footsteps.

The thesis also summarizes the results of my PhD work reported in the publications [32, 47, 48, 51], included in the Appendices A, B, C, D.

Chapter 2 reports a complete derivation of the hydrodynamic equations. Some parts can be found in ordinary textbooks, whereas other parts are new equations emphasizing the real-space formulations appropriate for non-translationally invariant systems. It could provide a starting point for new research directions, especially on the nonlinear hydrodynamic model and electron tunneling.

Chapter 3 contains a description of the formulas and equations that were used in the 2D scattering code for the scattering of light by dimers. The results of the simulations are also discussed. I sometimes refer to the papers in the appendix for further information. I also present a full discussion on the numerical convergence, that is not reported in the paper.

Chapter 4 presents an application of the hydrodynamic model to a practical problem: field enhancement limitations in Surface-Enhanced Raman Spectroscopy (SERS). I shortly describe the concept of SERS for people who are not familiar with it, and then I show the results of my numerical studies.

Chapter 5 deals with the description of the formulas and equations used for the implementation of the hydrodynamic model for waveguiding problems. Also in this case, the discussion of the numerical testing is included.

Finally, Chapter 6 offers the conclusions, a comparison to other approaches, and an outlook on further developments.

2

Hydrodynamic model: an introduction

In this chapter we will introduce the general derivation of the hydrodynamic model starting from the formulation of the classical Hamiltonian of an electron gas interacting with an electromagnetic wave. In the first part we will introduce the fundamentals of the hydrodynamic model. In the second part we will discuss appropriate boundary conditions for the hydrodynamic equation, according to the considerations we made in Paper A (p. 73).

2.1 Bloch's Hydrodynamic model

The hydrodynamic model describes the collective motion of an electron gas in terms of the deviation from the equilibrium density $n_0(\mathbf{r})$ assuming that all the relevant physical quantities can be expressed in terms of the electron density $n(\mathbf{r})$ [27,53]. The basic assumption of this theory is that the ground state of the gas can be described with the Thomas-Fermi theory, and it is characterized by a ground state density $n_0(\mathbf{r})$, and the corresponding one-electron potential $V_0(\mathbf{r})$. The system is characterized by the following quantities: the density $n(\mathbf{r})$, the kinetic pressure in the electron gas $P = P[n(\mathbf{r})]$, and the hydrodynamic velocity $\mathbf{v}(\mathbf{r}, t)$.

The single electron classical Hamiltonian function is given by [54]:

$$H = \frac{3}{5}\frac{\hbar^2}{2m}(3\pi^2)^{2/3}n^{2/3}(\mathbf{r}, t) + \frac{1}{2m}(\mathbf{p} - e\mathbf{A})^2 + e\phi(\mathbf{r}, t),$$

where the vector $\mathbf{p} = m\mathbf{v} + e\mathbf{A}$ is the canonical momentum of an electron in an electromagnetic field. The first term represents the internal kinetic energy of an electron in a Fermi gas, while both the second and the third term represent the Hamiltonian of an electron in the electromagnetic field associated with the scalar potential $\phi(\mathbf{r}, t)$, and the vector potential $\mathbf{A}(\mathbf{r}, t)$. These potentials are generated by the fluctuations of the electron gas, and they can be written as:

$$\phi(\mathbf{r}, t) = \frac{1}{4\pi\varepsilon_0} \int \frac{\rho(\mathbf{r}', t_{\mathrm{r}})}{|\mathbf{r} - \mathbf{r}'|} \, d\mathbf{r}',$$

and

$$\mathbf{A}(\mathbf{r}, t) = \frac{\mu_0}{4\pi} \int \frac{\mathbf{J}(\mathbf{r}', t_{\mathrm{r}})}{|\mathbf{r} - \mathbf{r}'|} \, d\mathbf{r}',$$

where t_{r} is the retarded time $t_{\mathrm{r}} = t - \frac{|\mathbf{r}-\mathbf{r}'|}{c}$, $\rho = en$ is the charge density, and $\mathbf{J} = en\mathbf{v}$ is the current density vector. The electromagnetic field can be calculated by means of the relations $\mathbf{E} = -\nabla\phi - \frac{\partial\mathbf{A}}{\partial t}$, and $\mathbf{B} = \nabla \times \mathbf{A}$.

The internal kinetic energy term can be expressed in terms of the kinetic pressure $P = P[n(\mathbf{r})]$, by using the well-known relation between the kinetic energy per particle and the kinetic pressure in a Fermi gas $P[n(\mathbf{r})] = \frac{2}{5}\frac{\hbar^2}{2m}(3\pi^2)^{2/3}n^{5/3}(\mathbf{r}, t)$.

The canonical coordinates q_i are represented by the Cartesian coordinates $x_i = (x_1, x_2, x_3)$, and their conjugate canonical momenta are given by $p_i = mv_i + eA_i$. In order to study the dynamics of the electron gas, we need to obtain the equation of motion of the electron gas. This follows from the Hamilton equation, that reads:

$$\dot{p}_i = -\frac{\partial H}{\partial x_i}.$$

This equation can be worked out by means of the *Einstein notation*, and we obtain:

$$\dot{p}_i = ev_j\frac{\partial A_j}{\partial x_i} - \frac{2}{5}\frac{\hbar^2}{2m}(3\pi^2)^{2/3}\frac{1}{n^{1/3}}\frac{\partial n(\mathbf{r}, t)}{\partial x_i} - e\frac{\partial\phi(\mathbf{r}, t)}{\partial x_i}. \qquad (2.1.1)$$

Moreover, $\dot{p}_i$ is defined as:

$$\dot{p}_i = m\ddot{x}_i + e\dot{A}_i = m\ddot{x}_i + e\left(\frac{\partial A_i}{\partial t} + v_j\frac{\partial A_i}{\partial x_j}\right). \qquad (2.1.2)$$

If we adopt the Eulerian specification of the flow field, so that velocity of the fluid $\mathbf{v}$ is a function of space $\mathbf{r}$ and time t, then the acceleration term in equation (2.1.2) can be rewritten in this way:

$$\dot{p}_i = m\ddot{x}_i + e\dot{A}_i = m\left(\frac{\partial v_i}{\partial t} + v_j\frac{\partial v_i}{\partial x_j}\right) + e\left(\frac{\partial A_i}{\partial t} + v_j\frac{\partial A_i}{\partial x_j}\right). \quad (2.1.3)$$

If we substitute (2.1.3) into (2.1.1), we get to:

$$m\left(\frac{\partial v_i}{\partial t} + v_j\frac{\partial v_i}{\partial x_j}\right) = -\frac{2}{5}\frac{\hbar^2}{2m}(3\pi^2)^{2/3}\frac{1}{n^{1/3}}\frac{\partial n(\mathbf{r},t)}{\partial x_i} +$$

$$- e\left(\frac{\partial \phi(\mathbf{r},t)}{\partial x_i} + \frac{\partial A_i}{\partial t}\right) + e\left(v_j\frac{\partial A_j}{\partial x_i} - v_j\frac{\partial A_i}{\partial x_j}\right).$$

$$(2.1.4)$$

The term $\left(v_j\frac{\partial A_j}{\partial x_i} - v_j\frac{\partial A_i}{\partial x_j}\right)$ can be written by means of the *Levi-Civita* symbol ϵ_{ijk}, and we obtain:

$$v_j\frac{\partial A_j}{\partial x_i} - v_j\frac{\partial A_i}{\partial x_j} = v_j[\delta_{il}\delta_{jm} - \delta_{im}\delta_{jl}]\frac{\partial A_m}{\partial x_l} = \epsilon_{ijk}v_j\epsilon_{klm}\frac{\partial A_m}{\partial x_l},$$

where we used the *contracted epsilon* identity:

$$\epsilon_{ijk}\epsilon_{klm} = \delta_{il}\delta_{jm} - \delta_{im}\delta_{jl}.$$

At this point we can recognize that:

$$B_k = \epsilon_{klm}\frac{\partial A_m}{\partial x_l},$$

so we can rewrite equation (2.1.4) as:

$$m\left(\frac{\partial v_i}{\partial t} + v_j\frac{\partial v_i}{\partial x_j}\right) = -\frac{2}{5}\frac{\hbar^2}{2m}(3\pi^2)^{2/3}\frac{1}{n^{1/3}}\frac{\partial n(\mathbf{r},t)}{\partial x_i} + e\left(E_i + \epsilon_{ijk}v_j B_k\right),$$

$$(2.1.5)$$

that contains the *Lorentz force* term $e\left(E_i + \epsilon_{ijk}v_j B_k\right)$.

The equation (2.1.5) is the well-known *Euler equation*, where the pressure term is given by the pressure in a Fermi gas, and the force term is due to the electromagnetic field force. The electron density $n(\mathbf{r},t)$ must satisfy the continuity relationship, that in the Einstein notation reads:

$$\frac{\partial n}{\partial t} + \frac{\partial}{\partial x_j}[n(\mathbf{r},t)v_j] = 0. \quad (2.1.6)$$

2.1.1   Linearized hydrodynamic model

The Euler equation and the continuity equations are are nonlinear, but they can be linearized in the case of small-amplitude motion as follows [54]:

$$n(\mathbf{r}, t) = n_0(\mathbf{r}) + n_1(\mathbf{r}, t)$$
$$E_i(\mathbf{r}, t) = E_{1i}(\mathbf{r}, t)$$
$$B_i(\mathbf{r}, t) = B_{1i}(\mathbf{r}, t)$$
$$v_i(\mathbf{r}, t) = v_{1i}(\mathbf{r}, t),$$

$$(2.1.7)$$

where $n_0(\mathbf{r})$ is the electron density at rest, and the zero-order terms are $E_{oi}(\mathbf{r})$, $B_{0i}(\mathbf{r})$, $v_{0i}(\mathbf{r})$ vanish. We can now substitute the terms of equation (2.1.7) into the equation (2.1.5), and consider only the terms of order zero and order one. For the sake of clarity, we now analyze each term of equation (2.1.5). The term on the left hand side becomes:

$$m\left(\frac{\partial v_i}{\partial t} + v_j \frac{\partial v_i}{\partial x_j}\right) = m\left(\frac{\partial v_{1i}}{\partial t} + v_{1j}\frac{\partial v_{1j}}{\partial x_j} + O(v_{2i})\right) = m\frac{\partial v_{1i}}{\partial t} + O(v_{2i}).$$

In order to analyze the first term on the right hand side of equation (2.1.5), we point out the Taylor expansion around the point $x = 0$ of the function $f(x) = 1/(\tau + x)^{1/3}$:

$$f(x) = \frac{1}{(\tau + x)^{1/3}} = \frac{1}{\tau^{1/3}}\left(1 - \frac{1}{3}\frac{1}{\tau}x\right) + O(x^2).$$

We can now proceed, and obtain:

$$\frac{1}{n^{1/3}}\frac{\partial n(\mathbf{r}, t)}{\partial x_i} = \frac{1}{n_0^{1/3}}\left(1 - \frac{1}{3}\frac{1}{n_0}n_1\right)\left(\frac{\partial n_0}{\partial x_i} + \frac{\partial n_1}{\partial x_i}\right) + O(n_2) =$$

$$\frac{1}{n_0^{1/3}}\left(\frac{\partial n_0}{\partial x_i} + \frac{\partial n_1}{\partial x_i} - \frac{1}{3}\frac{1}{n_0}n_1\frac{\partial n_0}{\partial x_i}\right) + O(n_2).$$

The Lorentz force term reads:

$$E_i + \epsilon_{ijk}v_j B_k = E_{1i} + \epsilon_{ijk}v_{1j}B_{1k} = E_{1i} + O(E_{2i}),$$

and we can notice that the magnetic force does not give any contribution to the first order approximation. We can now finally write the linearized hydrodynamic equation:

$$
m\frac{\partial v_i}{\partial t} = -\frac{2}{5}\frac{\hbar^2}{2m}(3\pi^2)^{2/3}\frac{1}{n_0^{1/3}}\left(\frac{\partial n_0}{\partial x_i} + \frac{\partial n}{\partial x_i} - \frac{1}{3}\frac{1}{n_0}n\frac{\partial n_0}{\partial x_i}\right) + eE_i,
$$

$$(2.1.8)$$

where we dropped the notation n_1 and E_{1i} in order to improve the readibility.

A similar procedure can be followed for the continuity equation, that to first order reads:

$$
\frac{\partial n}{\partial t} + \frac{\partial}{\partial x_j}(n_0(\mathbf{r},t)v_j) = 0. \tag{2.1.9}
$$

These equations form the basis of the calculation of the linear response to an external field in the hydrodynamic model. Most of the applications of the hydrodynamic theory are based on a simplified version of the linearized equations, where the medium is assumed to behave locally as a uniform electron gas. This allows us to neglect the terms explicitly containing the derivatives of n_0 in both the equations (2.1.8) and (2.1.9), that become

$$
m\frac{\partial v_i}{\partial t} = -\frac{2}{5}\frac{\hbar^2}{2m}(3\pi^2)^{2/3}\frac{1}{n_0^{1/3}}\frac{\partial n}{\partial x_i} + eE_i, \tag{2.1.10}
$$

and

$$
\frac{\partial n}{\partial t} + n_0\frac{\partial}{\partial x_j}v_j = 0. \tag{2.1.11}
$$

If we introduce the Fermi velocity v_F, defined as:

$$
v_\mathrm{F} = \frac{\hbar}{m}(3n_0\pi^2)^{1/3},
$$

then we can write the equation of motion (2.1.10) as:

$$
m\frac{\partial v_i}{\partial t} = -\beta^2\frac{m}{n_0}\frac{\partial n}{\partial x_i} + eE_i, \tag{2.1.12}
$$

where $\beta^2 = \frac{2}{5}v_F^2$. The equation (2.1.12) states that the force that acts on the electron is given by the sum of the force exerted by the electric field and the pressure force given by the gradient of the electron density.

It is useful for the next considerations to write both eq. (2.1.11) and eq. (2.1.12) in vectorial notation. In this case, the continuity equation looks like:

$$\frac{\partial n}{\partial t} + n_0 \nabla \cdot \mathbf{v}(\mathbf{r}, t) = 0, \tag{2.1.13}$$

and the equation of motion reads:

$$m\frac{\partial \mathbf{v}}{\partial t} = -\beta^2 \frac{m}{n_0}\nabla n(\mathbf{r}, t) + e\mathbf{E}(\mathbf{r}, t). \tag{2.1.14}$$

2.2   Hydrodynamic Drude model

A classical model that describes the electron motion in a metal is the Drude model, that was proposed by P. Drude in 1900 [55, 56]. In this model the electrons in a metal are assumed to move freely through space, apart from collisions, not with each other, but rather with the much larger atomic cores. The Drude equation of motion for the free electron can be written as [13]:

$$m\frac{\partial \mathbf{v}}{\partial t} = e\mathbf{E}(\mathbf{r}, t) - \gamma\mathbf{v}, \tag{2.2.1}$$

where $\gamma = 1/\tau$, and τ is the *relaxation time*, that is the average time between collisions of the electron with the nuclei. Thus, the electrons are subject to both the electromagnetic field force and to the *drag force* exerted by the nuclei.

When we derived the hydrodynamic equation of motion (2.1.14), we did not take into account for the interaction of the electrons with the atomic cores. We can include this effect by means of the drag term $-\gamma\mathbf{v}$, as in eq. (2.2.1), and we obtain:

$$m\frac{\partial \mathbf{v}}{\partial t} = -\beta^2 \frac{m}{n_0}\nabla n(\mathbf{r}, t) - \gamma\mathbf{v} + e\mathbf{E}(\mathbf{r}, t). \tag{2.2.2}$$

This is the *hydrodynamic Drude equation*, and it differs from eq. (2.2.1) for the presence of the pressure term $-\beta^2 \frac{m}{n_0}\nabla n(\mathbf{r}, t)$.

We can now look at the hydrodynamic model from the electro-magnetic point of view by means of the current density vector $\mathbf{J}$, that to the first-order approximation is defined as $\mathbf{J} = -en_0\mathbf{v}$, and the charge density $\rho = -en$. If we multiply both sides of eq. (2.2.2) by $-en_0$, we can rewrite it as:

$$\frac{\partial \mathbf{J}}{\partial t} = -\beta^2 \nabla \rho - \gamma \mathbf{J} + \varepsilon_0 \omega_p^2 \mathbf{E}, \qquad (2.2.3)$$

where ω_p is called *plasma frequency* of the electron gas, and is given by $\omega_p = \sqrt{\frac{n_0 e^2}{m \epsilon_0}}$, and ϵ_0 is the electric permittivity of vacuum.

In the same way, the continuity equation (2.1.13) becomes:

$$\nabla \cdot \mathbf{J} = -\frac{\partial \rho}{\partial t}. \qquad (2.2.4)$$

These two equations can be merged by deriving eq (2.2.3) respect to time, and using eq. (2.2.4) into it. We obtain the following equation:

$$\beta^2 \nabla \nabla \cdot \mathbf{J} - \frac{\partial^2 \mathbf{J}}{\partial t^2} + \gamma \frac{\partial \mathbf{J}}{\partial t} = -\epsilon_0 \omega_p^2 \frac{\partial \mathbf{E}}{\partial t}, \qquad (2.2.5)$$

that links the electric field $\mathbf{E}$ to the polarization current $\mathbf{J}$. The two fields are also linked by means of Maxwell's equations, and the polarization of the electron gas is fully described by the closed equation system:

$$\nabla \times \mathbf{E} = -\mu_0 \frac{\partial \mathbf{H}}{\partial t}$$
$$\nabla \times \mathbf{H} = \epsilon_0 \frac{\partial \mathbf{E}}{\partial t} + \mathbf{J}$$
$$\beta^2 \nabla \nabla \cdot \mathbf{J} - \frac{\partial^2 \mathbf{J}}{\partial t^2} + \gamma \frac{\partial \mathbf{J}}{\partial t} = -\epsilon_0 \omega_p^2 \frac{\partial \mathbf{E}}{\partial t}$$

$$(2.2.6)$$

where $\mathbf{H}$ is the magnetic field. In the next chapters, we will always work with time harmonic field, so it is useful to transform the previous system in the frequency domain. The equation (2.2.5) becomes:

$$\beta^2 \nabla \nabla \cdot \mathbf{J} + \omega(\omega + i\gamma)\mathbf{J} = i\omega \epsilon_0 \omega_p^2 \mathbf{E}, \qquad (2.2.7)$$

then the equation system (2.2.6) reads:

$$\nabla \times \mathbf{E} = i\omega\mu_0\mathbf{H}$$
$$\nabla \times \mathbf{H} = -i\omega\epsilon_0\mathbf{E} + \mathbf{J}$$
$$\beta^2\nabla\nabla \cdot \mathbf{J} + \omega(\omega + i\gamma)\mathbf{J} = i\omega\epsilon_0\omega_p^2\mathbf{E}.$$

$$(2.2.8)$$

This is the equation system that we used in our work. It is important to mention that the value of $\beta^2 = \frac{2}{5}v_{\mathrm{F}}^2$ we introduced at par. (2.1.1) is valid at low frequencies, and it must be corrected in the visible frequency range. The corrected value is $\beta = \sqrt{3/(D+2)}v_{\mathrm{F}}$, where D is the number of spatial dimensions that are not quantum confined [57]. In the next chapters, we will assume $D = 3$.

We can follow the same procedure and derive the expression of the polarization current density in the Drude model, that turns out to be proportional to the electric field [58]:

$$\mathbf{J} = i\omega\epsilon_0\frac{\omega_p^2}{\omega(\omega + i\gamma)}\mathbf{E} = \sigma_{\mathrm{Drude}}\mathbf{E}, \qquad (2.2.9)$$

where σ_{Drude} is the AC Drude conductivity of the electron gas, that can be written as:

$$\sigma_{\mathrm{Drude}} = \frac{\sigma_0}{(1 - i\omega\tau)}, \qquad (2.2.10)$$

with $\sigma_0 = \frac{n_o e^2\tau}{m}$ is the DC Drude conductivity. Equation (2.2.9) is the well-known Ohm's law, and it could also be obtained from eq. (2.2.7) for $\beta = 0$.

2.2.1 Spatial nonlocality

The pressure term in the hydrodynamic equation of motion (2.2.3) indicates that the compression or expansion of the electron gas in a point propagates to the other points in the gas, by means of a pressure wave, analogous to a sound wave [28]. This pressure wave affects the polarization of the electron gas in a given point. From the electromagnetic point of view, this is equivalent to say that the electron gas described by the hydrodynamic model is a *nonlocal medium*. To show this, we rewrite eq. (2.2.7) as:

$$\frac{\beta^2}{i\omega\epsilon_0\omega_p^2}\nabla\nabla \cdot \mathbf{J} + \frac{(\omega + i\gamma)}{i\epsilon_0\omega_p^2}\mathbf{J} = \mathbf{E},$$

that we can reformulate by introducing the linear operator

$$L = \frac{\beta^2}{i\omega\epsilon_0\omega_p^2}\nabla\nabla\cdot + \frac{(\omega + i\gamma)}{i\epsilon_0\omega_p^2},$$

as:

$$L[\mathbf{J}] = \mathbf{E}.$$

If we introduce the dyadic Green function $\boldsymbol{\sigma}(\mathbf{r}, \mathbf{r}', \omega)$ associated to the operator L, that solves

$$L[\sigma(\mathbf{r}, \mathbf{r}', \omega)] = \boldsymbol{\delta}(\mathbf{r}, \mathbf{r}', \omega), \qquad (2.2.11)$$

then equation (2.2.7) can be written in integral form as:

$$\mathbf{J}(\mathbf{r}, \omega) = \int_\Omega \boldsymbol{\sigma}(\mathbf{r}, \mathbf{r}', \omega) \cdot \mathbf{E}(\mathbf{r}', \omega)\, d^3 r',$$

where Ω is the volume of the electron gas. This equation shows that the polarization current density in a point $\mathbf{r}$ is affected by the application of the electric field in all the points of the gas volume. This is the definition of *spatial dispersion* [59], and the metal is a nonlocal medium.

If we put $\beta = 0$ in eq. (2.2.11), we get the conductivity for the Drude model:

$$\boldsymbol{\sigma}(\mathbf{r}, \mathbf{r}', \omega) = \sigma_{\text{Drude}}\boldsymbol{\delta}(\mathbf{r}, \mathbf{r}', \omega),$$

that actually shows that the polarization current density in a point $\mathbf{r}$ is affected by the application of the electric field in the same point (see fig. 2.1). The electron gas in the Drude model is a local medium.

In the next sections and chapters, we will use the term local model to indicate the Drude model, and nonlocal model to refer to the hydrodynamic Drude model.

2.2.2 Boundary Conditions

The system of equations (2.2.8) must be equipped with an appropriate set of boundary conditions (see Paper A, p. 73). The usual Maxwell's boundary conditions are no longer sufficient, because the polarization current is no longer given in terms of the Ohm's law, but as a solution of a differential equation. Thus, something must be stated about the behavior of this quantity on the boundary. We
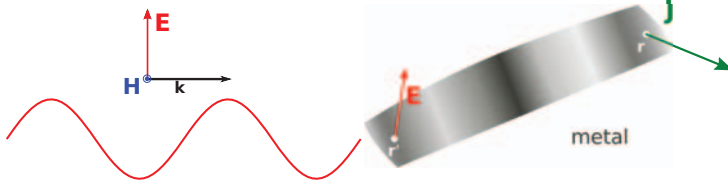
Figure 2.1 Spatial dispersion. The polarization current density in a point $\mathbf{r}$ is affected by the field in a point $\mathbf{r}'$.

can start by recalling Maxwell's boundary conditions, that state the continuity of the tangential components of both the magnetic and electric field:

$$\mathbf{n} \times [\mathbf{E}_1 - \mathbf{E}_2] = 0,$$
$$\mathbf{n} \times [\mathbf{H}_1 - \mathbf{H}_2] = 0,$$

where 1 and 2 refer to the inner volume and the external one respectively. The polarization current has a tangential component and a normal component on the surface boundary. The tangential components $\mathbf{n} \times \mathbf{J}$ are in general non-zero because the electron plasma is described as a fluid that is free to move around the boundaries. More specifically, there is no viscous term into the Euler equation (2.1.5). Something different happens for the normal component $\mathbf{n} \cdot \mathbf{J}$, that is related to the electron spill-out. The phenomenon of electron spill-out can be important in case of electron transport among nanostructures [26], but this is not treated in this thesis. The structure that we study are always considered as "isolated", so to avoid all the complications due to the treatment of the electron transport. Thus we can state the boundary conditions that suit this physical reasoning are [32]:

$$\mathbf{n} \cdot \mathbf{J} = 0. \tag{2.2.12}$$

There is an important consequence of this boundary condition and it is related to the surface charges. In the local mode, the charges are distributed on the surface as "impulsive" charges. We know that in the absence of free charges, the divergence of the displacement vector $\mathbf{D}$ is zero:

$$\nabla \cdot \mathbf{D} = 0, \tag{2.2.13}$$

and this implies that the normal component of the $\mathbf{D}$ field is continuous across the boundary:

$$\mathbf{n} \cdot [\mathbf{D}_1 - \mathbf{D}_2] = 0. \qquad (2.2.14)$$

In a local medium, the $\mathbf{D}$ vector can be expressed as:

$$\mathbf{D} = \epsilon_0 \epsilon_r \mathbf{E},$$

so the condition (2.2.14) implies that:

$$\mathbf{n} \cdot \epsilon_0 [\epsilon_1 \mathbf{E}_1 - \epsilon_2 \mathbf{E}_2] = 0.$$

This means that there is a jump in the normal component of the electric field due to impulsive polarization surface charges:

$$\mathbf{n} \cdot [\mathbf{E}_1 - \mathbf{E}_2] = \frac{\sigma}{\epsilon_0}.$$

This is the case of the local Drude model, where $\epsilon_1 = \epsilon_{\text{Drude}}$, and $\epsilon_2 = \epsilon_{\text{diel}}$, the permittivity of the surrounding dielectric. This is not the case of the nonlocal HD model. In order to show this, we can start from the general formulation of the $\mathbf{D}$ field:

$$\mathbf{D} = \epsilon_0 \mathbf{E} + \mathbf{P},$$

where $\mathbf{P}$ is the polarization vector, that is linked to the polarization current by:

$$\mathbf{J} = -i\omega \mathbf{P}, \qquad (2.2.15)$$

so we can write:

$$\mathbf{D} = \epsilon_0 \mathbf{E} + \frac{\mathbf{J}}{i\omega}. \qquad (2.2.16)$$

If we impose the condition (2.2.14), we get:

$$\mathbf{n} \cdot [\epsilon_0 \mathbf{E}_1 + \frac{\mathbf{J}}{i\omega} - \epsilon_0 \mathbf{E}_2] = 0.$$

We can apply the condition (2.2.12), then we get:

$$\mathbf{n} \cdot [\mathbf{E}_1 - \mathbf{E}_2] = 0. \qquad (2.2.17)$$

This means that there is no impulsive charge density in the hydrodynamic model for the pure electron plasma. In this case, indeed, there is only volume charge density. However, for metals that, beside the pure plasma response, also have interband absorption, eq. (2.2.17) does not hold and a jump in the normal component of the $\mathbf{E}$ field does occur.

2.2.3 Charge distribution

The volumetric charge distribution in the hydrodynamic model satisfies the homogeneous Helmoltz equation. In order to show this, we can apply the divergence operator to eq. (2.2.16), and obtain

$$\nabla \cdot \mathbf{E} = \frac{\rho}{\epsilon_0}, \tag{2.2.18}$$

where we used the continuity equation (2.2.13), and (2.2.4) in the frequency domain.

If we apply the divergence operator $\nabla\cdot$ to both sides of eq. (2.2.7), and we use the continuity equations $\nabla \cdot \mathbf{J} = i\omega\rho$ and $\nabla \cdot \mathbf{E} = \rho/\epsilon_0$, we obtain:

$$\nabla^2 \rho + \frac{\omega(\omega + i\gamma) - \omega_p^2}{\beta^2}\rho = 0. \tag{2.2.19}$$

The Helmholtz equation (2.2.19) describes the plasma oscillations in the electron gas. If we put $\gamma = 0$, it can be easily seen that the oscillations are damped for $\omega < \omega_p$. This corresponds to the case of *surface plasmons*, that are localized around the surface of the metal and they fade into the bulk. *Bulk plasmons* are excited instead for $\omega \geq \omega_p$ [54]. We will observe these behaviors in the next chapters.

In the previous paragraph we analyzed the effect of the finite charge distribution on the boundary conditions for the electric field. However, the presence of volumetric charges also affects the propagation properties of the electric field.

We know that the electric field can be decomposed in a transversal (divergence-free) and longitudinal (curl-free) component, by using the Helmholtz decomposition:

$$\mathbf{E} = \mathbf{E}^T + \mathbf{E}^L.$$

It is then evident that if $\nabla \cdot \mathbf{E} \neq 0$, then a longitudinal wave propagates in the electron gas.

For the sake of simplicity, we can choose $\gamma = 0$. We consider the Ampère-Maxwell equation in the local case, that reads

$$\nabla \times \mathbf{H} = -i\omega\epsilon_0 \left(1 + i\frac{\sigma_{\text{Drude}}}{\epsilon_0\omega}\right)\mathbf{E}.$$

If we apply the divergence operator $\nabla\cdot$ to both sides, and we use the definition of σ_{Drude} in eq. (2.2.10), we get:

$$\left(1 - \frac{\omega_p^2}{\omega^2}\right)\nabla \cdot \mathbf{E} = 0.$$

This expression implies that $\nabla \cdot \mathbf{E} = 0$, unless $\omega = \omega_p$. This means that the electric field in the local case is *transversal* for $\omega \neq \omega_p$. A longitudinal wave can arise only at $\omega = \omega_p$, and it is associated with a bulk plasmon [13].

This is not the case anymore in the hydrodynamic model. In fact, we can see from eq. (2.2.18) that $\nabla \cdot \mathbf{E} \neq 0$, and this means that there is always a longitudinal wave propagating in the gas. These waves are called *plasma waves*, and are well known in plasma physics [60]. Thus, in the hydrodynamic model both transversal and longitudinal waves are allowed to propagate in the gas at any frequency.

2.3   Electromagnetic Energy stored in the free-electron gas

The EM energy density stored in the free-electron gas plays an important role in the study of the mode confinement in plasmonic nanostructures (see chapter 5). We derive here a generalized expression for the electromagnetic energy density, that includes the contributions stored in the hydrodynamics of the free-electron gas. We start from the Poynting theorem in time: domain [61]

$$\int_{\partial\Omega} \mathbf{E} \times \mathbf{H} \cdot \hat{\mathbf{n}}\, d\mathbf{S} = -\int_{\Omega} \left[\varepsilon_0 \mathbf{E} \cdot \dot{\mathbf{E}} + \mathbf{E} \cdot \dot{\mathbf{P}} + \mu_0 \mathbf{H} \cdot \dot{\mathbf{H}}\right] dV, \quad (2.3.1)$$

where $\mathbf{P}$ is the polarization vector, V is the volume of the electron gas, and ∂V is its boundary. The polarization current $\mathbf{J}$ is linked to $\mathbf{P}$ by:

$$\mathbf{J} = \frac{\partial \mathbf{P}}{\partial t} = \dot{\mathbf{P}}. \qquad (2.3.2)$$

At the same time, the polarization current is related to the electric field by means of the hydrodynamic equation. In time domain, the linearized hydrodynamic Euler equation for the electron dynamics is given by eq. (2.2.2), that we recall here:

$$m\frac{\partial \mathbf{v}}{\partial t} = -\beta^2 \frac{m}{n_o}\nabla n - m\gamma\mathbf{v} - e\mathbf{E}, \qquad (2.3.3)$$

where $\mathbf{v}$ is the electron velocity, n is the electron density, n_0 is the electron density at rest, and m the electron mass. If we introduce the polarization current $\mathbf{J} = -en_0\mathbf{v}$ and the charge density $\rho = -en$, the Eq. (2.3.3) becomes:

$$\frac{\partial \mathbf{J}}{\partial t} = -\beta^2 \nabla \rho - \gamma \mathbf{J} + \varepsilon_0 \omega_p^2 \mathbf{E}.$$

Next, if we use the definition (2.3.2), and the continuity equation $\rho = -\nabla \cdot \mathbf{P}$, we get:

$$\beta^2 \nabla \nabla \cdot \mathbf{P} - \frac{\partial^2 \mathbf{P}}{\partial t^2} - \gamma \frac{\partial \mathbf{P}}{\partial t} + \varepsilon_0 \omega_p^2 \mathbf{E} = 0.$$

We can now isolate $\mathbf{E}$ in this expression,

$$\mathbf{E} = -\frac{1}{\varepsilon_0 \omega_p^2} \left[\beta^2 \nabla \nabla \cdot \mathbf{P} - \frac{\partial^2 \mathbf{P}}{\partial t^2} - \gamma \frac{\partial \mathbf{P}}{\partial t} \right],$$

and by taking the inner product with $\dot{\mathbf{P}}$, we obtain:

$$\mathbf{E} \cdot \dot{\mathbf{P}} = -\frac{1}{\varepsilon_0 \omega_p^2} \left[\beta^2 \nabla \nabla \cdot \mathbf{P} \cdot \dot{\mathbf{P}} - \frac{1}{2} \frac{d \dot{\mathbf{P}}^2}{dt} - \gamma \dot{\mathbf{P}}^2 \right]. \qquad (2.3.4)$$

In the spirit of Eq. (2.3.1), we now integrate Eq. (2.3.4) over the metallic volume,

$$\int_\Omega \mathbf{E} \cdot \dot{\mathbf{P}} \, dV = -\frac{1}{\varepsilon_0 \omega_p^2} \int_\Omega \left[\beta^2 \nabla \nabla \cdot \mathbf{P} \cdot \dot{\mathbf{P}} - \frac{1}{2} \frac{d \dot{\mathbf{P}}^2}{dt} - \gamma \dot{\mathbf{P}}^2 \right] dV. \quad (2.3.5)$$

Our next step is to integrate by part,

$$\int_\Omega \nabla \nabla \cdot \mathbf{P} \cdot \dot{\mathbf{P}} \, dV = -\int_\Omega \nabla \cdot \mathbf{P} \nabla \cdot \dot{\mathbf{P}} \, dV + \int_{\partial \Omega} \nabla \cdot \mathbf{P} \dot{\mathbf{P}} \cdot \hat{\mathbf{n}} \, dS.$$

To further proceed, we now apply the physical boundary condition $\mathbf{J} \cdot \hat{\mathbf{n}} = 0$. This gives:

$$\int_\Omega \nabla \nabla \cdot \mathbf{P} \cdot \dot{\mathbf{P}} \, dV = -\int_\Omega \frac{1}{2} \frac{d(\nabla \cdot \mathbf{P})^2}{dt} \, dV.$$

In this way Eq. (2.3.5) now reads

$$\int_\Omega \mathbf{E} \cdot \dot{\mathbf{P}} \, dV = \frac{1}{\varepsilon_0 \omega_p^2} \int_\Omega \left[\frac{\beta^2}{2} \frac{d(\nabla \cdot \mathbf{P})^2}{dt} + \frac{1}{2} \frac{d \dot{\mathbf{P}}^2}{dt} + \gamma \dot{\mathbf{P}}^2 \right] dV,$$

and substituting into the Poynting theorem, Eq. (2.3.1), we get

$$\int_{\partial\Omega} \mathbf{E} \times \mathbf{H} \cdot \hat{\mathbf{n}}\, d\mathbf{S} + \int_{\Omega} \frac{\gamma}{\varepsilon_0 \omega_p^2} \dot{\mathbf{P}}^2\, dV = -\int_{\Omega} \dot{u}\, dV.$$

Here, u is the electromagnetic energy density defined as

$$u = \frac{1}{2}\varepsilon_0 \mathbf{E}^2 + \frac{\beta^2}{2\varepsilon_0 \omega_p^2}\left(\nabla \cdot \mathbf{P}\right)^2 + \frac{1}{2\varepsilon_0 \omega_p^2}\dot{\mathbf{P}}^2 + \frac{1}{2}\mu_0 \mathbf{H}^2.$$

Finally, if we recall the continuity equation for the polarization charge density, given by $\rho = -\nabla \cdot \mathbf{P}$, and we use Eq. (2.3.2), then

$$u = \frac{1}{2}\varepsilon_0 \mathbf{E}^2 + \frac{\beta^2}{2\varepsilon_0 \omega_p^2}\rho^2 + \frac{1}{2\varepsilon_0 \omega_p^2}\mathbf{J}^2 + \frac{1}{2}\mu_0 \mathbf{H}^2. \qquad (2.3.6)$$

This is our generalization of the common energy-density to account for the energy stored in the additional degrees of freedom associated with the nonlocal hydrodynamics of the electron gas. For time-harmonic fields, this expression can easily be time-averaged.

3

Scattering of light from metallic nanowires in the hydrodynamic model

In this chapter we will discuss the application of the hydrodynamic equation that we derived in the previous chapter to the study of some important 2D structures: the cylindrical nanowire, the dimer of cylindrical nanowires and the bow-tie dimer. The discussion will follow the material described in Paper B (p. 79), but more details will be given about the used formulas, the implementation of the algorithm in COMSOL, and the computational validation/benchmarking.

3.1   Numerical implementation

The system of equations (2.2.8) was solved numerically by means of COMSOL Multiphysics 4.1. This is a commercial software for solving partial differential equations based on the Finite Element Method (FEM). COMSOL has built-in routines for treating specific physical models, such as fluid flow, acoustics, and heat transfer. The routine that was used extensively in our case is the *Electromagnetic Waves* (EM) module, that includes methods for solving electromagnetic problems like scattering and waveguiding. These routines can be coupled in order to treat multiple or simultaneous physical phenomena. COMSOL also has a general routine for solving mathematical equations in the general form, called *weak form PDE*, that turns out to be very useful in our case.

The EM module can treat only media that are spatially homogeneous, described by a dielectric function that can be either a scalar or a tensor, in case of an anisotropic medium. Thus, the module does not allow to treat *nonlocal* media, where the relationship between the polarization field and the dielectric field is described by a differential equation. This is actually the case of the HD model, because the polarization of electron gas is a nonlocal phenomenon, as we discussed in Chapter 2. We had to devise a specific approach to overcome this problem in COMSOL. The solution we proposed is the implementation of the HD equation of motion (2.2.7) in the general "weak form PDE" module and to couple it with the "EM module".

COMSOL solves the differential equations by implementing the *Galerkin method* [62], so we need to provide the HD equation of motion (2.2.7) in the weak form. This can be done straightforwardly by applying the standard integration by part procedures. We recall the HD equation of motion here:

$$\beta^2 \nabla \nabla \cdot \mathbf{J} + \omega(\omega + i\gamma)\mathbf{J} = i\omega\epsilon_0\omega_p^2\mathbf{E}$$

this is defined on a domain in space, say Ω, that is in general 3-dimensional. We can multiply both sides of this equation by a test function $\tilde{\mathbf{J}}$ that satisfies the same boundary conditions of $\mathbf{J}$ on $\partial\Omega$, and belongs to the space $C^\infty(\Omega)$. We can integrate both side over the domain Ω, and we obtain:

$$\int_\Omega \left[\beta^2 \nabla \nabla \mathbf{J} \cdot \tilde{\mathbf{J}} + \omega(\omega + i\gamma)\mathbf{J} \cdot \tilde{\mathbf{J}} - i\omega\epsilon_0\omega_p^2\mathbf{E} \cdot \tilde{\mathbf{J}} \right] d\mathbf{r} = 0. \quad (3.1.1)$$

If we integrate by part the $\nabla\nabla\cdot$ operator, we get:

$$\int_\Omega \nabla\nabla \cdot \mathbf{J} \cdot \tilde{\mathbf{J}} \, d\mathbf{r} = -\int_\Omega \nabla \cdot \mathbf{J} \nabla \cdot \tilde{\mathbf{J}} \, d\mathbf{r} + \int_{\partial\Omega} \nabla \cdot \mathbf{J} \tilde{\mathbf{J}} \cdot \hat{n} \, d\sigma,$$

that can be substituted into the equation (3.1.1), and obtaining:

$$\int_\Omega \left[-\beta^2 \nabla \cdot \mathbf{J} \nabla \cdot \tilde{\mathbf{J}} + \omega(\omega + i\gamma)\mathbf{J} \cdot \tilde{\mathbf{J}} - i\omega\epsilon_0\omega_p^2\mathbf{E} \cdot \tilde{\mathbf{J}} \, d\mathbf{r} \right] =$$

$$= \int_{\partial\Omega} \nabla \cdot \mathbf{J} \, \tilde{\mathbf{J}} \cdot \hat{n} \, d\sigma. \quad (3.1.2)$$

The integral at the right-hand side of equation (3.1.2) can be interpreted as a flux of energy through the boundaries of the domain

Ω due to the flow of electric current. We exclude this possibility here, and we apply the boundary conditions (2.2.12). We can finally write down the equation that we implemented in COMSOL:

$$\int_{\Omega} \left[-\beta^2 \nabla \cdot \mathbf{J} \, \nabla \cdot \tilde{\mathbf{J}} + \omega(\omega + i\gamma)\mathbf{J} \cdot \tilde{\mathbf{J}} - i\omega\epsilon_0\omega_p^2 \mathbf{E} \cdot \tilde{\mathbf{J}} \, d\mathbf{r} \right] = 0. \quad (3.1.3)$$

3.2   Scattering from nanowires

The first application that we are going to discuss is the scattering from a gold cylindrical nanowire in vacuum. The free-electron gas parameters for gold are obtained from [63], and we do not consider interband effects here.

The electromagnetic problem can be solved analytically, and it has been treated by Ruppin in the work [64]. The analytical solutions provide an important benchmark for our numerical results, as we discussed in Paper B (p. 79).

As it is shown in Fig 3.1, our system is infinite in one direction, say z, and the incoming electric field $\mathbf{E}_i$ is a TM-polarized plane wave, in order to excite the longitudinal waves associated with the nonlocal effects (see par. 2.2.3). In fact, it can be seen from the motion equation in the system (2.2.8), that if the electric field is polarized along z, the z-component of $\mathbf{J}$ does not show any nonlocal effect because the derivative $\frac{\partial J_z}{\partial z} = 0$. An important parameter that is introduced for studying the scattering by a particle [65], is the *extinction cross-section* σ_{ext}, that is defined by the quantity:

$$\sigma_{\text{ext}}(\omega) = \frac{|P_{\text{ext}}|}{2aI_0},$$

where a is the radius of the wire, I_0 is the power density of the plane wave, $I_0 = |E_0|^2/2\xi_0$, where $\xi_0 = 376.730\,\Omega$ is the impedance of free space. We can look a bit further into the definition of *extinction power*, by introducing the *extinction power density vector* $\mathbf{S}_{\text{ext}}$:

$$\mathbf{S}_{\text{ext}} = \frac{1}{2}\left(\mathbf{E}_i \times \mathbf{H}_{\text{scat}}^*\right) + \frac{1}{2}\left(\mathbf{E}_{\text{scat}} \times \mathbf{H}_i^*\right),$$

that contains the exchange terms between the incoming source field, $\left(\mathbf{E}_i, \mathbf{H}_i\right)$, and the scattered field $\left(\mathbf{E}_{\text{scat}}, \mathbf{H}_{\text{scat}}\right)$. The extinction power can be calculated by integrating the vector $\mathbf{S}_{\text{ext}}$ along
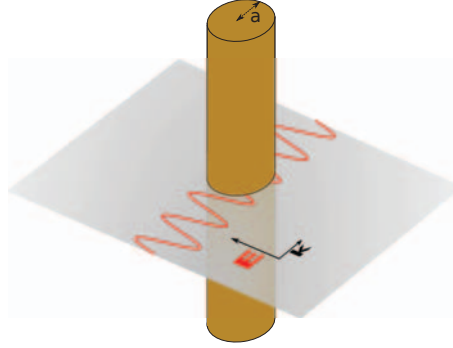
Figure 3.1 Cylindrical nanowire. The incoming field is TM-polarized.

an arbitrary closed path l surrounding the structure:

$$P_{\text{ext}} = \oint_l \mathbf{S}_{\text{ext}} \cdot \mathbf{n} \, dl, \qquad (3.2.1)$$

where $\mathbf{n}$ is the outward normal vector along the path l. It can be easily shown that:

$$P_{\text{ext}} = P_{\text{abs}} - P_{\text{scat}},$$

where P_{abs} is the power dissipated in the metal due to losses (Joule effect), and P_{scat} is the scattered power. It is important to notice that the convention for the verse of $\mathbf{n}$ implies that $P_{\text{abs}} < 0$, and $P_{\text{scat}} > 0$. It is clear that σ_{ext} takes into account both the power that is scattered and the power absorbed by the structure. The frequency spectrum of σ_{ext} gives information about the plasmonic excitations into the metal.

Fig. 3.2 shows the extinction cross section for the case of a nanowire with radius $a = 2\,\text{nm}$ in Panel (a), and a nanowire with radius $a = 25\,\text{nm}$ in Panel (b). The nanowires are made of gold, and the interband effects are not included.

Panel (a) illustrates an important characteristic of the nonlocal hydrodynamic model: the blueshift of surface plasmon resonance. In the local case, the surface plasmon frequency is given by $\omega_{\text{sp}}^{\text{loc}} = \omega_{\text{p}}/\sqrt{2} = 6.231$ eV, and it is independent of the size of the rods, if the quasi-static conditions are fulfilled, as in the case of nanorods with sizes of the order of $10\,\text{nm}$ or below. The blueshift amounts for $\Delta\hbar\omega = 0.19\,\text{eV}$, so $\omega_{\text{sp}}^{\text{nloc}} = 6.421$ eV.

In the Panel (b) the case of $a = 25\,\text{nm}$ is considered, and it is clear that the difference between local and nonlocal case is not as
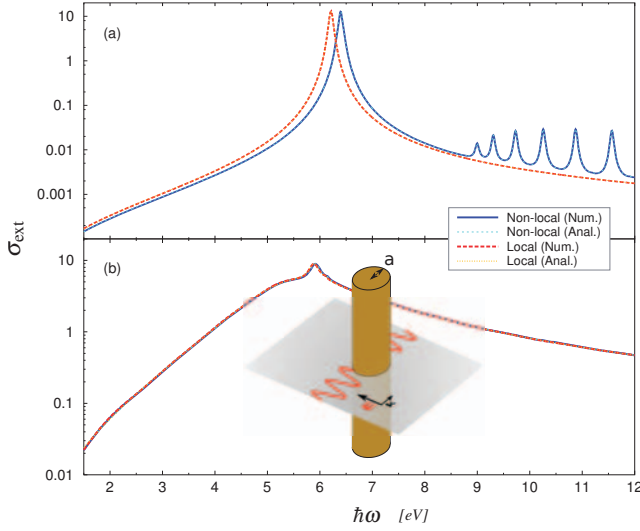
Figure 3.2 Cylindrical nanowires, Extinction Cross Section. Panel (a) Radius $a = 2\,\mathrm{nm}$; The plot shows σ_{ext} for the local case (red-dashed curve) and the nonlocal case (blue curve). The SPP resonance peak for the nonlocal case is blueshifted of $\Delta\hbar\omega = 0.19\,\mathrm{eV}$ with respect to the local case. Panel (b) Radius $a = 25\,\mathrm{nm}$. The nonlocal effects are almost negligible. The numerical data are benchmarked with the analytical results, and the numerical curves overlap the corresponding analytical curves.

evident as before. This is due to the fact that the nonlocal effects become more pronounced when the gas is very confined, that is when the dimension of the structure become comparable with the Fermi wavelength of gold, $\lambda_{\mathrm{F}} = 0.52\,\mathrm{nm}$.
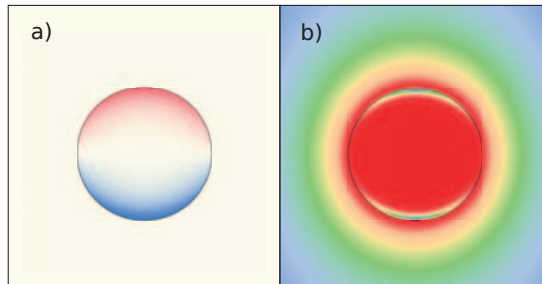
Figure 3.3 Charge density ρ (a) and norm of the electric field $|\mathbf{E}|$ (b) at $\omega_{\mathrm{sp}}^{\mathrm{nloc}} = 6.421\,\mathrm{eV}$ in the nonlocal case.

Fig. 3.3a shows the charge distribution corresponding to the surface plasmon resonance in the nonlocal case. The typical thick-

ness of the surface large layer is of the order of λ_F, and this is a general property of the hydrodynamic model. The blueshift of the surface plasmon resonance is caused by the finite thickness of the charge density, because the distance between charges of opposite sign is smaller respect to the LRA case. This means that the Coulomb forces are more intense, so the work that must be done to separate the charges is higher. The fingerprint of the charge distribution is also evident from the electric-field distribution in Fig. 3.3b.

Another important feature of the nonlocal model is the excitation of longitudinal bulk plasmons for $\omega > \omega_p$ (see par. 2.2.3). We know that in the local case it is possible to excite a longitudinal bulk mode only for $\omega = \omega_p$, while in the nonlocal case there is a numerable infinity of modes for frequencies above the plasma frequency. However, the intensities of the extinction cross section for these modes are low compared to the intensity of the peak of the surface plasmon resonance (see Fig. 3.2).

3.3   Scattering from dimers

The case of dimers is more interesting for applications, because dimers can concentrate a high amount of energy in their gaps, that can lead to an enhancement of the electric field of many orders of magnitude with respect to the incoming field. This phenomenon is called *Field Enhancement*, and it is very important for example for chemical sensing based on SERS spectroscopy (see Chap. 4).

Figure 3.4 shows the systems that we analyzed with our code: the cylindrical dimer and the bow-tie dimer in vacuum.

The information about the surface plasmon excitations are obtained from the spectrum of the extinction cross section σ_{ext}. The extinction power is obtained by integrating the expression (3.2.1) along a circular path that surrounds the dimer. If we introduce the quantity γ (not to be confused with the Drude damping parameter):

$$\gamma(\mathbf{r}) = \frac{|\mathbf{E}(\mathbf{r})|^2}{E_i^2},$$

we can then define the field enhancement in the gap as the line-
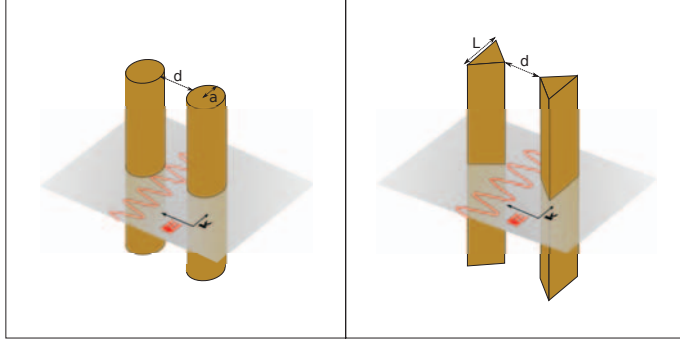
Figure 3.4 Cylindrical dimer (left) and bow-tie dimer (right). The incoming field is TM-polarized.

average value of γ along the axis ℓ of the dimer:

$$\langle \gamma \rangle = \frac{\int_\ell d\mathbf{r}\, \gamma(\mathbf{r})}{\int_\ell d\mathbf{r}} = \frac{1}{E_0^2 d} \int_\ell d\mathbf{r}\, |\mathbf{E}(\mathbf{r})|^2.$$

The choice of the integration path is arbitrary, and it is justified by the fact that the fundamental mode is strongly localized in the gap, along the axis of the dimer.
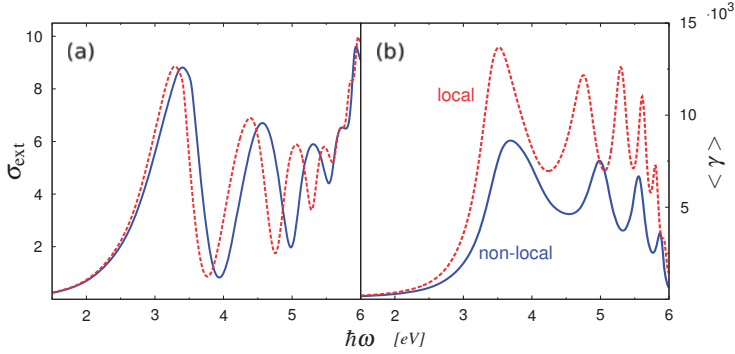

Figure 3.5 Cylindrical dimer. Panel (a) Extinction cross-section. The main resonance peak for the nonlocal case is blueshifted of $\Delta \hbar \omega = 0.12\,$eV with respect to the local case. The blueshift is a function of frequency. Panel (b) Field enhancement. Blueshift of the main resonance and reduction $\Delta \langle \gamma \rangle = 5.4 \cdot 10^3$ of the enhancement factor for the nonlocal case.

Figure 3.5 shows the extinction cross section and the field enhancement for two gold cylindrical nanowires of radius $a = 25\,$nm, separated by a gap of size $d = 1$ nm. In this case there is a

strong coupling between the two wires, and the modes of the isolated nanowires hybridize. The field is strongly localized into the gap. From Panel (a) in (3.5), it can be seen that the main surface plasmon resonance (SPR) occurs at 3.28 eV in the local case, and 3.40 eV in the nonlocal case, that accounts for a blueshift of $\Delta\hbar\omega = 0.12$ eV. The high order modes appear to be more blueshifted than the fundamental one. This is due to the fact that high modes are *multipolar*, and complex charge distributions may be associated with them, giving rise to different energy absorption.

The field enhancement factor $\langle\gamma\rangle$ is depicted in Panel 3.5b, and it also shows the blueshift of the resonance peaks, but the main point here is that the peak associated with the main SPR is reduced by the nonlocal effects. In fact, $\langle\gamma\rangle = 1.4 \times 10^4$ for local response, and $\langle\gamma\rangle = 8.6 \times 10^3$ for nonlocal response. This is due to the fact that the field intensity at resonance is smaller for the nonlocal case (see Fig. 3.6). However, this is not always the case because the value of $\langle\gamma\rangle$ is higher for the nonlocal case at some fixed frequencies. This is an effect due to our arbitrary choice of the integration path for averaging γ. At high frequencies, the modes are not confined along the dimer axis (see fig 3.7), so it may happen that the intensity of the electric field along the path ℓ is higher for the nonlocal case.
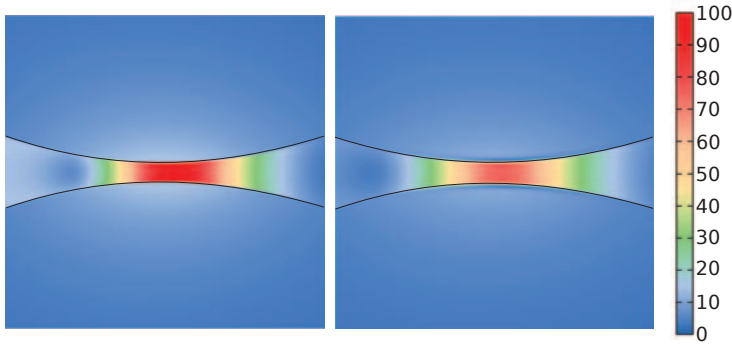

Figure 3.6 Cylindrical dimer, main SPR, intensity of the normalized electric field $|\mathbf{E}|/|\mathbf{E}_i|$. Left: local case. Right: nonlocal case. The field intensity and its spatial distribution are different in the two cases. The asymmetry is due to the fact that the light comes from the left side.

The case of the gold bow-tie dimer is presented in Fig. 3.8. The dimer is made of two equilateral triangular nanorods with sides
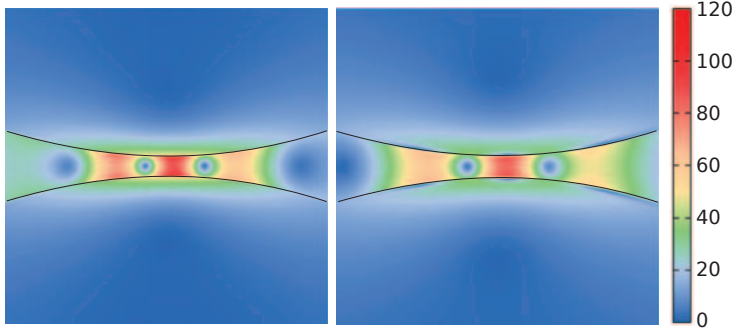
Figure 3.7 Cylindrical dimer, intensity of the normalized electric field $|\mathbf{E}|/|\mathbf{E}_i|$ at $5.1\,\mathrm{eV}$, where $\langle\gamma\rangle_{\mathrm{loc}} \approx \langle\gamma\rangle_{\mathrm{nloc}}$ (see Fig. 3.5). Left: local case. Right: nonlocal case. The electric field $\mathbf{E}_i$ comes from the left side.

$L = 45\,\mathrm{nm}$. The tips of the triangle are rounded with a radius of curvature $r = 1\,\mathrm{nm}$, and the gap distance between the nanowires is $d = 1\,\mathrm{nm}$. The rounding of the tips is needed in order to remove
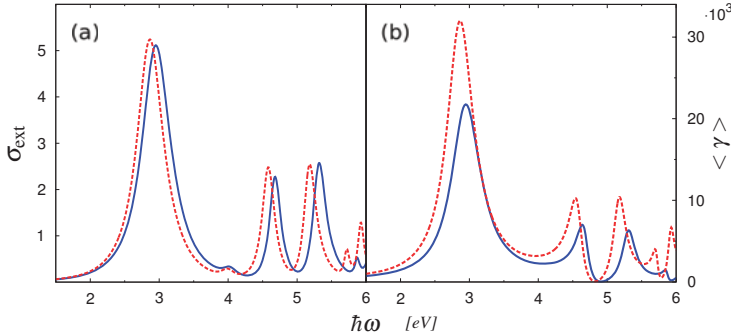

Figure 3.8 Bow-tie dimer. Panel (a) Extinction cross-section. The main resonance peak for the nonlocal case is blueshifted of $\Delta\hbar\omega = 0.10\,\mathrm{eV}$ with respect to the local case. The blueshift is a function of frequency. Panel (b) Field enhancement. Blueshift of the main resonance and reduction of the enhancement factor $\Delta\langle\gamma\rangle = 1.03\cdot 10^4$ in the nonlocal case.

the sharp tip singularity and make the local simulations converge. Indeed, the local simulations were often the more challenging ones, once our nonlocal program was written.

The results mimic very closely those for the circular dimer. A strong interaction between the plasmon modes localized on the tips is observed, and the surface plasmon hybridization occurs. The SPR peak in the nonlocal case is blueshifted, and the main SPR appears at $2.86\,\mathrm{eV}$ for local, and at $2.96\,\mathrm{eV}$ for the nonlocal re-

sponse. The field enhancement for the bow-tie dimer is higher than for the cylindrical dimer, because of the well-known ability of sharp tips of confining the electromagnetic field. The enhancement factor is $\langle\gamma\rangle = 3.2 \times 10^4$ in the local case, and $\langle\gamma\rangle = 2.17 \times 10^4$ in the nonlocal case.
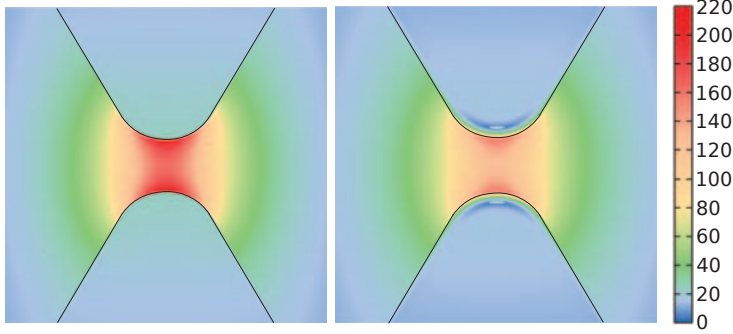
Figure 3.9 Triangular dimer, main SPR, intensity of the normalized electric field $|\mathbf{E}|/|\mathbf{E}_i|$. Left: local case. Right: nonlocal case. The field intensity and its spatial distribution are different in the two cases. The fingerprint of the spatially non-singular charge distribution is clearly visible in the nonlocal case.

In general, the nonlocal effects fade out as soon as the distance between the wires is increased. This is discussed in detail in Paper B (p. 79).

3.4   Numerical convergence analysis

In this section we analyze the convergence of the numerical code for nonlocal response in metallic nanostructures. This was done by studying the convergence of both the extinction cross section and the enhancement factor as the mesh density on the surfaces of the structures changes. Before doing that, we introduce the important parameters that define the physical and numerical validity of our model.

3.4.1   Physical and numerical consistency

Energy conservation is an essential property of electromagnetic system, so it is an important parameter that must be kept under control during the simulations. The energy conservation is stated by

the Poynting theorem. We briefly recall the statement of the theorem, and the quantities that were checked for physical consistency. The Poynting vector in the frequency domain is defined as:

$$\mathbf{S} = \frac{1}{2}\mathbf{E} \times \mathbf{H}^*.$$

If we calculate the divergence of $\mathbf{S}$, and use Maxwell's equations, we get:

$$\nabla \cdot \mathbf{S} = -2\omega i\left(\frac{1}{4}\epsilon_0\mathbf{E}^2 - \frac{1}{4}\mu_0\mathbf{H}^2\right) - \mathbf{E} \cdot \mathbf{J}^*.$$

This is a general definition, that shows the electromagnetic energy balance in every point in space. We want to apply this energy balance to our system that is made of a metallic structure in space, and it is illuminated by an EM field. If the space is filled with a lossless medium, we can define a generic closed surface that surrounds the metallic structure, and study the energy exchange through this boundary. The current density vector $\mathbf{J}$ is the polarization current in our next considerations, as we did not consider injected currents in this work. We can thus write:

$$\int_{\partial V} \mathbf{S} \cdot \hat{n}\, d\sigma + 2\omega i \int_V \left(\frac{1}{4}\epsilon_0\mathbf{E}^2 + \frac{1}{4}\mu_0\mathbf{H}^2\right) dV - \frac{1}{2}\int_V \mathbf{E} \cdot \mathbf{J}^*\, dV = 0,$$

where V is the volume enclosed by the surface ∂V. This is a complex quantity, and if we separate the real and imaginary part, we get:

$$\int_{\partial V} \Re\{\mathbf{S}\} \cdot \hat{n}\, d\sigma + \frac{1}{2}\int_V \Re\{\mathbf{E} \cdot \mathbf{J}^*\}\, dV = 0$$

$$\int_{\partial V} \Im\{\mathbf{S}\} \cdot \hat{n}\, d\sigma + 2\omega \int_V \left(\frac{1}{4}\epsilon_0\mathbf{E}^2 - \frac{1}{4}\mu_0\mathbf{H}^2\right) dV +$$

$$+ \frac{1}{2}\int_V \Im\{\mathbf{E} \cdot \mathbf{J}^*\}\, dV = 0.$$

$$(3.4.1)$$

The first equation states the conservation of the *real power*, that is the power dissipated by the Joule effect in the metal. The second term states the conservation of the *reactive power*, that takes into account for the balance between the electric and magnetic energy in the volume V. The conservation of both the real power and

reactive power are the parameters for physical consistency that are checked during the simulations.

The linearization procedure that we developed in the previous chapter is valid as soon as the perturbed charge density ρ is much smaller than the charge density at rest ρ_0. The ratio $|\rho/\rho_0|$ is a function of the incoming field intensity $\mathbf{E}_\mathrm{i}$. The condition of mathematical consistency at a given field intensity to be checked during the simulations is:

$$\max_\Omega \left| \frac{\rho}{\rho_0} \right| \ll 1. \tag{3.4.2}$$

3.4.2   Convergence tests

As we have discussed earlier, the external electric field excites the charges in the metal that localize to a region of thickness $\approx \lambda_F$ about the surface of the structures. This is true for frequencies lower than ω_p, where only surface plasmons are present. In these cases, the meshing of the surfaces is of crucial importance for obtaining the convergence of our model because a sensitive variation of the observables with the size of the surface meshes is expected [66]. For this reason, we study the variation of these parameter as the number of edge elements n changes, with all the other meshed geometrical entities fixed. The edge elements are the elements that lie on the surface of the structure, and they provide a measure of the mesh density at the surface. The convergence tests are conducted at the fundamental resonance frequency for all the structures. The observables that we consider here are the extinction cross section σ_ext and the enhancement factor $\langle \gamma \rangle$. We define the relative error:

$$\delta_\mathrm{x}^\mathrm{num} = \frac{|x_\mathrm{mesh} - x_\mathrm{reg}|}{x_\mathrm{reg}} \cdot 100 \tag{3.4.3}$$

where x can be either σ_ext or $< \gamma >$. The observable value x_mesh is the value at a fixed mesh edge number, and x_reg is the value at convergence regime.

The first example that we consider is the convergence of the extinction cross section for the case of the circular nanowire in the hydrodynamic model. In this case, we have the possibility to benchmark the numerical solutions with the analytical ones, that were calculated by Ruppin in the paper [64]. The benchmarking is very satisfactory because the results show a very good agreement
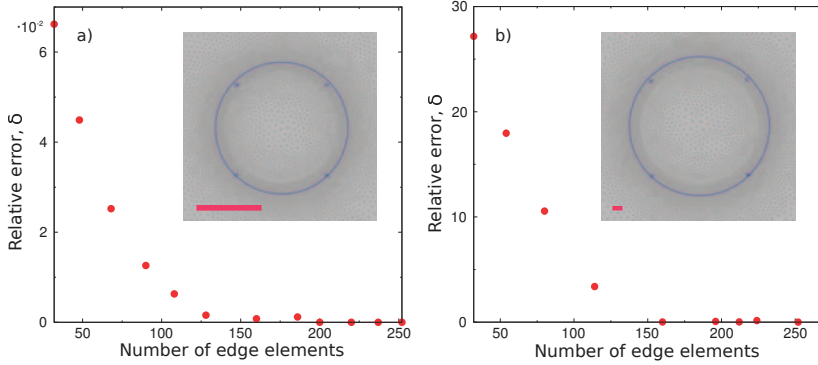
Figure 3.10 Relative error $\delta_{\text{ext}}^{\text{num}}$ of the extinction cross section versus number of edge element for cylindrical nanowires. Panel (a) Cylinder of radius $R = 2$ nm. The convergence occurs for $n > 150$, but it is already small (0.066%) at $n = 32$. Panel (b) Cylinder of radius $R = 25$ nm. The convergence occurs for $n > 150$. The insets show the mesh densities. The scale bars are 2 nm long.

between both kinds of data, as shown in fig. 3.2. The benchmarking procedure is described in Paper B (p. 79).

The outcomes of our current convergence analysis are shown in fig. 3.10, that presents the cases of the cylinders with radii $R = 2$ nm and $R = 25$ nm respectively. The only observable in this
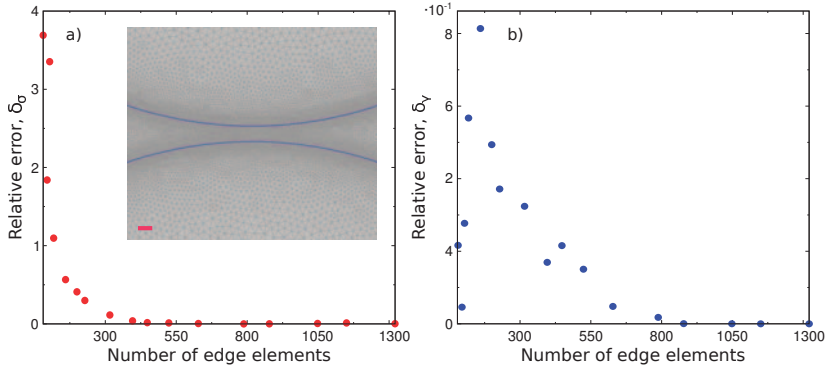
Figure 3.11 Relative errors for the cylindrical dimer versus number of edge elements at the cylinders surface. Panel (a) $\delta_{\text{ext}}^{\text{num}}$, the convergence occurs for $n > 550$. Panel (b) $\delta_{\gamma}^{\text{num}}$, the convergence occurs for $n > 800$. The inset shows the mesh density in the gap. The scale bar is 1 nm long.

case is σ_{ext}, and the convergence parameter is $\delta_{\text{ext}}^{\text{num}}$ of eq. (3.4.3). It can be seen that the case of the nanowire with radius $a = 2$ nm, the convergence is reached easily. The value of $\delta_{\text{ext}}^{\text{num}}$ is already 0.066%

with only 32 edge elements. The convergence is reached at 250 elements, and the simulation lasts less than one minute.

The intensity of the incoming field is $\mathbf{E}_i$ is $1\,\text{V/m}$, that corresponds to a power density $\mathbf{S}_i$ of $2.7 \cdot 10^{-3}\,\text{W/m}^2$, that is much smaller of the typical power density needed to excite nonlinear effects in nanostructures [22]. Indeed, the condition of numerical consistency (NC) defined in eq. (3.4.2) is fulfilled, because $|\rho/\rho_0| < 1.356 \cdot 10^{-9}$ on the domain at the convergence regime. The reactive power balance (RPB) in eq. (3.4.1) value is $2.9 \cdot 10^{-17}\,\text{var}$, and the active power balance (APB) is $2.59 \cdot 10^{-19}\,\text{W}$ at regime. These can be considered as numerical zeros.

The case of a nanowire with radius $a = 25$ nm is reported in fig. 3.10b. It can be noticed that the $\delta_{\text{ext}}^{\text{num}}$ value converges more slowly, starting from a value of $\approx 30\%$. The observable σ_{ext} converges for edge numbers bigger than 150. The intensity of the incoming field $\mathbf{E}_i$ is $1\,\text{V/m}$ also in this case, and the corresponding value of $|\rho/\rho_0|$ at convergence regime is smaller than $8.146 \cdot 10^{-11}$, so the NC condition is fulfilled. The RPB value is $4.90 \cdot 10^{-18}$ var, and the APB is $8.41 \cdot 10^{-19}$ W. These can also be considered numerical zeros. The simulation time is about $1\,\text{min}$.

The case of cylindrical nanowire dimers is described in fig. 3.11, that shows the convergence study for σ_{ext} in Panel (a) and the $\langle \gamma \rangle$ factor in Panel (b). The number of edge elements is relative to the surface of the structures facing each other. It can be seen that the convergence of the extinction cross section occurs at a lower number of edge elements as compared to the enhancement factor. This is due to the fact that a high number of mesh elements is needed in the gap in order to reach convergence. The convergence of σ_{ext} occurs at about 550 elements, while $\langle \gamma \rangle$ convergences at about 800 elements. The intensity of the incoming field is $\mathbf{E}_i$ is $1\,\text{V/m}$, and the corresponding value of the ratio $|\rho/\rho_0|$ is smaller than $8.8743 \cdot 10^{-10}$ at regime, so the NC condition is fulfilled also for a high field enhancement factor. The value of the RPB is $1.77 \cdot 10^{-18}$ var, and the value of the APB is $3.2796 \cdot 10^{-19}$ W, so the physical consistency conditions are fulfilled as well. The simulation time is about $5\,\text{min}$.

Finally, we examine the case of the bow-tie dimer. The convergence tests are shown in fig 3.12. As in the previous case, Panel (a) shows the convergence for σ_{ext}, and Panel (b) shows the con-
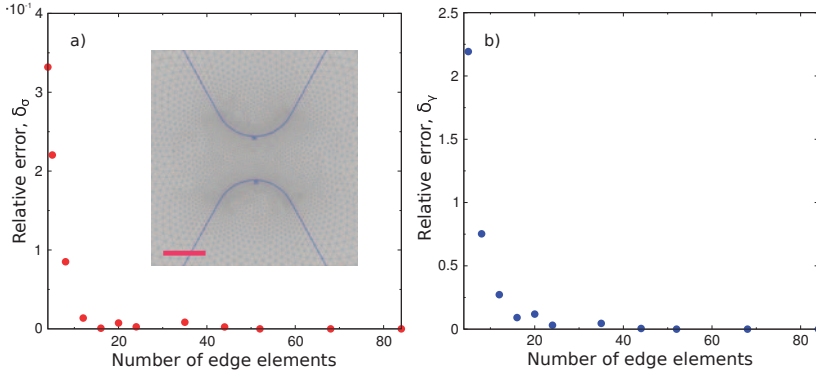
Figure 3.12 Relative errors for the bow-tie dimer versus number of edge elements at the triangles tip. Panel (a) $\delta_{\text{ext}}^{\text{num}}$, the convergence occurs for $n > 400$. Panel (b) $\delta_{\gamma}^{\text{num}}$, the convergence occurs for $n > 800$. The inset shows the mesh density in the gap. The scale bar is $1\,\text{nm}$ long.

vergence test for $\langle\gamma\rangle$. The observable σ_{ext} converges much faster than $\langle\gamma\rangle$, as in the case of the cylindrical dimer. It can be seen that σ_{ext} converges for $n > 400$, while $\langle\gamma\rangle$ convergences for $n > 800$. However, the variations are pretty small, also for smaller n. The intensity of $\mathbf{E}_i$ is again $1\,\text{V/m}$, and the ratio $|\rho/\rho_0|$ is smaller than $2.19 \cdot 10^{-9}$ on the domain at convergence regime, so the NC condition is fulfilled also in this case. The value of RPB is $2.43 \cdot 10^{-17}$ var, while the value of APB is $1.15 \cdot 10^{-19}$ W at convergence regime. These can also be considered as numerical zeros. The simulation time is about $5\,\text{min}$.

4

Field enhancement in the HD model and its application to SERS

In this chapter we will discuss about an important consequence of the finite extension of the surface charges in the hydrodynamic model: the ability to calculate fields near sharp tips where the classical model gives divergent results. This has a great impact on the understanding of the field enhancement phenomenon, and casts new light on the fundamental limitations of the field enhancement of the Raman signal that occur in the Surface-Enhanced Raman Spectroscopy. The results we will show are published in Paper C (p. 93).

4.1 Resolution of sharp tips

The numerical solutions of Maxwell's equations is not always defined in proximity of very sharp corners or edges. This is the usual case of local media, where the polarization charges are distributed as a delta function on the surface of the medium. To obtain convergent field distributions, the procedure used in local response is the smoothening of the sharp features by introducing a curvature radius r, and this is usually supported by the fact that the physical structures do not present infinitely sharp features [67,68]. However, the state-of-the-art fabrication techniques in nanoplasmonic allow to produce devices with very sharp tips, so it can be important to include sharp features in the simulations. Moreover, the simulation of sharp features allows us to perform "limit-procedure" analysis, where we study the ultimate theoretical values of a given quantity as the curvature radius r goes to zero. This is the case for the

field enhancement in this chapter and of the mode area in the next chapter.

As we have seen in the previous discussions (par. 2.2.3 and sec. 3.2), in the HD model the charges are distributed on the surface as an ordinary function, and the extension of the charge layer is of the order of λ_F for surface plasmons. This causes the field to be smeared out on a layer surrounding the surface of the structure, and it ultimately removes the singularities on sharp corners.

We perform a numerical experiment to show this effect by simulating the scattering from a gold triangular nanowire, as depicted in fig. 4.1. The triangle is equilateral with side length $L = 45\,\text{nm}$, and the incoming electric field is linearly polarized, and directed along the height of the triangle, in order to excite the plasmon localized on the tip.
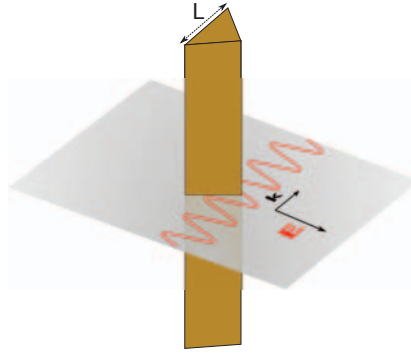

Figure 4.1 Triangular nanowire. The incoming field is TM polarized and it is parallel to the height of the triangular cross-section of the wire, in order to excite the plasmon localized on the tip.

The main surface resonance for this structure occurs at $\hbar\omega = 3.72\,\text{eV}$, and the electric field is localized on the tip of the triangle (see fig. 4.2). This simulation is supported by the convergence study of the extinction cross section. In this case, the σ_{ext} is normalized to the triangle side L, $\sigma_{\text{ext}}(\omega) = \frac{|P_{\text{ext}}|}{2LI_0}$. The value of σ_{ext} at the main resonance peak is 2.450. The same structure cannot be simulated in the LRA because the computation does not converge.
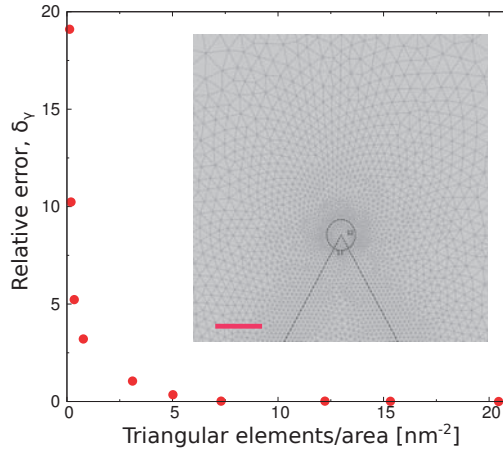
4.1.1   Convergence tests

A careful converge study is performed in this case. The areas that need to be meshed accurately are the triangle tips. We devise an
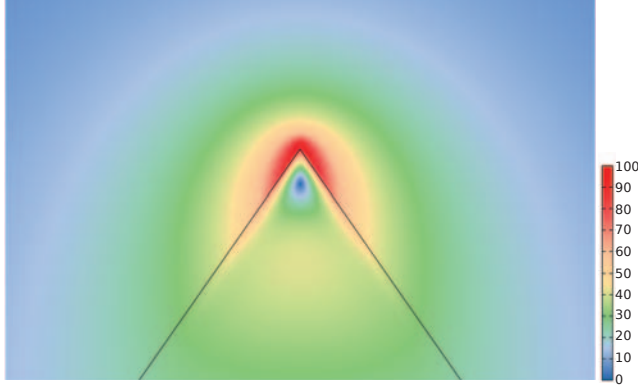
Figure 4.2 Intensity of the normalized electric field $|\mathbf{E}|/|\mathbf{E}_i|$ at resonance frequency $\hbar\omega = 3.72\,\text{eV}$. The field is localized on the tip surface. The fingerprint of the surface charges is clearly visible.

ad-hoc procedure that consists into defining circular neighborhoods of the tips enclosing a constant number of triangular elements, $n = 244$, and varying the the radii of the circles from $R_{\text{mesh}} = 25\,\text{nm}$ to $R_{\text{mesh}} = 0.3\,\text{nm}$. We expect that σ_{ext} would converge as we

Figure 4.3 Convergence test for the triangular nanowire. The radius of the circle varied, while the number of elements within a circle was kept constant. The picture shows the case $R_{\text{mesh}} = 0.3\,\text{nm}$. The converge occurs for $R_{\text{mesh}} \approx 3\,\text{nm}$, corresponding to $\bar{n} = 8$. The scale bar is $1\,\text{nm}$ long.

approached the usual size of the localized charges, that is $\approx \lambda_F$. The results are shown in fig. 4.3, where we represent the numerical error δ_γ defined in eq. (3.4.3), against the number of triangular

elements contained in the circle per unit of area, $\overline{n}$. The plot clearly shows that the convergence is obtained for $\overline{n} > 8$, that corresponds to a radius $R_{\text{mesh}} \approx 3\,\text{nm}$. The intensity of the incoming field $\mathbf{E}_i$ is $1\,\text{V/m}$, and the corresponding value $|\rho/\rho_0| < 2.9 \cdot 10^{-9}$ at convergence regime, so the NC condition is fulfilled. The conditions of physical consistency are also fulfilled because RPB is $1.45 \cdot 10^{-17}$ var, while the value of APB is $2.48 \cdot 10^{-19}$ W at $R_{\text{mesh}} = 0.3\,\text{nm}$. The simulation time is about $5\,\text{min}$

4.2   Surface-Enhanced Raman spectroscopy: an introduction

Before discussing the application of the sharp tip resolution to the study of metallic nanostructures for SERS, let us briefly recall the concepts of Raman effect and Surface-Enhanced Raman Spectroscopy [69], [70], [71].

The Raman effect is a scattering process between a photon and a molecule. Incident photons ω_L are inelastically scattered from a molecule and shifted in frequency by the energy of its characteristic molecular vibrations ω_M. Frequency-shifted scattered photons can occur at lower and higher energy relative to the incoming photons, depending on whether they interacted with a molecule in the vibrational ground state or in an excited vibrational state. In the first case, photons lose energy by exciting a vibration and the scattered light appears at a lower frequency ω_S, called Stokes scattering. By interacting with a molecule in an excited vibrational state, the photons gain energy from the molecular vibrations and the scattered signal appears at higher frequency ω_{aS}, called anti-Stokes scattering. The Raman effect probes the vibrational levels of the molecule, and the Raman spectrum provides a fingerprint of its structure. The intensity of the Raman signal $P^{RS}(\omega_S)$, can be written in this way:

$$P^{\text{RS}}(\omega_S) = N\sigma_{\text{free}}^{\text{R}}I(\omega_L),$$

where $\sigma_{\text{free}}^{\text{R}}$ is the Raman cross section, $I(\omega_L)$ the intensity of the excitation field, N is the number of molecules probed in the volume. The typical Raman cross sections per molecule range between 10^{-30} and $10^{-25}\,\text{cm}^2$, which is very small if compared with the usual fluorescence cross sections, that are of the order of $10^{-16}\,\text{cm}^2$. Thus, the intensity of a Raman signal of a *free* molecule is very low.

Nonetheless, if the molecules are adsorbed on a metallic struc-
ture, a strong Raman signal can be detected, and this is due to the
interaction of the molecule with the metallic surface. In principle,
two effects can be recognized in this case:

- *Electromagnetic effect.* The Raman scattering takes place in
  the enhanced local optical fields due to the excitation of sur-
  face plasmon polaritons on the metallic surface.

- *Chemical effect.* A molecule in contact with a metallic surface
  exhibits a cross section that is larger than the cross section
  of the free molecule. This is due to the fact that a charge
  transfer between the molecule and the metal occurs, and this
  may alter the polarizability of the molecule and increase the
  Raman-scattering efficiency.

This can be summarized by the formula:

$$P^{\text{SERS}}(\omega_S) = N'\sigma_{\text{ads}}^{\text{R}}|A(\omega_L)|^2|A(\omega_S)|^2 I(\omega_L), \qquad (4.2.1)$$

where N' is the number of molecules that are involved in the SERS
process, and can be smaller than the number of molecules in the
probed volume N. The cross section $\sigma_{\text{ads}}^{\text{R}}$ describes an increased
cross section of the new Raman process of the adsorbed molecule.
The factor $A(\omega)$ is the local field enhancement factor due to the
plasmon excitation, defined as:

$$A(\omega) = \frac{|\mathbf{E}(\omega)|}{|\mathbf{E}(\omega)_0|}.$$

The term $A(\omega_L)$ denotes the enhancement of the excitation signal,
and $A(\omega_S)$ expresses the enhancement of the Raman scattered light
by the molecule. The SERS enhancement is particularly strong
when both the excitation and the scattered fields are in resonance
with the surface plasmons. The frequency shift between the excita-
tion and scattered light is usually small compared with the width of
the plasmon resonance, so we can say that $A(\omega_L) \approx A(\omega_S)$. Then,
equation (4.2.1) can be rewritten as:

$$P^{\text{SERS}}(\omega_S) = N'\sigma_{\text{ads}}^{\text{R}}|A(\omega_L)|^4 I(\omega_L),$$

so the Raman signal intensity is proportional to the *fourth* power
of the enhancement of the local incident near field.

The earliest sensing experiments showed a modest enhancement of the SERS signal with respect to the 'normal' RS signal, of the order of 10^4 to 10^6. Recent experiments have reported much higher enhancements, of the order of 10^{14} [71]. However, the relative importance of the electromagnetic and chemical effects is still not clear because both the chemical and the electromagnetic effects involved in SERS are difficult to quantify.

The usual theoretical approach for the assessment of the electromagnetic contribution to the field enhancement is based on the Drude model (LRA). As we discussed above, a rounding of the sharp tips or edges is needed in order to make the simulations converge. Unfortunately, the field intensity is strongly affected by the variations of the curvature angle r, and it diverges as $r \to 0$ [72]. This unlimited increase in the electric field intensity does not allow to determine the maximum enhancement of the Raman signal that can be reached by means of the electromagnetic field enhancement.

This is where the nonlocal effects come into play, and can provide us with an answer.

4.3   Groove structure for SERS applications

In SERS, the molecules under test are usually adsorbed on surfaces of copper, silver or gold that are rough at the nanometer scale. This surface roughness can be modeled by means of a periodic structure of infinitely long metallic half-cylinders of radius R, resting shoulder-by-shoulder on a semi-infinite metal film (fig. 4.4). This is called groove structure, and it reproduces the large curvature areas and small interstices that are expected to generate a large local field enhancement.

This structure was initially proposed and studied by García-Vidal and Pendry [73], to explain qualitatively the electromagnetic origin of the large enhancement factors observed experimentally. Near the bottom of the groove, the surfaces of the two touching half-cylinders become tangential to each other and a field singularity forms within the traditional LRA of the dielectric function. As we stated in the previous subsection, a rounding r of this point is needed in order to prevent the field from growing indefinitely. We
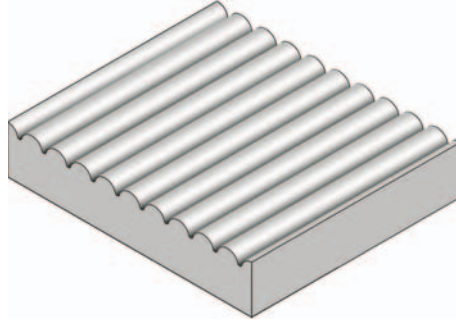
Figure 4.4 A section of the groove structure for SERS applications. The structure is indefinitely extended in all directions.

write here the definition of SERS enhancement factor γ :

$$\gamma(\mathbf{r}, \omega) = A(\mathbf{r}, \omega)^4 = \frac{|\mathbf{E}(\mathbf{r}, \omega)|^4}{|\mathbf{E}_0(\omega)|^4},$$

where we indicated the dependence of all the quantities on the position. The parameter that we consider here is the surface averaged field enhancement factor $\langle\gamma\rangle$, that is defined as:

$$\langle\gamma\rangle(\omega) = \frac{1}{L} \int_L \gamma(\mathbf{r}, \omega) \, d\mathbf{r},$$

where L is a period of the groove structure. This definition is based on the assumption that the molecules under test are adsorbed on the surface, and they experience the local field on the surface.

We excited the structure by means of a plane wave $\mathbf{E}_0(\omega)$ normal to the substrate, with the electric field polarized across the groove section, as it is shown in fig. 4.5a [48]. The structure is made of silver, and the interband effects are included in this case. The simulation parameters are obtained from [74]. All the simulations are performed in the visible frequency band $[400, 800]$ nm, that is relevant for the SERS applications.

Fig 4.6 presents the results of two studies that show the relative importance of the nonlocal effect as the curvature angle r becomes comparable with λ_F. The $\langle\gamma\rangle$ factor is the same for $r = 5$ nm for both LRA and HD model. The nonlocal effects are clearly visible when $r = 0.1$ nm. The fundamental dipolar mode occurs at $\lambda = 700.88$ nm for the HD model, and it is blueshifted of $\Delta\lambda =$
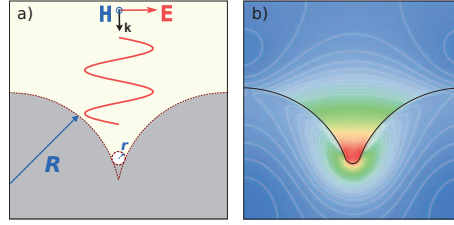
Figure 4.5 Panel (a) Unit cell of the groove structure, with geometrical parameters and incident field polarization. Panel (b) Typical electric field intensity in the groove crevice.
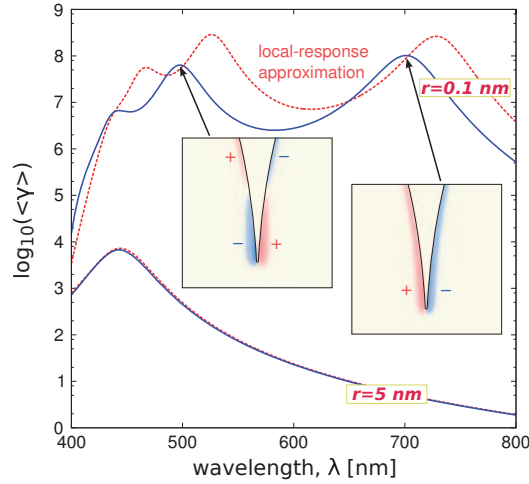
Figure 4.6 Blueshift of the main resonance peak and field enhancement reduction due to the nonlocal effect. The picture shows the case of a groove with $R = 75$ nm. The effect of spatial nonlocalities is negligible for $r = 5$ nm, while it is visible for $r = 0.1$ nm. The fundamental dipolar mode occurs at $\lambda = 700.88$ nm for the HD model, and the wavelength blueshift is $\Delta\lambda = 27.534$ nm. The insets show the charge distributions corresponding to the two resonance peaks.

27.534 nm with respect to the local case. The field enhancement factor $\langle\gamma\rangle$ in the HD model is $1.02 \cdot 10^8$ and it is smaller than the relative value in the LRA model. The difference $\Delta\langle\gamma\rangle$ between the values of $\langle\gamma\rangle$ is $1.62 \cdot 10^8$. Fig. 4.7 is very important because it shows the highest value of $\langle\gamma\rangle$ that can be reached in the HD model when $r \to 0$ for an array of cylinders with radius $R = 15$ nm. The picture shows a monotonic behavior that saturates when $r = 0$, and it reaches the enhancement $\langle\gamma\rangle = 1.52 \cdot 10^9$ at $\lambda = 707.78$ nm.

The final analysis consists into studying the ultimate field en-
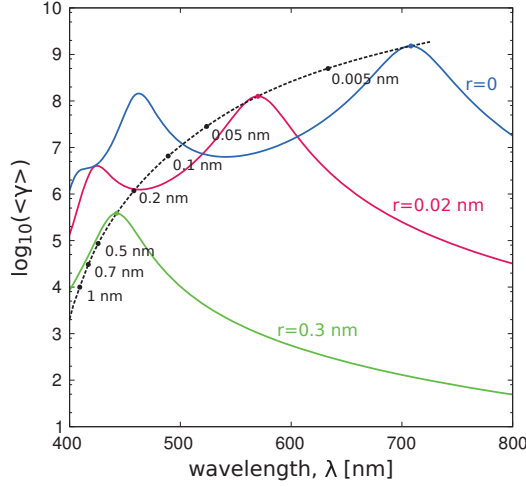
Figure 4.7 Variation of $\langle\gamma\rangle$ as r changes in $[0, 1]$ nm for a groove made of cylinders with radius $R = 15$ nm in the HD model. The main resonance peaks are redshifted, and the maximum $\langle\gamma\rangle$ value saturates to the value $1.72\cdot 10^9$ at $\lambda = 707.78$ nm for $r = 0$.

hancement that can be reached by varying R, while keeping $r = 0$. The results are presented in fig. 4.8, that shows the *maximum field enhancement* that can be reached with a groove structure. This corresponds to a structure with $R = 120$ nm, and it occurs at $\lambda = 765.43$ nm. The value of $\langle\gamma\rangle$ is $1.72\cdot 10^9$. This value of the maximum $\langle\gamma\rangle$ is still far from the enhancement of the Raman signal present in the literature, that is of the order of 10^{14}. This means that there must be an important contribution from the chemical effect to the high signal enhancement that occurs in SERS.

4.3.1 Convergence tests

The converge test for the groove structure is very similar to the one we performed for the triangular nanowire in the previous section. The surface charges tend to localize on the two cylindrical surfaces that border the crevice of the groove, so the side extension of the distribution is bigger. In this case, we defined a circular neighborhood of the tangent point of the two cylinders, and we varied the number n of triangular elements in this circle.

The example we consider here is a groove structure with $R = 75$ nm, with $r = 0$, that is included in the study of fig. 4.8. The main resonance frequency occurs at $\lambda = 668.734$ nm and the value
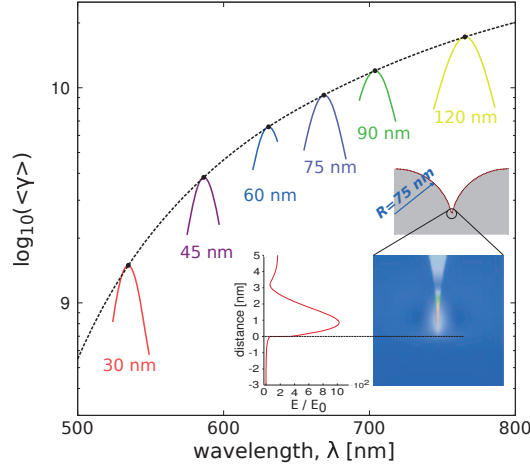
Figure 4.8 Maximum field enhancement factor that can be reached with a groove structure in the HD model. The picture shows the variations of $\langle\gamma\rangle$ as a function of R, when $r = 0$. The maximum value is smaller than $2\cdot 10^{10}$.
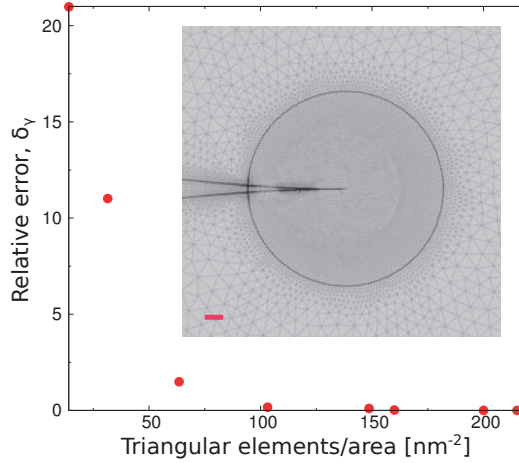
Figure 4.9 Convergence test for the groove structure. The radius of the circle is $R_{\mathrm{mesh}} = 5\,\mathrm{nm}$, and the number of triangular elements varied from $n = 1100$ to $n = 16800$. The convergence occurs for $n > 7800$.

of the field enhancement factor $\langle\gamma\rangle$ is $9.31\cdot 10^9$. We defined a circle of radius $R_{\mathrm{mesh}} = 5\,\mathrm{nm}$, that encloses the surface charges on the cylindrical surface in the crevice, and we varied the number of triangular elements n from 1100 to 16800. The results are shown in fig. 4.9, and the convergence occurs for $n > 7800$ elements. The intensity of the incoming field $\mathbf{E}_0$ is $1\,\mathrm{V/m}$, and the corresponding

value of $|\rho/\rho_0|$ is smaller than $5.75 \cdot 10^{-9}$ at regime, so the NC condition is fulfilled. The value of RPB is $1.31 \cdot 10^{-17}$ var, while the value of APB is $3.11 \cdot 10^{-19}$ W at $n = 16800$. The integration path for the power flux calculation was arbitrarily chosen as a line that encloses a period of the groove (it passes through the metal). The simulation time is about $5\,\mathrm{min}$

5

Hydrodynamic theory for plasmonic waveguides

In this chapter we will study an important application of surface plasmon polaritons: plasmonic waveguides. The surface plasmons that we studied in chapter 3 and 4 are "localized", and the plasma oscillation are stationary waves. We have seen that this has many interesting applications, but this is not the full story. Plasmons can also be propagating waves, and this is one of the most promising applications to the field of optoelectronics and telecommunications. We will analyze waveguides that show high field confinement, such as nanowires, grooves and edges for which the nonlocal effects are important. The results we will show are issued in Paper D (p. 97).

5.1   Plasmonic waveguides

Before starting our discussion on the hydrodynamic theory of plasmonic waveguides, let us briefly review different types of plasmonic waveguides and their application. In the introduction of this thesis, we talked about the ability of surface plasmon polaritons of focusing light beyond the diffraction limit. We have seen some examples in the previous chapters concerning the confinement of energy in gap regions between nanorods (Chapter 3) or in groove crevices (Chapter 4). In this chapter, beside the focusing properties of SPP, we also consider the ability of surface plasmon polaritons of carrying energy between two given points of an optical circuit. The metallic devices that support these propagating modes are called *plasmonic waveguides*.

Various types of plasmonic waveguides have been proposed for guiding SPP, and these include, for example, thin metal films [75, 76], chains of metal nanoparticles [77–79], cylindrical nanorods [80], metal nanostrips on a dielectric substrate [81–84], sharp metallic wedges [85–89], nanogrooves in metallic substrates [88–93]. For plasmonic waveguides, focusing refers to the ability of laterally confining light, i.e. orthogonally to the propagation direction. There is usually a trade-off between lateral field confinement and propagation distance for these guides, so not all of them can focus light in the same way [9]. For example, metal nanostrips on a metallic substrate are long-range guides. This is due to the fact that most of the energy carried by the SPP modes in these guides is localized into the dielectric substrate, that is usually less lossy then the metallic strip. Moreover, decreasing the thickness of the strip or of the film, causes the field to leak into the dielectric, and this results in poorer localization of the modes. In the telecommunications band $[1300 - 1600]$ nm, the propagation length for the fundamental mode of this guide can be of the order of millimeters, but they are not suitable for integrated optical circuits.

In order to reach a subwavelength focusing of light, guided SPP modes must mainly propagate in the metal, and this unavoidably reduces the propagation length of the guide. Some of the guides we listed above are able to focus light efficiently, but they are affected by high propagation losses. A typical example of this kind of guides is the chain of nanoparticles, that is rather difficult to use for plasmonic interconnects [78]. Cylindrical nanowires are difficult to fabricate, and they are too sensitive to imperfections.

Recently, Λ-wedges and V-grooves have received considerable attention from the plasmonic research community because they are relatively easy to fabricate, and they show very good light confinement and relatively low propagation losses. In particular, at telecommunications frequencies wedge plasmon waveguides show better lateral field localization and less attenuation with respect to the groove waveguides. This means that they are good for optical interconnects of signals in the near infrared. At optical frequencies, the situation is reversed, and V-grooves show better lateral confinement of light, and longer propagation distances [9]. These waveguides find important applications in all areas where nanoscale resolution is essential, such as near-field optical microscopy,

electromagnetic probing of separate molecules and quantum dots, non-linear plasmonics, and nanofocusing [94]

In this chapter, we examine in detail the light confinement and propagation properties of V-grooves, and Λ-wedges in the hydrodynamic model.

5.2   Hydrodynamic wave equation for the electric field

The waveguiding problem is a 3D problem, because all the components of the electric and current density field must be considered. The solutions of the full hydrodynamic system (2.2.8) would be based on the 6 dimensional vector $(\mathbf{E}, \mathbf{J})$, and this can be very difficult to handle numerically. However, it is possible to work the equations out and eliminate the current density vector, and writing a compact equation that contains only the electric field $\mathbf{E}$. We report here all the steps of the derivation.

We start again with the equation of motion (2.2.7):

$$\beta^2 \nabla\nabla \cdot \mathbf{J} + \omega(\omega + i\gamma)\mathbf{J} = i\omega\epsilon_0\omega_p^2\mathbf{E}, \qquad (5.2.1)$$

and recall the definition of displacement vector $\mathbf{D}$ as:

$$\mathbf{D} = \epsilon_0\mathbf{E} + i\frac{\mathbf{J}}{\omega}.$$

If we apply the divergence operator on both sides and we use the fact that $\nabla \cdot \mathbf{J} = i\omega\rho$, where ρ is the polarization charge density, and $\mathbf{D}$ is solenoidal because there are no free charges, then we obtain:

$$\nabla \cdot \mathbf{E} = \frac{\rho}{\epsilon_0},$$

from which we derive the relation:

$$\nabla \cdot \mathbf{J} = i\omega\epsilon_0\nabla \cdot \mathbf{E}.$$

We can substitute this expression in the equation of motion (5.2.1), and isolate $\mathbf{J}$, and obtain:

$$\mathbf{J} = -i\omega\epsilon_0\frac{\beta^2}{\omega(\omega + i\gamma)}\nabla\nabla \cdot \mathbf{E} + i\omega\epsilon_0\frac{\omega_p^2}{\omega(\omega + i\gamma)}\mathbf{E}. \qquad (5.2.2)$$

The term:

$$\chi_{\text{Drude}} = -\frac{\omega_p^2}{\omega(\omega + i\gamma)},$$

is the Drude electric susceptibility. If we define:

$$\vartheta_{\text{HD}} = \frac{\beta^2}{\omega(\omega + i\gamma)},$$

and rewrite (5.2.2) as:

$$\mathbf{J} = -i\omega\epsilon_0\vartheta_{\text{HD}}\nabla\nabla\cdot\mathbf{E} - i\omega\epsilon_0\chi_{\text{Drude}}\mathbf{E},$$

that can be substituted in Maxwell's wave equation and obtain:

$$\nabla\times\nabla\times\mathbf{E} - \epsilon_{\text{Drude}}k_0^2\mathbf{E} = k_0^2\vartheta_{\text{HD}}\nabla\nabla\cdot\mathbf{E}, \qquad (5.2.3)$$

where $\epsilon_{\text{Drude}} = 1 + \chi_{\text{Drude}}$. This equation can be written in a more compact way by using the vector identity $\nabla[\nabla\cdot\mathbf{E}] = \nabla\times\nabla\times\mathbf{E} + \nabla^2\mathbf{E}$:

$$\nabla\times\nabla\times\mathbf{E}(\mathbf{r}) = k_0^2\frac{1}{(1 - k_0^2\vartheta_{\text{HD}})}\hat{\varepsilon}_{\text{NL}}(\mathbf{r})\mathbf{E}(\mathbf{r}),$$

where $\hat{\varepsilon}_{\text{NL}}(\mathbf{r})$ is defined as:

$$\hat{\varepsilon}_{\text{NL}}(\mathbf{r}) = \varepsilon_{Drude} + \vartheta_{\text{HD}}\nabla^2.$$

The term

$$\frac{1}{(1 - k_0^2\vartheta_{\text{HD}})} = \frac{1}{1 - \left(\frac{\beta}{c}\right)^2\frac{\omega}{(\omega + i\gamma)}} \approx 1$$

for noble metals at optical frequencies. The *hydrodynamic wave equation* for the electric field becomes:

$$\nabla\times\nabla\times\mathbf{E}(\mathbf{r}) = \left(\frac{\omega}{c}\right)^2\hat{\varepsilon}_{\text{NL}}(\mathbf{r})\mathbf{E}(\mathbf{r}).$$

This is formally similar to the ordinary Maxwell's equation in a local medium, where all the aspects of the nonlocal response are included in the operator $\hat{\varepsilon}_{\text{NL}}(\mathbf{r})$. We still need an additional boundary condition to solve this equation, because $\hat{\varepsilon}_{\text{NL}}(\mathbf{r})$ is a differential operator. This condition is given in this case by equation (2.2.17), discussed at section (2.2.2), that states the continuity of the normal component of the $\mathbf{E}$ vector.

It is useful to write eq. (5.2.3) in the weak form, in order to implement it in COMSOL Multiphysics. For this reason, we rewrite the equation (5.2.3) in the weak form.

Before doing that, we introduce the mathematical identities that will allow us to integrate the differential operators in equation (5.2.3) by parts.

The first identity it permits to write the differential $\nabla \times$ operator in its integral equivalent. If we consider an integration domain Ω, and the vectorial functions $\mathbf{a}(\mathbf{r})$, $\mathbf{F}(\mathbf{r})$, and $\mathbf{C}(\mathbf{r})$ are integrable on Ω, the identity reads:

$$\int_\Omega \mathbf{a} \cdot \nabla \times \mathbf{F} \; d^3r = \int_\Omega \mathbf{F} \cdot \nabla \times \mathbf{a} \; d^3r + \int_{\partial\Omega} \hat{n} \times \mathbf{F} \cdot \mathbf{a} \; d^2r.$$

The second identity permits to transform the $\nabla\nabla\cdot$ operator in its integral equivalent:

$$\int_\Omega \mathbf{a} \cdot \nabla\nabla \cdot \mathbf{C} \; d^3r = -\int_\Omega \nabla \cdot \mathbf{C} \; \nabla \cdot \mathbf{a} \; d^3r + \int_{\partial\Omega} \nabla \cdot \mathbf{C} \; \mathbf{a} \cdot \hat{n} \; d^2r,$$

where $\hat{n}$ is the outward normal vector on $\partial\Omega$.

If we specify $\mathbf{C} = \mathbf{E}$, $\mathbf{F} = \nabla \times \mathbf{E}$, and $\mathbf{a} = \tilde{\mathbf{E}}$, where $\tilde{\mathbf{E}}$ is the test function applied to $\mathbf{E}$ (see sec. 3.1), we obtain:

$$\int_\Omega \nabla \times \mathbf{E} \cdot \nabla \times \tilde{\mathbf{E}} \; d^3r - \epsilon_{\text{Drude}} k_0^2 \int_\Omega \mathbf{E} \cdot \tilde{\mathbf{E}} \; d^3r +$$

$$+ \int_{\partial\Omega} \tilde{\mathbf{E}} \cdot (\hat{n} \times \nabla \times \mathbf{E}) \; d^2r = -k_0^2 \vartheta_{\text{hd}} \int_\Omega \nabla \cdot \mathbf{E} \; \nabla \cdot \tilde{\mathbf{E}} \; d^3r +$$

$$+ k_0^2 \vartheta_{\text{hd}} \int_{\partial\Omega} \nabla \cdot \mathbf{E} \; \tilde{\mathbf{E}} \cdot \hat{n} \; d^2r,$$

$$(5.2.4)$$

and this is the *hydrodynamic wave equation* in the weak form. The term on the left-hand side represents the ordinary Maxwell's wave equation, while the term on the right-hand side represents the non-local contribution. This equation is very easy to implement in a finite-element method program, such as COMSOL.

5.3 Plasmonic waveguides: mathematical formulation

The equations (5.2.3) and (5.2.4) are general formulations that can be used for any kind of electromagnetic problem involving nonlocal response. We are interested into plasmon propagation into metallic waveguides, that are indefinitely extended along the guiding direction (say z), and they have a constant section that is invariant along z. The metallic waveguide is immersed into a dielectric medium with permittivity ϵ_r, that we can consider as infinitely extended in all directions (see fig. 5.1).

In waveguiding problems, we look for solutions of Maxwell's equations that are propagative along the guiding direction, and are confined in the near vicinity of the guiding structure. Thus, we must specialize the form of the electric field, and seek for solutions of this form:

$$\mathbf{E}(x, y, z) = \mathbf{E}(x, y)e^{ik_z z}, \qquad (5.3.1)$$

where (x, y) are the coordinate of the transversal section, k_z is the
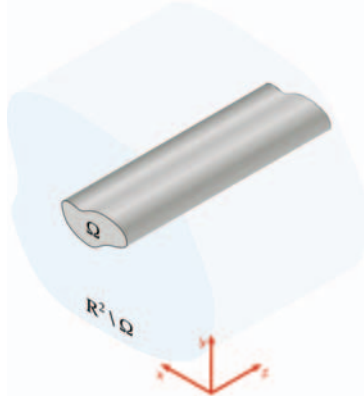
Figure 5.1 Metallic waveguide. The picture shows a generic waveguide. Ω is the metallic domain, that it is surrounded by a dielectric of permittivity ϵ_r. The guide is indefinitely extended along z.

propagation constant, that can be written as $k_z = \beta + i\alpha$, β is the propagation constant, and α is the attenuation constant. This is a wave that has a "shape" $\mathbf{E}(x, y)$ in the transversal direction, that propagates along z with propagation constant β, and the intensity $|\mathbf{E}(x, y)|$ is attenuated of $1/\alpha$ in the propagation direction. The dynamics of the solutions in the z direction is determined, so we have to find the field $\mathbf{E}(x, y)$ in the transversal direction.

The field (5.3.1) must obey to the hydrodynamic wave equation (5.2.3) in the transversal metallic domain Ω, and the ordinary wave equation for a local medium in the transversal dielectric $\mathbb{R}^2 \setminus \Omega$. This equation reads:

$$\int_{\mathbb{R}^2 \setminus \Omega} \left[\nabla \times \mathbf{E} \cdot \nabla \times \tilde{\mathbf{E}} - \epsilon_r k_0^2 \mathbf{E} \cdot \tilde{\mathbf{E}} \right] d^3r +$$

$$- \int_{\partial \Omega} \tilde{\mathbf{E}} \cdot (\hat{n} \times \nabla \times \mathbf{E}) \, d^2r = 0,$$

where the sign of the flux integral is negative due to the convention on the versor normal to $\partial \Omega$.

The test-function $\tilde{\mathbf{E}}$ must have the same form of (5.3.1), so it will be of the kind:

$$\tilde{\mathbf{E}}(x, y, z) = \tilde{\mathbf{E}}(x, y) e^{-i k_z z}.$$

The solution in the metallic domain Ω, and in the in the dielectric $\mathbb{R}^2 \setminus \Omega$ must be "glued" along the boundary $\partial \Omega$, and the z direction. This procedure leads to an eigenvalue problem for the electric field, with eigenvalue k_z.

The general procedure that we have illustrated here constitutes the the algorithm that we implemented in COMSOL 4.1, by using only the *PDE Weak form* module, and the standard MUMPS eigenvalue solver.

5.3.1 Implementation issues and workarounds

The numerical implementation that we discussed above allows us to determine the eigenvalue k_z of a given plasmonic waveguide configuration. However, the convergence of the electromagnetic field on the boundary of the structures is not pointwise. This is due to the fact that COMSOL does not give enough flexibility to the programmer concerning the boundary conditions and the interpolating polynomials.

An implementation based on the scheme discussed in Chapter 3, that is the solution of the coupled equations (2.2.8), would be possible in principle, but it does not converge in practice. The explanation for such behavior is not clear, but we think that it is due to two reasons: the fact that the solver has to handle a six dimensional vector as discussed in section 5.2, and the fact that $|\mathbf{J}|$

has higher value with respect, for example, the polarization vector $|\mathbf{P}|$.

Indeed, a way to overcome the latter problem is to write the equation of motion in terms of the polarization vector $\mathbf{P}$, that is linked to $\mathbf{J}$ by the equation:

$$\mathbf{P} = i\frac{\mathbf{J}}{\omega},$$

so $|\mathbf{P}|$ is smaller than $|\mathbf{J}|$ by a factor $1/\omega$. The system of equation in strong for in this case reads:

$$\nabla \times \nabla \times \mathbf{E} - k_0^2\mathbf{E} = \omega^2\mu_0\mathbf{P} \tag{5.3.2}$$

$$\beta^2\nabla\nabla \cdot \mathbf{P} + i(\omega + i\gamma)\mathbf{P} = -\epsilon_0\omega_p^2\mathbf{E}. \tag{5.3.3}$$

The equation (5.3.2) is solved by means of the *Mode Analysis* routine of the "EM module", and the equation of motion for $\mathbf{P}$ (5.3.3) is solved by means of the "PDE weak form" module. This implementation works correctly, and the convergence on the boundaries is punctual, and it is useful to determine the field shapes in proximity of the boundaries.

We call HDW code the implemetation based on the hydrodynamic wave equation, and HDP code to indicate the code based on the approach that we have just presented.

The propagation properties in section (5.4) are calculated with the HDW code, while the mode confinement properties calculated in sec. (5.5) are calculate by means of the HDP code.

5.4 Propagation properties of nanowires, V-grooves, and Λ-wedges

In this section we examine the dispersion relations for plasmonic waveguides that are characterized by an extreme light confinement: cylindrical nanowires, V-grooves and Λ-wedges (see fig. 5.2). All the waveguides we study are made of silver, and the interband effects are not included. The parameters for the free-electron gas are obtained from [74]. The analysis for the V-grooves and Λ-wedges is conducted in visible and near infrared band.

The case of the cylindrical nanowire is one of the first examples presented in the literature because it is possible to find analytical

solutions for the fields in the HD model for this kind of structures
[95].

Analytical solutions for the V-grooves in the HD model are difficult to obtain. Nonetheless, it is possible to calculate approximated solutions by using the effective-index method (EIM) in the LRA [96, 97]. The EIM method might be also applied to the HD model, but there are no works concerning this approach in the literature.

Finally, as far as we know, there are no analytical solutions for either the HD model or the LRA for the Λ-wedge.
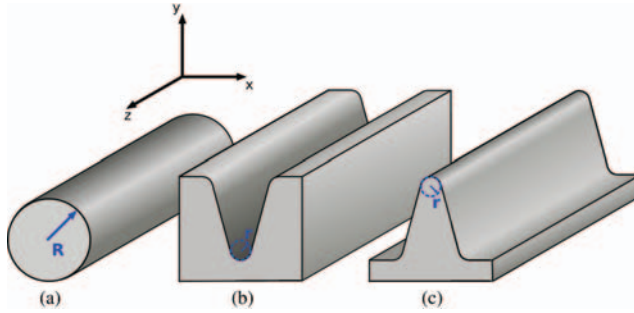
Figure 5.2 Generic plasmonic waveguides geometries with wave propagation in the z-direction and extreme transverse confinement in the xy-plane due to subnanometer geometric dimensions. a) Cylindrical nanowire b) V-groove c) Wedge.

It is difficult to find an analytical solution also for this kind of structures both for LRA and HD model.

The analysis that we performed is also a "limit-procedure" as described in chapter 4. In particular, we investigated the "fundamental limit" for the dispersion relation for both the V-groove and the wedge in the limiting case of curvature radius $r \to 0$ (r shown in fig. 5.2). A limit-procedure analysis was also performed for the cylindrical nanowire, in order to study the behavior for small radii.

5.4.1 Circular Nanowires

Fig. 5.3 shows the dispersion relation $\omega(k_z)$ for the fundamental mode of a cylindrical nanowire of radius $R = 2\,\mathrm{nm}$ (blue) and $R = 4\,\mathrm{nm}$ (green) in air. The solid points refer to the numerical results, while the solid lines represent the analytical results calculated by Ruppin [98]. The non-retarded analytical result for the LRA case
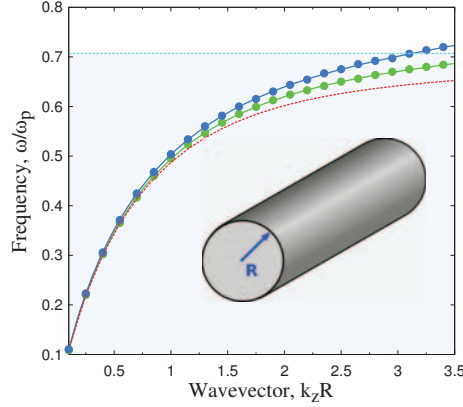
Figure 5.3 Dispersion relation $\omega(k_z)$ for the nanowire radius $R = 2\,\text{nm}$ (blue) and $R = 4\,\text{nm}$ (green) respectively. Numerical solutions are indicated with solid points, and analytical results are indicated with solid lines. The red dashed curve shows the universal result of the non-retarded LRA. with its large k_z limiting value $\omega_p/\sqrt{2}$ indicated by the horizontal light-blue line.

[99] is indicated by the red-dashed curve, and its large k_z limiting value $\omega_p/\sqrt{2}$ is indicated by the horizontal light-blue line. The effect of the nonlocal response is clearly visible. The local curve has an asymptotic behavior for large k_z, while the nonlocal curve shows a monotonically increasing behavior that depends on the radius R. The smaller the radius, the bigger is the slope of the line. This is again the *blueshift* effect: if we fix the value of k_z, the highest value of ω corresponds to the smallest radius R. This means that the nonlocal effects are non-negligible for very small isolated structures, as we discussed in 3. We did not calculate the dispersion relation for high-order mode. The analytical calculations were performed by Boardman and can be found in [95].

5.4.2   V-groove and Λ-wedge waveguides

The propagation in this kind of metallic waveguide is studied in terms of the effective refractive index and propagation length. These parameters are linked to the propagation constant β and the attenuation constant α by the definitions:

$$n_{\text{eff}} = \frac{\beta}{k_0} \qquad\qquad L = \frac{1}{2\alpha}.$$

The V-groove waveguide that we considered has an opening angle
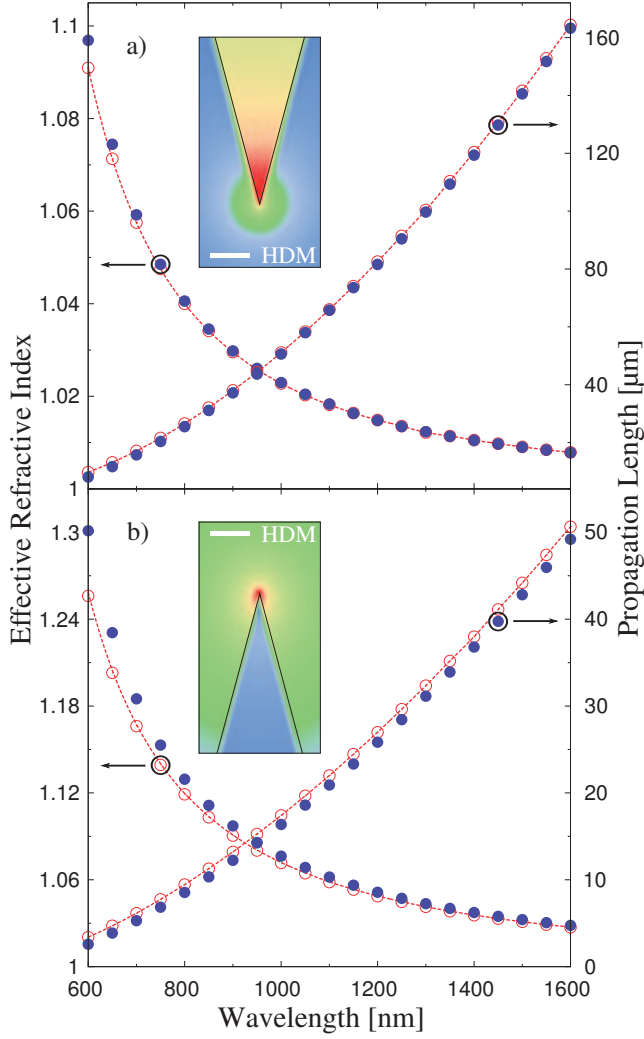
Figure 5.4 n_{eff} (left axis) and L (right axis) versus λ for the fundamental mode in complimentary (a) V-groove and (b) wedge silver waveguides, both with opening angle of $30°$. The nonlocal results (solid circles) are contrasted to the LRA (open circles). The dashed lines are eye guides. Results for structures with $r = 0$ (blue solid circles) are contrasted to rounding $r = 1\,\text{nm}$ (red open circles). Insets show field-intensity distributions (scale bars are $1\,\text{nm}$ long) calculated with the HDM ($\lambda = 600\,\text{nm}$) for $r = 0$.

of $\theta = 30°$. We studied the fundamental mode that is localized in the gap. It must be noticed that the depth of the groove must be chosen appropriately in order to ensure the mode localization [96, 97].

Fig 5.4a shows the dispersion relation $n_{\text{eff}}(\lambda)$ on the left axis, and the propagation length $L(\lambda)$ on the right axis. It can be noticed that the differences between local and nonlocal cases are negligible for both quantities n_{eff} and L when the radius of curvature $r = 1\,\text{nm}$. However, in the limiting case of $r = 0$, there are variations with respect to the case of $r > 0$.

Analogous discussion can be done for the sharp metal Λ-wedge (see fig. 5.4b). This wedge has an aperture angle of $\theta = 30°$, and it is the complimentary structure of the groove. There are no appreciable differences between the local and nonlocal case for $r = 1\,\text{nm}$ for both n_{eff} and L. The effective refractive index is larger for the nonlocal case when $r = 0$ at short wavelengths, while the propagation length is smaller in the same wavelength band.

5.5   Measure of confinement: mode area

As we said earlier, the plasmonic waveguides that we considered here are characterized by a high field confinement far beyond the diffraction limit.

An intuitive way to measure the efficiency of the mode confinement of a waveguide is by defining an effective area. There are many kinds of definition for mode areas in the literature, but the one we are interested here is [100]:

$$A_{\text{eff}} = \frac{\int_{V_m + V_a} \mathrm{d}x\mathrm{d}y\, u(\mathbf{r})}{\max_{V_a}\left\{u(\mathbf{r})\right\}}, \qquad (5.5.1)$$

where $u(\mathbf{r})$ is the electromagnetic energy functional, and the cross-sectional integral extends over the volumes V_m and V_a occupied by metal and air, respectively, while the evaluation of the maximal energy density is restricted to the air region. The electromagnetic energy functional $u(\mathbf{r})$ for the electron gas in the HD model is given by equation (2.3.6) in time domain. However, here we will consider the electric part of the functional, that for time-harmonic field is:

$$u_{\text{E}}^{\text{HD}} = \frac{1}{4}\varepsilon_0 \mathbf{E}^2 + \frac{\beta^2}{4\varepsilon_0 \omega_p^2}\rho^2 + \frac{1}{4\varepsilon_0 \omega_p^2}\mathbf{J}^2.$$

The analogue of this expression for the free-electron gas in the LRA

is [101]:

$$u_{\mathrm{E}}^{\mathrm{LRA}} = \frac{1}{4}\epsilon_0 \mathbf{E}^2 + \frac{1}{4}\epsilon_0 \left(\frac{\omega_p^2}{\omega^2 + \gamma^2} \right)\mathbf{E}^2,$$

while the energy density in air is simply $u_{\mathrm{E}}^{\mathrm{AIR}} = \frac{1}{4}\epsilon_0 \mathbf{E}^2$.

This definition of mode area is linked to the *Purcell factor*, that characterizes a mode ability to enhance the spontaneous emission rate of light of a near-by quantum system (atom, molecule, quantum dot). The rate of spontaneous emission by a quantum system, depends on the nature of the light source, and on the electromagnetic environment of the source itself. In the 1940s, Purcell discovered that the emission rate could be enhanced by placing a source close to a dielectric microcavity that is resonating with the radiative transition frequencies of the quantum system [102]. The emission rate for a dipole emission is proportional to the *Purcell factor*, that is defined by:

$$F_P = \frac{3Q}{4\pi^2 V_{\mathrm{eff}}} \left(\frac{\lambda}{n} \right)^3,$$

where V_{eff} is the mode volume for a cavity, that corresponds to the definition (5.5.1) extended to a 3D structure. The Purcell factor is a "coupling factor" between the emitter and the photonic structure, and it can be defined analogously for the coupling to a plasmonic waveguide [103]. In this case, the factor reads:

$$F_P \simeq \frac{1}{\pi} \frac{n_g}{n^2} \frac{A_0}{A_{\mathrm{eff}}},$$

where $A_0 = (\lambda/2)^2$, n_g is the group index of the waveguide mode, n is the refractive index of the medium surrounding the emitter, that is air in our case. The details of the derivation can be found in [100]. It is evident that a small mode area strongly enhances the coupling, and this makes the plasmonic waveguides that we examined good candidates for quantum communication applications [104].

We can now analyze the effect of nonlocal response on the mode area for our structures.

5.5.1 Cylindrical Nanowires

The case of the cylindrical nanowire is depicted in fig. 5.5, that shows the effective mode area for the fundamental mode A_{eff} normalized to R^2 as a function of the normalized propagation constant

$k_z R$. As in the case of the propagation properties β and α, the nonlocal effects are visible for values of the radius R smaller than $10\,\mathrm{nm}$. This confirms once again that the nonlocal effects in isolated systems become important for very small systems. Panel (b) shows
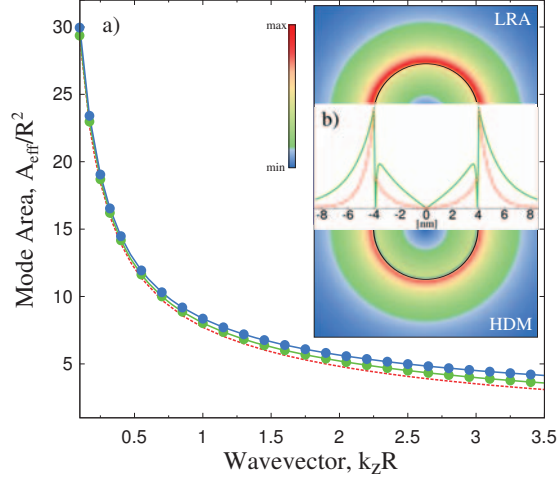
Figure 5.5 Panel (a) Normalized effective mode area within the HDM for the nanowire radius $R = 2\,\mathrm{nm}$ (blue) and $4\,\mathrm{nm}$ (green), respectively, showing excellent agreement between numerical solutions (solid points) and analytical results (solid lines). For comparison, the red-dashed curve shows the universal result of the nonretarded LRA. Panel (b) Radial distribution of the electric field $\left|\mathbf{E}_\rho\right|$ at $\omega = 0.6\,\omega_\mathrm{p}$ for $R = 4\,\mathrm{nm}$, contrasting the continuous field variation in the HDM with its usual boundary discontinuity in the LRA.

the distribution of the radial component of the electric field $\left|\mathbf{E}_\rho\right|$ for both the local and nonlocal case at a high frequency, $\omega = 0.6\,\omega_\mathrm{p}$ and for a wire with $R = 4\,\mathrm{nm}$. In the nonlocal case, the mode pattern in the metallic structure is affected by the excitation of the longitudinal field, and this is clearly visible in the cross-section plot. Moreover, $\left|\mathbf{E}_\rho\right|$ is continuous across the boundaries in the nonlocal case, while it shows a jump in the local case, as discussed in sec. 2.2.2.

5.5.2 V-groove and Λ-wedge waveguides

Fig 5.6 shows the effective mode area A_eff for the fundamental mode for both the V-groove (Panel a) and Λ-wedge (Panel b) structure. The area A_eff is normalized by the area A_0, and this provides a direct comparison of the mode area with the wavelength, showing the

subwavelength dimensions of the modes. It is possible to compare the relative size of the areas for both the wedge and the groove, and see that the wedge confines the light much better, as reported in [105].

We conducted a "limit-procedure" for the mode area as we did in par. 5.4.2 to determine how the mode area behaves when the curvature of the sharp tips $r \rightarrow 0$ both for the groove and the wedge. What we found is that the mode area in the LRA approximation decreases indefinitely as $r \rightarrow 0$, while it saturates in the HD model. This has an important impact on the spontaneous emission applications because it gives an upper limit on the Purcell factor.

The mode area for the wedge varies pretty slowly for long wavelengths, and it drops only for very short wavelengths. The mode area for the the V-groove varies quite abruptly instead. Moreover, A_{eff} for the Λ-wedge is almost 4 order of magnitude smaller that the relative value for V-groove in the telecommunications band $[1300 - 1600]\,$nm. A high field confinement capability and a considerably long propagation length make Λ-wedges very amenable for optical nanocircuits in the near infrared band. In the optical region of the spectrum, the effective areas for the two waveguides are comparable, but the propagation length for the V-groove is larger then the one for the Λ-wedge. Thus, V-grooves are superior to the Λ-wedges in the optical domain. This confirms the properties of these waveguides that we anticipated in sec. 5.1.

5.6 Convergence tests

In this section we consider the convergence tests for the waveguides that we have analyzed in the sections above. It is possible to observe in fig. 5.3 and fig. 5.5 that the agreement between the analytical and numerical solutions is very good. More quantitatively, the relative error of the numerically calculated propagation constant β with respect to the analytical value is always smaller than 0.3% in the entire frequency range of figure 5.3. The relative error for the effective mode area A_{eff} is always smaller than 0.12% on the same frequency range.

The convergence analysis for the circular nanowire waveguides
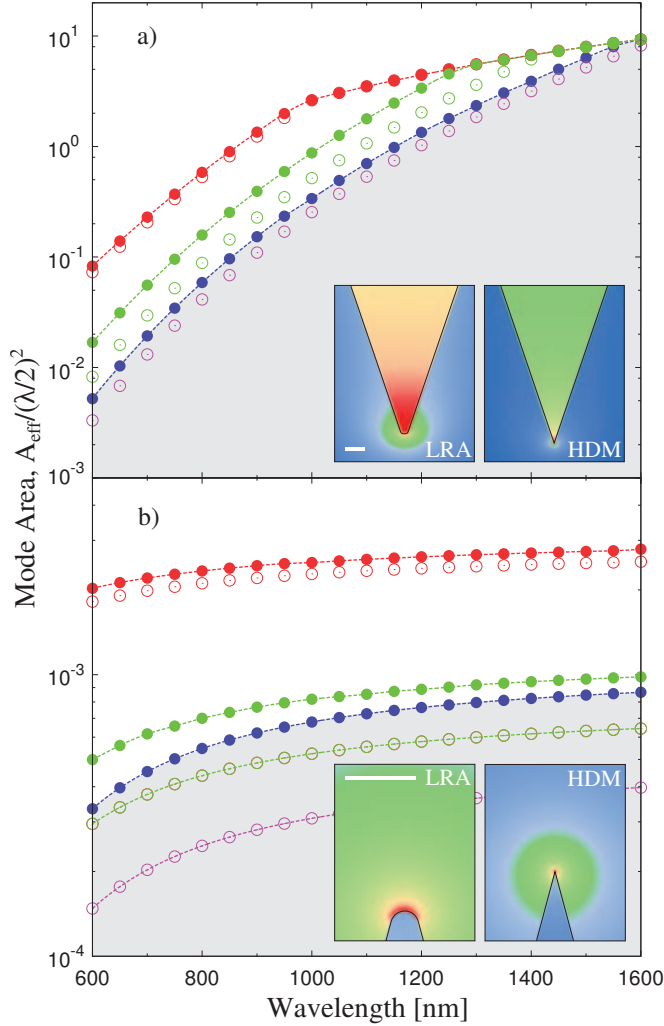
Figure 5.6 Normalized mode area versus wavelength for the fundamental mode in complimentary (a) V-groove and (b) wedge silver waveguides, both with opening angles of $30°$. The HDM results (solid symbols) are contrasted to the LRA (open circles), for $r = 1$ nm (red) and $r = 0.2$ nm (green). Results for mathematically sharp structures with $r = 0$ (blue solid circles) define a lower limit in the HDM (grey-shaded regions are inaccessible). For the LRA, the $r = 0.1$ nm results (magenta) exceed this limit and the mode area tends to zero when $r \to 0$. Insets show field-intensity distributions (white scale bars are 5 nm long) at $\lambda = 600$ nm. The LRA intensities are with rounding $r = 1$ nm, while $r = 0$ is used for the HDM maps.

is based on the methodology that we developed in sec. 3.4 for the scattering problem. In this case we have two observables, that

are the propagation constant β and the effective mode area A_{eff}. Thus, we define the relative errors $\delta_\beta^{\text{num}}$ and $\delta_{\text{A}}^{\text{num}}$ according to the definition given in eq. (3.4.3). We select the test that is performed at high frequency $\omega = 0.6\omega_p$, because in this case the field is mainly localized in the metal. This is a "worst-case" condition for the calculations because a high number of edge elements is needed. The results are shown in fig. 5.7. It is important to underline that the propagation constant β is calculated by means of the HDW code, while the mode area is calculated with the HDP code. However, both codes show a convergence of the calculated parameters for $n > 250$. The corresponding simulation time is about $5\,\text{min}$ for both codes.
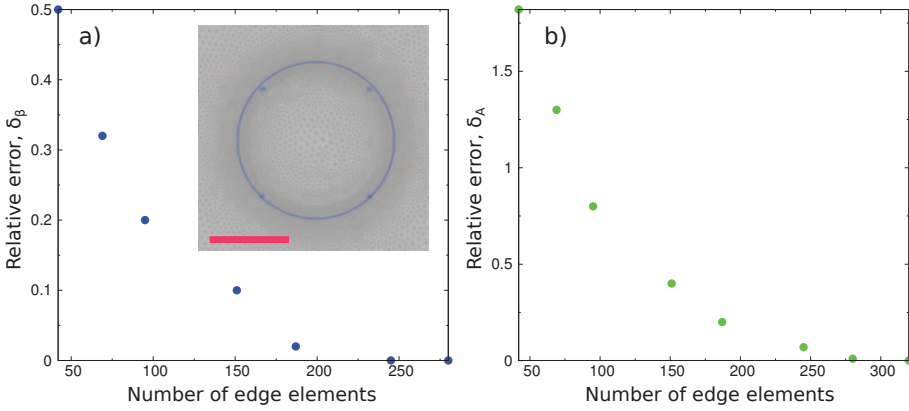
Figure 5.7 Convergence test for a cylindrical nanowire with radius $R = 2$ nm. Panel (a) Relative error $\delta_\beta^{\text{num}}$ of the propagation constant β versus number of edge elements for cylindrical nanowires. The convergence occurs for $n > 200$. Panel (b) Relative error $\delta_{\text{A}}^{\text{num}}$ of the effective mode area A_{eff} versus number of edge elements for cylindrical nanowires. The convergence occurs for $n > 250$. The scale bar is $1\,\text{nm}$ long. The inset refers to $n = 250$.

The convergence test for the V-groove is similar to the one we developed for the groove structure for SERS applications in par. 4.3.1. We consider the case $\lambda = 600\,\text{nm}$, because it corresponds to the maximum field localization in the visible spectrum, and a high mesh density is needed. The observables are the effective refractive index n_{eff}, and the propagation length L. Both relative errors $\delta_{\text{n}}^{\text{num}}$ and $\delta_{\text{L}}^{\text{num}}$ converge for $\overline{n} > 200$, and the simulation time is about 10 min. These results were calculated with the HDW code.
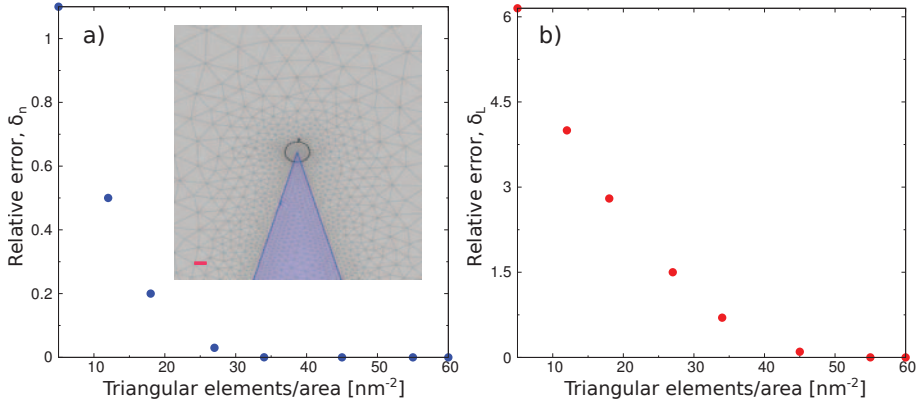
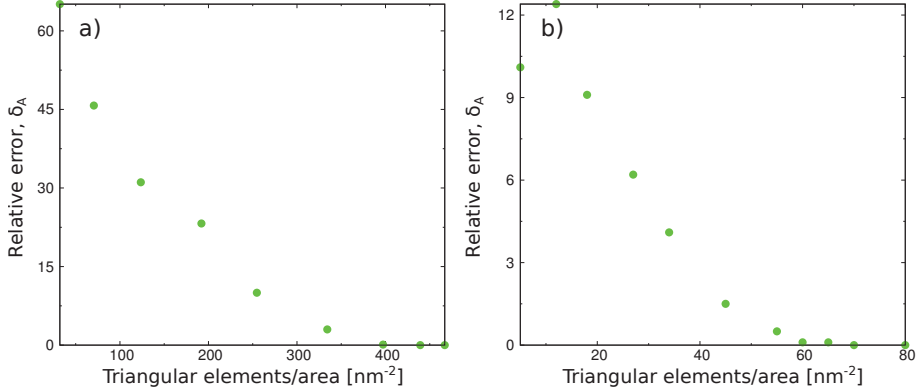The convergence test for the Λ-wedge structure is similar to
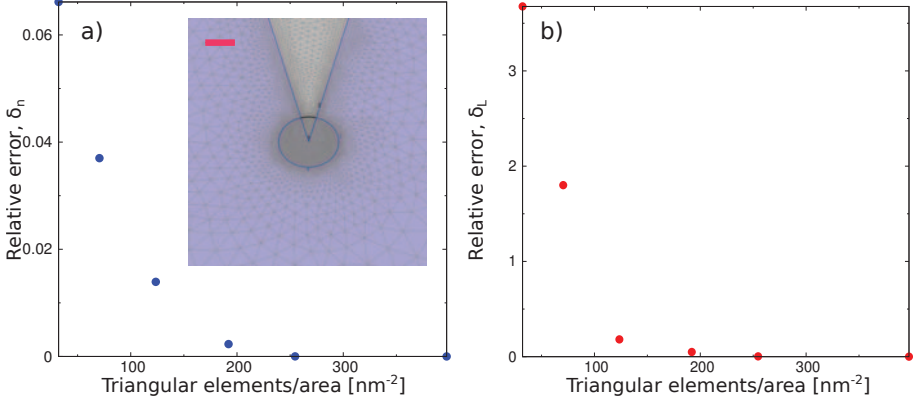
Figure 5.8 Convergence test for a V-groove structure with aperture angle $\theta = 30°$. The radius of the meshing circle $R_{\mathrm{mesh}} = 10\,\mathrm{nm}$, and it is kept constant while varying the number of triangular elements. Panel (a) Relative error $\delta_{\mathrm{n}}^{\mathrm{num}}$ of the effective refractive index versus the normalized number of triangular elements n. The convergence occurs for $\overline{n} > 200$, that corresponds to $\overline{n} = 6283$ elements. Panel (b) Relative error $\delta_{\mathrm{L}}^{\mathrm{num}}$ of the propagation length L versus $\overline{n}$. The convergence occurs for $\overline{n} > 200$. The scale bar is $10\,\mathrm{nm}$ long. The inset refers to $\overline{n} = 200$, and the shaded blue area indicates the metal.

the analysis performed for the triangular nanowire at par. 4.1.1. Also in this case, we show the test performed at $\lambda = 600\,\mathrm{nm}$, that corresponds to the highest field confinement in the metal. The results are shown in fig. 5.9, and it is possible to notice that the propagation length converges at higher n with respect to the effective refractive index. The Λ-wedge presents high losses at this wavelength, and the simulations can be very sensitive on the mesh density. The results are obtained with the HDW code, and the typical computation time is about $10\,\mathrm{min}$.

Finally, we consider the convergence of the effective mode area for both V-groove and Λ-wedge. The results are shown in fig. 5.9. It must be pointed out that the mesh densities in the two cases are relative to different geometrical entities, so they cannot be compared directly. This can be seen in the insets of fig. 5.9 and 5.8. The results are obtained with the HDP code, and the simulation time is about $10\,\mathrm{min}$ also in this case.

Figure 5.9 Convergence test for a Λ-wedge structure with aperture angle $\theta = 30°$. The radius of the meshing circle $R_{\mathrm{mesh}} = 1\,\mathrm{nm}$, and it varies, while the number of triangular elements is kept constant. Panel (a) Relative error $\delta_{\mathrm{n}}^{\mathrm{num}}$ of the effective refractive index versus the normalized number of triangular elements n. The convergence occurs for $\overline{n} > 30$, that corresponds to $n > 94$ elements. Panel (b) Relative error $\delta_{\mathrm{L}}^{\mathrm{num}}$ of the propagation length L versus $\overline{n}$. The convergence occurs for $\overline{n} > 45$, i.e. $n > 141$. The scale bar is $1\,\mathrm{nm}$ long. The inset refers to $\overline{n} = 141$, and the shaded blue area indicates the metal.

Figure 5.10 Convergence test for the effective mode area for V-groove and Λ-wedge waveguides. Panel (a) Relative error $\delta_{\mathrm{A}}^{\mathrm{num}}$ of the effective mode area A_{eff} versus number of edge element for the V-groove. The convergence occurs for $\overline{n} > 400$, i.e. $n > 12566$. Panel (b) Relative error $\delta_{\mathrm{A}}^{\mathrm{num}}$ of the effective mode area A_{eff} versus number of edge elements for the Λ-wedge waveguide. The convergence occurs for $\overline{n} > 60$, i.e. $n > 188$.

6

Conclusions and outlook

In this thesis I presented a theoretical study and a numerical implementation of the hydrodynamic model, and focused on its ability to describe fundamental phenomena that can not be accounted for in the Drude model.

In Chapter 2 I discussed the derivation of the hydrodynamic equations, that were used in my implementation. The key information is contained in Section 2.2, where I analyze both differences and similarities between local and nonlocal models from a theoretical point of view. The main point is the presence and importance of the pressure term, and the correct form of the boundary conditions. In particular, I showed that the surface charge layers have finite thicknesses in the nonlocal model, and this constitutes the novelty of the hydrodynamic approach to plasmonics.

In Chapter 3 I presented the numerical implementation in COMSOL Multiphysics of the hydrodynamic equation of motion (2.2.7), and derived its weak form. Then, I studied the scattering from a gold nanowire and a nanowire dimer. I observed that one of the main fingerprints of the hydrodynamic model is the blueshift of the surface plasmon resonance peaks, and this is due to the finite extension of the surface charge layers. The blueshift plays an important role in dimer structures, where two metallic particles face each other and Coulomb forces between them arise. For dimer structures, the electromagnetic energy is mainly confined in the gap, and this causes the phenomenon of field enhancement. The enhancement peaks are notably influenced by nonlocal effects,

and a decrease of the enhancement factor is usually but not always observed.

Another important feature of the hydrodynamic model is the ability to calculate fields near sharp tips where the classical model gives divergent results. This has important implications for the study of the structures where field enhancement is expected to saturate when the sharpness of the edges increases. This is actually the case of the groove structure for SERS applications that I presented in Chapter 4. I calculated the maximum field enhancement that is possible to achieve with this structure, and I noticed that it is smaller than the values typically measured experimentally.

Finally, in Chapter 5 I presented a new formulation of the hydrodynamic equation of motion, that has the same form of the usual wave equation in the local case. This implementation was fundamental for the definition and implementation of the waveguiding problem in COMSOL. The dispersion relations for the circular waveguide, V-groove and Λ-wedge were calculated. I also presented the ultimate surface mode area for V-groove and Λ-wedges, that has important implications for the understanding of the Purcell effect in spontaneous emission.

A natural direction for the future development of this work would be the study of the combined effects of spatial nonlocalities and electron tunneling for small gaps. A possible solution for this implementation has been devised by Dong *et al.* [39]. In this study, two circular nanorods were bridged by a fictitious medium that describes the conducting electrons in the gap region. Their results show that the tunneling effects dominate over the nonlocal effects in the conducting regime. However, the hydrodynamic model that they use is not correct, as I pointed out in [32]. The idea behind this particular implementation was initially presented by Esteban *et al.* [17], who used the Drude model for the metallic dimers.

From the experimental point of view, the effect of electron tunneling is still an open question because it is difficult to control the particles separation at a distance where these effects can be observed. However, the fabrication, control and analysis techniques

have improved in the last years, and new preliminary results were recently obtained. For example, Kern *et al.* [52] managed to control the gap between two gold nanorod dimer down to a width of 0.3 nm, with a combined HAADF-STM study. They showed that the tunneling starts to occur for gap widths that are ≤ 0.5 nm. They also made important measurement of resonance shifting and they observed a good qualitative agreement with my results for nanowire dimers. The control of the separation distance between two gold nanoparticle was also reached by Savage *et al.* [23], by means of a two gold-nanoparticle-terminated atomic force microscope (AFM), and they observed the onset of the tunneling effects at a separation distances of ~ 0.4 nm. Scholl *et al.* [106] also managed to control the distance between two nanosphere by means of a STEM-EELS combined approach. They show that the field enhancement in the quantum limit gap width of ~ 0.5 nm reaches a saturation, due to the tunneling current that neutralizes the charge separation at the junction between the spheres.

Another possible direction for my work could be the implementation of the nonlinear hydrodynamic model, I introduced in eq. (2.1.5). This model is highly complex from the computational point of view, but it would be possible to start from the analysis of the quadratic terms in the expansion (2.1.7). A similar approach has already been applied by Ciracì *et al.* [49, 50] in order to study the second-harmonic generation in metals.

There are other methods that are developing in parallel with the hydrodynamic model, and they are mainly based on ab-initio calculations. I recall here a pioneering work on plasmon resonance in a nanoparticle dimer as a function of the interparticle separation, that was conducted by Zuloaga *et al.* [26] in 2009. Some of the phenomena anticipated by these calculations, such as the plasmon resonance blueshift due to the conduction regime, were confirmed in the measurements made by Scholl *et al.* [106]. In my calculations for dimers [47], I showed that the nonlocal effects start already to be relevant for gap sizes of 3 nm, and it would be interesting to see ab-initio calculations confirming these results. The comparison of the effects observed in the hydrodynamic model with the outcomes of ab-initio calculations could be considered as another possible development of my work. In a recent work by Andersen *et al.* [107], an attempt was made to compare the classical Drude model with

a more advanced DFT-RPA combined approach for the study of plasmonic excitation in Na layers. The results showed a redshift of the surface plasmon resonance calculated with the ab-initio method respect to the classical one, and this is mainly due to the electrons spilling out of the Na layers.

The combination of ab-initio calculations and hydrodynamic model might be important for the description of 2D materials, such as graphene. The implementation of such a computational solution could be a new challenge to be taken up in the near future.

Paper A

Unusual resonances in nanoplasmonic structures due to nonlocal response

Søren Raza,[1] Giuseppe Toscano,[1] Antti-Pekka Jauho,[2] Martijn Wubs,[1,*] and N. Asger Mortensen[1,†]

[1]*Department of Photonics Engineering, Technical University of Denmark, DK-2800 Kgs. Lyngby, Denmark*
[2]*Department of Micro and Nanotechnology, Technical University of Denmark, DK-2800 Kgs. Lyngby, Denmark*

We study the nonlocal response of a confined electron gas within the hydrodynamical Drude model. We address the question as to whether plasmonic nanostructures exhibit nonlocal resonances that have no counterpart in the local-response Drude model. Avoiding the usual quasistatic approximation, we find that such resonances do indeed occur, but only above the plasma frequency. Thus the recently found nonlocal resonances at optical frequencies for very small structures, obtained within quasistatic approximation, are unphysical. As a specific example we consider nanosized metallic cylinders, for which extinction cross sections and field distributions can be calculated analytically.

Nanoplasmonics[1,2] is presently entering an era where the metallic structures offer nanoscale features that will eventually allow both photons and electrons to exhibit their full wave nature. This regime challenges the existing theoretical framework resting on a local-response picture using bulk-material parameters. In tiny metallic nanostructures, quantum confinement[3–7] and nonlocal response[8–18] are believed to change the collective plasmonic behavior with resulting strong optical fingerprints and far-reaching consequences for, e.g., field enhancement and extinction cross sections. Within nonlocal response, Maxwell's constitutive relation between the displacement and the electric fields reads

$$D(r,\omega) = \varepsilon_0 \int dr' \, \varepsilon(r,r',\omega) \cdot E(r',\omega). \quad (1)$$

The dielectric tensor $\varepsilon(r,r',\omega)$ reduces to $\varepsilon(r,\omega)\delta(r-r')$ in the local-response limit. Historically, there has been a strong emphasis on nonlocal response in extended systems with translational invariance (TI),[10] where a k-space representation is useful. However, for the present problem of metallic nanostructures, TI is broken and a real-space description is called for.

Recent theoretical studies of nanoscale plasmonic structures have predicted considerable differences in the field distributions and scattering cross sections between local and nonlocal response theories, both in numerical implementations of a simplified hydrodynamic Drude model,[14–18] and in corresponding analytical calculations.[15] Importantly, additional resonances of the free-electron plasma were found, also at optical frequencies, which have no counterparts in local-response theories. Such resonances have already gained interest both from a fundamental[7] and an applied[19] perspective. At present, the status of these optical nonlocal resonances is unclear, since in Ref. 13 the same nonlocal model was used as in Refs. 14–18, and yet no corresponding modes were found at visible frequencies. Resolving this issue is important for the engineering of ultrasmall plasmonic structures with optimized functionalities.[19–21]

In this Rapid Communication we report that unusual resonances due to nonlocal response do exist in nanoplasmonic structures, but only above the plasma frequency, not in the visible. We illustrate this property of arbitrary plasmonic

structures by exact calculations for metallic cylinders. We also clarify that different implementations of the common quasistatic approximation[9,11] are the reason for the conflicting results in Refs. 13–18. Here we refrain from making this approximation altogether, and by comparison analyze the validity and implementation of the quasistatic approximation in the hydrodynamic model.

The hydrodynamic Drude model. We express the collective motion of electrons in an inhomogeneous medium in terms of the electron density $n(r,t)$ and the hydrodynamical velocity $v(r,t)$.[8] Under the influence of macroscopic electromagnetic fields $E(r,t)$ and $B(r,t)$, the hydrodynamic model is defined via[10]

$$[\partial_t + v \cdot \nabla] v = -\gamma v - \frac{e}{m}[E + v \times B] - \frac{\beta^2}{n}\nabla n, \quad (2)$$

along with the continuity equation $\partial_t n = -\nabla \cdot (nv)$, expressing charge conservation. In the right-hand side of Eq. (2), the γ term represents damping, the second term is the Lorentz force, while the third term is due to the internal kinetic energy of the electron gas, here described within the Thomas-Fermi model, with β proportional to the Fermi velocity v_F. In analogy with hydrodynamics, the third term represents a pressure that gives rise to a nonlocal dielectric tensor, since energy may be transported by mechanisms other than electromagnetic waves.

We follow the usual approach[11] to solve Eq. (2) and the continuity equation, by expanding the physical fields in a zeroth-order static term, where, e.g., n_0 is the homogeneous static electron density, and a small (by assumption) first-order dynamic term, thereby linearizing the equations. In the frequency domain, we obtain

$$\beta^2 \nabla[\nabla \cdot J] + \omega(\omega + i\gamma)J = i\omega \omega_p^2 \varepsilon_0 E \quad (3a)$$

for a homogeneous medium, where $J(r) = -en_0 v(r)$ is the current density, and ω_p is the plasma frequency which also enters the Drude local-response function $\varepsilon(\omega) = 1 - \omega_p^2/[\omega(\omega + i\gamma)]$. We focus on the plasma, leaving out bulk interband effects present in real metals that could be easily taken into account,[14,22] as well as band-bending effects at the metal surface.

The electromagnetic wave equation. The retarded linearized hydrodynamic model is then fully described by Eq. (3a), together with the Maxwell wave equation

$$\nabla \times \nabla \times \boldsymbol{E} = \frac{\omega^2}{c^2}\boldsymbol{E} + i\omega\mu_0\boldsymbol{J}. \qquad (3b)$$

In order to see that these coupled equations (3) indeed describe a nonlocal dielectric response, one can in Eq. (3b) rewrite the current density $\boldsymbol{J}$ as an integral over the Green's tensor of Eq. (3a) and the electric field, whereby the nonlocal dielectric tensor of Eq. (1) can be identified.

In a local-response description it is commonplace to introduce the quasistatic or curl-free assumption that $\nabla \times \boldsymbol{E} = 0$.[23] This well-established approximation lies at the heart of most treatments and interpretations of electromagnetic wave interactions with subwavelength structures. Intuitively, one might expect that it can be extended to the nonlocal case and indeed several nonlocal treatments use this assumption.[9,11,13–17] However, as we shall demonstrate, one should proceed with care.

Three models. Here we solve Eqs. (3) directly, without further assumptions or approximations. We also compare the *nonlocal model* with two other models obtained by further assumptions. The *curl-free nonlocal model* enforces the condition $\nabla \times \boldsymbol{E} = 0$, which with Eq. (3a) implies that also $\nabla \times \boldsymbol{J} = 0$ in the medium. For the differential-operator term in Eq. (3a), from now on denoted $\hat{L}_J$, this has the consequence that $\nabla[\nabla \cdot]$ simplifies to the Laplace operator ∇^2, which gives the model used by Ruppin in the context of exciton physics in Ref. 27, and recently in plasmonics by McMahon *et al.*[14–17] and also by ourselves.[18] Finally, by assuming $\hat{L}_J = 0$ in the hydrodynamic treatment (3a), the familiar *local model* is obtained, with $\boldsymbol{J}$ and $\boldsymbol{E}$ related by Ohm's law.

We assume that the static density of electrons n_0 vanishes outside the metal of volume V, while it is constant and equal to the bulk value inside V, thus neglecting tunneling effects and inhomogeneous electron distributions associated with quantum confinement.[3,6] As a consequence, $\boldsymbol{J} = 0$ outside V for all three models.

Boundary conditions. In the local model the current $\boldsymbol{J}$ has the same the spatial dependence as the $\boldsymbol{E}$ field. Thus, in this case there are no additional boundary conditions (ABCs) to those already used in Maxwell's equations. For the nonlocal-response models, on the other hand, ABCs are in general needed.[10,16,24–26] From discussions in the literature it might appear that the number of necessary ABCs is a subtle issue, but we emphasize that there should be no ambiguity. The crucial point is that the required number of ABCs depends on the assumed static electron density profile at the boundaries.[26] For the present problem with the electron density vanishing identically outside the metal, only one ABC is needed in the nonlocal model to obtain unique solutions,[26] and it is readily found from the continuity equation and Gauss' theorem: $\hat{\boldsymbol{n}} \cdot \boldsymbol{J} = 0$ on the boundary, where $\hat{\boldsymbol{n}}$ is a normal vector to the surface, i.e., the normal-component of the current vanishes,[10,24,26] for all three models. On the other hand, in general, the tangential current $\hat{\boldsymbol{n}} \times \boldsymbol{J}$ is nonzero. This "slip" of the current is not surprising, since the hydrodynamic equation (2) describes the plasma as a nonviscous fluid.

TABLE I. Summary of the three different response models. V is the volume of the nanostructure, and ∂V its boundary.

	$\boldsymbol{r} \in V$		$\boldsymbol{r} \in \partial V$		$\boldsymbol{r} \notin V$
	$\nabla \times \boldsymbol{J}$	$\hat{L}_J$	$\hat{\boldsymbol{n}} \cdot \boldsymbol{J}$	$\hat{\boldsymbol{n}} \times \boldsymbol{J}$	$\boldsymbol{J}$
Local	$\neq 0$	0	0	$\neq 0$	0
Nonlocal	$\neq 0$	$\beta^2\nabla[\nabla\cdot]$	0	$\neq 0$	0
Nonlocal (curl-free)	0	$\beta^2\nabla^2$	0	0	0

Likewise, in several implementations of the quasistatic approximation, no further ABCs are needed to uniquely determine the electric field and current density.[11,13] In contrast, in the curl-free nonlocal model of Refs. 14–18 and 27, one more ABC *is* needed. It is assumed that the tangential components of $\boldsymbol{J}$ vanish at the boundary ($\hat{\boldsymbol{n}} \times \boldsymbol{J} = 0$), so that both normal and tangential components of the current field vanish on the boundary. In the different context of exciton physics[27] these are often referred to as Pekar's additional boundary conditions. There, the vanishing of the tangential boundary currents is motivated by the physical assumption that exciton wave functions vanish on the boundary.[27,28] Instead, in the hydrodynamical theory of metals, the ABC $\hat{\boldsymbol{n}} \times \boldsymbol{J} = 0$ seems more *ad hoc*: not a direct consequence of the quasi-static approximation, and not correct if that approximation is not made. The different boundary conditions are summarized in Table I.

Extinction cross section of metallic nanowires. To illustrate the surprisingly different physical consequences of the three models, we consider light scattering by a nanowire. Rather than solving Eqs. (3) numerically for a general cross-sectional geometry, we here limit our analysis to cylindrical wires whereby significant analytical progress is possible. We use an extended Mie theory, developed by Ruppin,[27,29] to calculate the extinction cross section σ_{ext} of an infinitely long spatially dispersive cylindrical metal nanowire in vacuum. Outside the wire there are incoming and scattered fields (both divergence free), whereas inside the wire both divergence-free and curl-free modes can be excited, the latter type only in the case of nonlocal response. The cross section is[30]

$$\sigma_{\text{ext}} = -\frac{2}{k_0 a}\sum_{n=-\infty}^{\infty}\text{Re}\{a_n\}, \qquad (4)$$

where a is the radius, $k_0 = \omega/c$ is the vacuum wave vector, and a_n is a cylindrical Bessel-function expansion coefficient for the scattered fields. We consider a normally incident plane wave with the electric-field polarization perpendicular to the cylinder axis (TM). The expression for the coefficients a_n depends on the particular response model and the associated ABCs. For the curl-free nonlocal model, the a_n are known.[27] For the full hydrodynamic model we follow the approach of Ref. 29, where the ABC of Ref. 25 is employed. This ABC is for metals in free space equivalent to $\hat{\boldsymbol{n}} \cdot \boldsymbol{J} = 0$. We obtain

$$a_n = -\frac{\left[d_n + J_n'(\kappa_t a)\right]J_n(k_0 a) - \sqrt{\varepsilon}J_n(\kappa_t a)J_n'(k_0 a)}{\left[d_n + J_n'(\kappa_t a)\right]H_n(k_0 a) - \sqrt{\varepsilon}J_n(\kappa_t a)H_n'(k_0 a)}, \qquad (5)$$
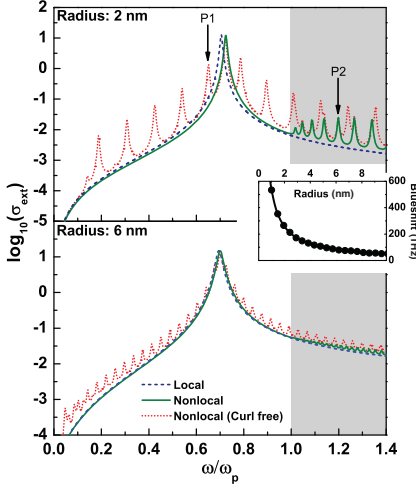
FIG. 1. (Color online) Extinction cross sections σ_{ext} as a function of frequency for TM-polarized light normally incident on a metallic cylinder in vacuum. Parameters for Au as in Ref. 14: $\hbar\omega_{\text{p}} = 8.812$ eV, $\hbar\gamma = 0.0752$ eV, and $v_{\text{F}} = 1.39 \times 10^6$ m/s. Inset: Frequency shift of the maximum $\sigma_{\text{ext}}(\omega)$ for nonlocal against local response, as a function of radius.
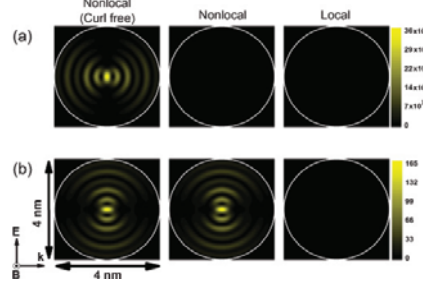

FIG. 2. (Color online) Field distributions in the three different models, for TM-polarized light normally incident on a cylinder of radius $a = 2$ nm. (a) Normalized displacement field $|\boldsymbol{D}|^2/|\boldsymbol{D}_{\text{in}}|^2$ at the frequency $\omega = 0.6503\omega_{\text{p}}$ (P1 in Fig. 1). $\boldsymbol{D}_{\text{in}} = \varepsilon_0\boldsymbol{E}_{\text{in}}$ and $\boldsymbol{E}_{\text{in}}$ is the incident electric field. (b) Analogous plots of $|\boldsymbol{E}|^2/|\boldsymbol{E}_{\text{in}}|^2$ for $\omega = 1.1963\omega_{\text{p}}$ (P2 in Fig. 1).

where J_n and H_n are Bessel and Hankel functions of the first kind and $\kappa_t^2 = \varepsilon(\omega)k_0^2$. The d_n coefficients are

$$d_n = \frac{n^2}{\kappa_l a} \frac{J_n(\kappa_l a)}{J_n'(\kappa_l a)} \frac{J_n(\kappa_t a)}{\kappa_t a} [\varepsilon(\omega) - 1], \tag{6}$$

where $\kappa_l^2 = (\omega^2 + i\omega\gamma - \omega_{\text{p}}^2)/\beta^2$. In the limit $\beta \to 0$, the d_n vanish and the a_n of Eq. (5) reduce to the local Drude scattering coefficients,[30] which confirms that the nonlocal response in our model requires moving charges.

Are there nonlocal resonances? Figure 1 depicts the extinction cross section of Eq. (4) for two cylinder radii, comparing the nonlocal models with the local Drude model. The main surface-plasmon resonance peak at $\omega_{\text{p}}/\sqrt{2}$ is blueshifted as compared to the local model, and more so for smaller radii. Similar blueshifts have been reported for other geometries[12] and in the curl-free nonlocal model.[14,27]

Figure 1 shows the unusual resonances mentioned in the title of this Rapid Communication: Additional peaks *do* appear in the nonlocal theory but only for frequencies *above* the plasma frequency ω_{p} ($\hbar\omega_{\text{p}} = 8.9$ eV for Ag and Au; 1.5–3 eV is visible). These peaks (such as P2 in Fig. 1) are due to the excitation of confined longitudinal modes, which are bulk-plasmon states with discrete energies above $\hbar\omega_{\text{p}}$ due to confinement in the cylinder.[13] These peaks are analogous to discrete absorption lines above the band gap in quantum-confined semiconductor structures. Interestingly, contrary to

the common belief that light does not scatter off bulk plasmons, which is correct in the local theory (i.e., no peak around ω_{p} in Fig. 1), here in the nonlocal model we do find such a coupling to longitudinal modes. The corresponding resonances could therefore be observed with electron loss spectroscopy but also with extreme UV light. The curl-free model also exhibits these resonances.

The striking difference between the two nonlocal-response models is that the curl-free nonlocal model shows additional stronger resonances, both above and below the plasma frequency, such as P1 in Fig. 1, in particular also at optical frequencies. These peaks do not show up in the full hydro-dynamical model, and thus originate from a mathematical approximation rather than a physical mechanism. It would, however, be premature to conclude that the quasistatic approximation breaks down, because in Ref. 13 the modes of cylinders in the hydrodynamical Drude model were found after making the quasistatic approximation, and the only different modes found were the confined bulk plasmon modes above ω_{p}. Figure 1 also illustrates that for increasing radii, σ_{ext} in the two nonlocal models converges toward the local-response value. This convergence is slower for the curl-free model.

In Fig. 2(a) we depict the scaled *displacement*-field distributions for the three models at the frequency marked P1 in Fig. 1, where only the curl-free nonlocal model has a (spurious) resonance. Correspondingly, in Fig. 2(a) we find a standing-wave pattern only in that model. Its appearance in the displacement field illustrates that the spurious resonance is a transverse resonance, i.e., occurring in the divergence-free components of $\boldsymbol{E}$ and $\boldsymbol{J}$. Figure 2(b), on the other hand, shows the normalized *electric*-field intensity for a true resonant mode at the frequency P2 of Fig. 1. Only the two nonlocal models give rise to resonant electric-field patterns. These confined bulk plasmon modes are longitudinal and would not produce standing waves in the displacement field.

Origin of spurious resonances. By eliminating the electric field from Eqs. (3), it follows that the exact hydrodynamic current satisfies the pair of third-order equations

$$(\beta^2\nabla^2 + \omega^2 + i\omega\gamma - \omega_p^2)\nabla \cdot \boldsymbol{J} = 0, \tag{7a}$$

$$[c^2\nabla^2 + \omega^2\varepsilon(\omega)]\nabla \times \boldsymbol{J} = 0, \tag{7b}$$

which reduce to the more symmetric Boardman equations[31] in the absence of damping. For arbitrary geometry, Eq. (7a) has damped solutions of $\nabla \cdot \boldsymbol{J}$ for $\omega < \omega_p$ and finite-width resonances for $\omega > \omega_p$, as seen in Fig. 1. Both solutions can be consistent with the quasistatic approximation $\nabla \times \boldsymbol{J} = 0$ that trivially solves Eq. (7b). On the other hand, we find that the spurious resonances have resonant divergence-free components of **E** and **J**. However, these cannot at the same time be curl free. Thus the curl-free nonlocal model has resonant solutions with nonvanishing curl, which is logically inconsistent. But how could this arise? Once the $\nabla \times \boldsymbol{J} = 0$ assumption has been invoked to simplify the differential operator into $\hat{L}_J = \beta^2\nabla^2$, the resulting Laplacian equation analogous to (3a) carries no information that the resulting solution should also be curl free. Thus, the solutions found for this equation are not necessarily self-consistent.

Conclusions. We have shown that plasmonic nanostructures exhibit unique resonances due to nonlocal response in the hydrodynamic Drude model, but only above the plasma frequency. The recently reported nonlocal resonances in the visible[14–18] agree with older work,[27] but are a surprisingly pronounced consequence of an implementation of the quasistatic approximation that is not self-consistent. For nanowires, we find extinction resonances without making the quasistatic approximation that agree with the quasistatic modes of Ref. 13, so we do not claim a general breakdown of the approximation itself. Even though there are no nonlocal resonances in the visible, plasmonic field enhancements are affected by nonlocal response. For arbitrary geometries, numerical methods must be used to quantitatively assess their importance. Self-consistent versions of the versatile time-domain[14–17] and frequency-domain[18] implementations of the hydrodynamical model can do just that.

*mwubs@fotonik.dtu.dk

†asger@mailaps.org

[1] D. K. Gramotnev and S. I. Bozhevolnyi, Nat. Photon. **4**, 83 (2010).

[2] J. A. Schuller, E. S. Barnard, W. Cai, Y. C. Jun, J. S. White, and M. L. Brongersma, Nat. Mater. **9**, 193 (2010).

[3] N. D. Lang and W. Kohn, Phys. Rev. B **1**, 4555 (1970).

[4] J. Zuloaga, E. Prodan, and P. Nordlander, Nano Lett. **9**, 887 (2009).

[5] O. Pérez-González, N. Zabala, A. G. Borisov, N. J. Halas, P. Nordlander, and J. Aizpurua, Nano Lett. **10**, 3090 (2010).

[6] Z. F. Öztürk, S. Xiao, M. Yan, M. Wubs, and N. A. Mortensen, J. Nanophoton. **5**, 051602 (2011).

[7] M. Wand, A. Schindlmayr, T. Meier, and J. Förstner, Phys. Status Solidi B **248**, 887 (2011).

[8] F. Bloch, Z. Phys. A **81**, 363 (1933).

[9] G. Barton, Rep. Prog. Phys. **42**, 963 (1979).

[10] A. D. Boardman, *Electromagnetic Surface Modes* (Wiley, New York, 1982).

[11] J. M. Pitarke, V. M. Silkin, E. V. Chulkov, and P. M. Echenique, Rep. Prog. Phys. **70**, 1 (2007).

[12] F. J. García de Abajo, J. Phys. Chem. C **112**, 17983 (2008).

[13] I. Villó-Pérez and N. R. Arista, Surf. Sci. **603**, 1 (2009).

[14] J. M. McMahon, S. K. Gray, and G. C. Schatz, Phys. Rev. Lett. **103**, 097403 (2009).

[15] J. M. McMahon, S. K. Gray, and G. C. Schatz, Phys. Rev. B **82**, 035423 (2010).

[16] J. M. McMahon, S. K. Gray, and G. C. Schatz, Nano Lett. **10**, 3473 (2010).

[17] J. M. McMahon, S. K. Gray, and G. C. Schatz, J. Phys. Chem. C **114**, 15903 (2010).

[18] G. Toscano, M. Wubs, S. Xiao, M. Yan, Z. F. Öztürk, A.-P. Jauho, and N. A. Mortensen, Proc. SPIE **7757**, 77571T (2010).

[19] R. Marty, A. Arbouet, C. Girard, J. Margueritat, J. Gonzalo, and C. N. Afonso, J. Chem. Phys. **131**, 224707 (2009).

[20] Y. Xia, Y. Xiong, B. Lim, and S. E. Skrabalak, Angew. Chem. Int. Ed. **48**, 60 (2009).

[21] S. Peng, J. M. McMahon, G. C. Schatz, S. K. Gray, and Y. Sun, Proc. Natl. Acad. Sci. USA **107**, 14530 (2010).

[22] S. A. Maier, *Plasmonics: Fundamentals and Applications* (Springer, New York, 2007).

[23] J. D. Jackson, *Classical Electrodynamics*, 3rd ed. (Wiley, Hoboken, NJ, 1999).

[24] F. Sauter, Z. Phys. **203**, 488 (1967).

[25] A. R. Melnyk and M. J. Harrison, Phys. Rev. B **2**, 835 (1970).

[26] P. Jewsbury, J. Phys. F **11**, 195 (1981).

[27] R. Ruppin, J. Opt. Soc. Am. B **6**, 1559 (1989).

[28] S. Pekar, J. Phys. Chem. Solids **5**, 11 (1958).

[29] R. Ruppin, Opt. Commun. **190**, 205 (2001).

[30] H. van de Hulst, *Light Scattering by Small Particles* (Wiley, New York, 1957).

[31] A. D. Boardman and B. V. Paranjape, J. Phys. F **7**, 1935 (1977).

Paper B

G. Toscano, S. Raza, A.-P. Jauho, N. A. Mortensen, and M. Wubs, "Modified field enhancement and extinction by plasmonic nanowire dimers due to nonlocal response",
Opt. Express **20**, 4176 (2012).

Modified field enhancement and extinction by plasmonic nanowire dimers due to nonlocal response

Giuseppe Toscano,[1] **Søren Raza,**[1,2] **Antti-Pekka Jauho,**[3]
N. Asger Mortensen,[1] **and Martijn Wubs**[1,*]

[1]*DTU Fotonik, Department of Photonics Engineering, Technical University of Denmark, DK-2800 Kongens Lyngby, Denmark*
[2]*DTU Cen, Center for Electron Nanoscopy, Technical University of Denmark, DK-2800 Kongens Lyngby, Denmark*
[3] *DTU Nanotech, Department of Micro- and Nanotechnology, Technical University of Denmark, DK-2800 Kongens Lyngby, Denmark*

[*]mwubs@fotonik.dtu.dk

Abstract: We study the effect of nonlocal optical response on the optical properties of metallic nanowires, by numerically implementing the hydrodynamical Drude model for arbitrary nanowire geometries. We first demonstrate the accuracy of our frequency-domain finite-element implementation by benchmarking it in a wide frequency range against analytical results for the extinction cross section of a cylindrical plasmonic nanowire. Our main results concern more complex geometries, namely cylindrical and bow-tie nanowire dimers that can strongly enhance optical fields. For both types of dimers we find that nonlocal response can strongly affect both the field enhancement in between the dimers and their respective extinction cross sections. In particular, we give examples of blueshifted maximal field enhancements near hybridized plasmonic dimer resonances that are still large but nearly two times smaller than in the usual local-response description. For the same geometry at a fixed frequency, the field enhancement and cross section can also be significantly more enhanced in the nonlocal-response model.

© 2012 Optical Society of America

References and links

1. A. D. Boardman, *Electromagnetic Surface Modes* (Wiley, 1982).
2. S. A. Maier, *Plasmonics: Fundamentals and Applications* (Springer, 2007).
3. D. K. Gramotnev and S. I. Bozhevolnyi, "Plasmonics beyond the diffraction limit," Nat. Photonics **4**, 83–91 (2010).
4. J. Aizpurua, G. W. Bryant, L. J. Richter, and F. J. García de Abajo, B. K. Kelley, and T. Mallouk, "Optical properties of coupled metallic nanorods for field enhanced spectroscopy," Phys. Rev. B **71**, 235420 (2005).
5. S. Xiao, N. A. Mortensen, and A.-P. Jauho, "Nanostructure design for surface-enhanced Raman spectroscopy - prospects and limits," J. Eur. Opt. Soc. Rap. Pub. **3**, 08022 (2008).
6. H. Wei, Z. Li, X. Tian, Z. Wang, F. Cong, N. Liu, S. Zhang, P. Nordlander, N. J. Halas, and H. Xu, "Quantum dot-based local field imaging reveals plasmon-based interferometric logic in silver nanowire networks," Nano Lett. **11**, 471–475 (2011).
7. Y. Chen, M. Wubs, J. Mørk, and A. F. Koenderink, "Coherent single-photon absorption by single emitters coupled to 1D nanophotonic waveguides," New J. Phys. **13**, 103010 (2011).

8. C. Rockstuhl, M. G. Salt, and H. P. Herzig, "Analyzing the scattering properties of coupled metallic nanoparticles," J. Opt. Soc. Am. A **21**, 1761–1768 (2004).

9. O. L. Muskens, V. Giannini, J. A. Sánchez-Gil, and J. Gómez Rivas, "Optical scattering resonances of single and coupled dimer plasmonic nanoantennas," Opt. Express **15**, 17736–17746 (2007).

10. V. Giannini and J. A. Sánchez-Gil, "Calculations of light scattering from isolated and interacting metallic nanowires of arbitrary cross section by means of Greens theorem surface integral equations in parametric form," J. Opt. Soc. Am. A **24**, 2822–2830 (2007).

11. T. Shegai, S. Chen, V. D. Miljković, G. Zengin, P. Johansson, and M. Käll, "A bimetallic nanoantenna for directional colour routing," Nat. Commun. 2:481 doi: 10.1038/ncomms1490 (2011).

12. R. Fuchs and K. L. Kliewer, "Optical properties of an electron gas: further studies of a nonlocal description," Phys. Rev. **185**, 905–913 (1969).

13. B. B. Dasgupta and R. Fuchs, "Polarizability of a small sphere including nonlocal effects," Phys. Rev. B **24**, 554–561 (1981).

14. F. J. García de Abajo, "Nonlocal effects in the plasmons of strongly interacting nanoparticles, dimers, and waveguides," J. Phys. Chem. C **112**, 17983–17987 (2008).

15. J. M. McMahon, S. K. Gray, and G. C. Schatz, "Nonlocal optical response of metal nanostructures with arbitrary shape," Phys. Rev. Lett. **103**, 097403 (2009).

16. S. Raza, G. Toscano, A.-P. Jauho, M. Wubs and N. A. Mortensen, "Unusual resonances in nanoplasmonic structures due to nonlocal response," Phys. Rev. B **84**, 121412(R) (2011).

17. C. David and F. J. García de Abajo, "Spatial nonlocality in the optical response of metal nanoparticles," J. Phys. Chem. C **115**, 19470–19475 (2011).

18. R. Ruppin, "Extinction properties of thin metallic nanowires," Opt. Commun. **190**, 205–209 (2001).

19. I. Villó-Pérez and N. R. Arista, "Hydrodynamical model for bulk and surface plasmons in cylindrical wires," Surf. Sci. **603**, 1–13 (2009).

20. A. Aubry, D. Y. Lei, S. A. Maier, and J. B. Pendry, "Interaction between plasmonic nanoparticles revisited with transformation optics," Phys. Rev. Lett. **105**, 233901 (2010).

21. J. P. Kottmann and O. J. F. Martin, "Plasmon resonant coupling in metallic nanowires," Opt. Express **8**, 655–663 (2001).

22. E. Prodan, C. Radloff, N. J. Halas, and P. Nordlander, "A hybridization model for the plasmon response of complex nanostructures," Science **302**, 419–422 (2003).

23. D. W. Brandl, C. Oubre, and P. Nordlander, "Plasmon hybridization in nanoshell dimers," J. Chem. Phys. **123**, 024701 (2005).

24. T. J. Davis, D. E. Goméz, and K. C. Vernon, "Simple model for the hybridization of surface plasmon resonances in metallic nanoparticles," Nano Lett. **10**, 2618–2625 (2010).

25. A. L. Koh, A. I. Fernández-Domínguez, D. W. McComb, S. A. Maier, and J. K. W. Yang, "High-resolution mapping of electron-beam-excited plasmon modes in lithographically defined gold nanostructures," Nano Lett. **11**, 1323–1330 (2011).

26. R. Fuchs and F. Claro, "Multipolar response of small metallic spheres: nonlocal theory," Phys. Rev. B **35**, 3722–3727 (1987).

27. R. Rojas, F. Claro, and R. Fuchs, "Nonlocal response of a small coated sphere," Phys. Rev. B **37**, 6799–6808 (1988).

28. V. Yannopapas, "Non-local optical response of two-dimensional arrays of metallic nanoparticles," J. Phys. Condens. Matt. **20**, 325211 (2008).

29. J. Zuloaga, E. Prodan, and P. Nordlander, "Quantum description of the plasmon resonances of a nanoparticle dimer," Nano Lett. **9**, 887–891 (2009).

30. J. Aizpura and A. Rivacoba, "Nonlocal effects in the plasmons of nanowires and nanocavities excited by fast electron beams," Phys. Rev. B **78**, 035404 (2008).

31. O. Nicoletti, M. Wubs, N. A. Mortensen, W. Sigle, P. A. van Aken, and P. A. Midgley, "Surface plasmon modes of a single silver nanorod: an electron energy loss study," Opt. Express **19**, 15371–15379 (2011).

32. E. S. Barnard, T. Coenen, E. J. R. Vesseur, A. Polman, and M. L. Brongersma, "Imaging the hidden modes of ultra-thin plasmonic strip antennas by cathodoluminescence," Nano Lett. **11**, 4265–4269 (2011).

33. A. L. Fetter, "Electrodynamics of a layered electron gas. I. Single layer," Ann. Phys. (N.Y.) **81**, 367–393 (1973).

34. Z. F. Öztürk, S. Xiao, M. Yan, M. Wubs, A.-P. Jauho, and N. A. Mortensen, "Field enhancement at metallic interfaces due to quantum confinement," J. Nanophoton. **5**, 051602 (2011).

35. M. S. Gockenbach, *Understanding and Implementing the Finite Element Method* (SIAM, 2006).

36. J. Merlein, M. Kahl, A. Zuschlag, A. Sell, A. Halm, J. Boneberg, P. Leiderer, A. Leitensdorfer, and R. Bratschitsch, "Nanomechanical control of an optical antenna," Nat. Photonics **2**, 230–233 (2008).

37. R. Marty, G. Baffou, A. Arbouet, C. Girard, and R. Quidant, "Charge distribution induced inside complex plasmonic nanoparticles," Opt. Express **18**, 3035–3044 (2010).

38. W. Ding, R. Bachelot, S. Kostcheev, P. Royer, and R. E. de Lamaestre, "Surface plasmon resonances in silver bowtie nanoantennas with varied bow angles," J. Appl. Phys. **108**, 124314 (2010).

39. H. Wallén, H. Kettunen, A. Sihvola, "Surface modes of negative-parameter interfaces and the importance of

rounding sharp corners," Metamaterials **2**, 113–121 (2008).

40. X. Cui and D. Erni, "The influence of particle shapes on the optical response of nearly touching plasmonic nanoparticle dimers," J. Comput. Theor. Nanosci. **7**, 1610–1615 (2010).

41. J. Zuloaga and P. Nordlander, "On the energy shift between near-field and far-field peak intensities in localized plasmon systems," Nano Lett. **11**, 1280–1283 (2011).

---

1. Introduction

In plasmonics [1–3], subwavelength metal structures are used to confine and enhance [4, 5], guide [6, 7], and scatter [8–11] light. The goal to measure and control light at ever smaller length scales drives the research field towards true nanoplasmonics. It is then a natural question to ask: down to which sizes is the optical description of the metal solely in terms of its bulk dielectric function still accurate?

One phenomenon beyond this usual description that becomes important is nonlocal optical response [1, 12–17]: the fact that not only light but also moving electrons in the metal transport energy. Here we will focus on effects due to nonlocal response, using the linearized hydrodynamic Drude model [1, 16, 18, 19]. Compared to the usual local-response Drude theory for free electrons, this hydrodynamic theory has the Fermi velocity of the electrons as an additional parameter.

Nowadays, simulating local-response plasmonic properties has almost become a standard task, even for complex geometries, thanks to the availability of advanced numerical methods and dedicated software. Because of the continuing success in fabricating ever smaller plasmonic nanostructures, the nonlocal response will become increasingly important. This has stimulated us to develop a similar reliable and easy-to-use numerical tool also for nonlocal response, and apply it to geometries where we expect effects of nonlocal response to be significant, as presented here. The nonlocal calculations are numerically more challenging, since the Fermi wavelength λ_F which is 0.5 nm both for silver and gold enters as a new length scale of longitudinal waves [1, 16, 18, 19]. The computational grid with typical separations $\Delta\mathbf{x}$ should resolve not just the sub-wavelength features, but rather sub-Fermi-wavelength features of the geometry of typical size $\mathbf{L}$ and field distributions for optical wavelengths λ. The numerical grid size $\Delta\mathbf{x}$ must be smaller than all physical length scales in our study, and the latter satisfy $\lambda_F < \mathbf{L} \ll \lambda$.

The core of this article is a numerical study of nonlocal-response effects when light scatters off nanoplasmonic dimer structures, which are archetypical structures to study both field enhancement [4, 20], scattering [8, 9], and hybridization of plasmonic resonances [21–24]. Important is also that dimers can display resonances in the visible [25] even when their two constituents, taken separately, would not. As is known from local-response hybridization theory, hybridization energies grow as dimer distances are reduced. Here we study how nonlocal response affects his behavior. Our study of nanowire dimers complements recent work on dimers of nanospheres [14, 17, 26–28]. Here we present results for dimer separations only down to 1 nm, because for smaller separations, quantum effects not taken account into our model are predicted to strongly reduce hybridization energies [29]. We focus solely on extinction cross sections and field enhancements that can be probed with light, leaving for later study the dark modes of the nanowire dimers that could be seen in electron energy loss spectroscopy [25, 30, 31] or cathodoluminescence experiments [32].

The structure of this article is as follows. In Sec. 2 we introduce the theoretical formalism, and the numerical implementation in Sec. 3. In Sec. 4 we benchmark our implementation of the hydrodynamical Drude model against the analytically solvable problem of the scattering off a single cylindrical nanowire, and also study the size dependence of nonlocal effects. In Sec. 5 we compare nonlocal response against local response for dimers consisting of two such cylindrical nanowires where field enhancement occurs in the open cavity between the cylinders. Then in

Sec. 6 we do the same for bow-tie dimer nanowires, where field enhancement occurs near the almost touching sharp tips of the triangles. Our conclusions are given in Sec. 7, and details on our numerical calculations in the Appendix.

2. Theoretical formalism

The usual local-response dielectric function of realistic metals is the sum of a Drude free-electron response plus interband effects [2, 11]. In the hydrodynamic description, only the free-electron response is modified while the other (interband) effects are unaltered. In the Maxwell wave equation for the electric field $\mathbf{E}$, the free-electron response is described by a current density $\mathbf{J}$, while the rest of the optical response is modeled with a local, usually spatially piecewise constant, dielectric function $\varepsilon_{\text{other}}(\mathbf{r}, \omega)$. We are interested in the linear optical response, and the linearized hydrodynamical model then leads to coupled equations for the electric field $\mathbf{E}$ and the current density $\mathbf{J}$ [1, 16]

$$\nabla \times \nabla \times \mathbf{E}(\mathbf{r}, \omega) = \varepsilon_{\text{other}}(\mathbf{r}, \omega) \frac{\omega^2}{c^2} \mathbf{E}(\mathbf{r}, \omega) + \mathrm{i}\omega\mu_0 \mathbf{J}(\mathbf{r}, \omega), \tag{1a}$$

$$\frac{\beta^2}{\omega(\omega + \mathrm{i}/\tau_{\text{Drude}})} \nabla\left[\nabla \cdot \mathbf{J}(\mathbf{r}, \omega)\right] + \mathbf{J}(\mathbf{r}, \omega) = \sigma(\mathbf{r}, \omega)\mathbf{E}(\mathbf{r}, \omega). \tag{1b}$$

This linearization is valid as long as first-order variations in the electron density are small compared to the static electron density. Also in linear response, this static electron density is homogeneous inside the metal while it is vanishing outside. In Eq. (1b), this electron density has been parameterized by the spatially piecewise constant AC Drude conductivity $\sigma(\mathbf{r}, \omega)$, which equals $\sigma_0/(1 - \mathrm{i}\omega\tau_{\text{Drude}})$ in the metal and vanishes elsewhere. The $\sigma_0 = \mathbf{n}_0 \mathbf{e}^2 \tau_{\text{Drude}}/\mathbf{m}$ is the DC Drude conductivity, where $\mathbf{n}_0$ is the static electron density and τ_{Drude} is the Drude damping time that also occurs in the Drude local-response dielectric function $\varepsilon(\omega) = 1 - \omega_{\text{p}}^2/[\omega(\omega + \mathrm{i}/\tau_{\text{Drude}})]$, where ω_{p} is the plasma frequency. We take parameters for gold, namely the plasma frequency $\hbar\omega_{\text{p}} = 8.812\,\text{eV}$, Drude damping $\hbar/\tau_{\text{Drude}} = 0.0752\,\text{eV}$, and Fermi velocity $\mathbf{v}_{\text{F}} = 1.39 \times 10^6\,\text{m/s}$, the same values as in Refs. [15, 16]. In the Thomas–Fermi model and for $\omega_{\text{p}}\tau_{\text{Drude}} \gg 1$, the nonlocal-response parameter β is proportional to the Fermi velocity through $\beta = \sqrt{3/(\mathbf{D}+2)}\mathbf{v}_{\text{F}}$. Here $\mathbf{D}$ is the number of spatial dimensions from the point of view of the electron dynamics, which is the number of dimensions that are not quantum confined [33]. For $\beta \rightarrow 0$ we recover the local-response model where the dynamics is governed by Ohm's law with $\mathbf{J} = \sigma\mathbf{E}$. We leave out the additional complexity of interband effects by taking $\varepsilon_{\text{other}}(\mathbf{r}, \omega) \equiv 1$ in Eq. (1a). The interband effects could be taken into account as well, following Refs. [14, 15, 17].

As stated in the Introduction, we do not consider the 'spill-out' of the electron density at the metal surface leading to quantum tunneling, as described by microscopic many-body calculations [29, 34]. As an immediate consequence of this approximation, the normal component of the current $\mathbf{J}$ vanishes at the surface of the metal volume(s). We proceed to solve the coupled equations (1) self-consistently, with the usual Maxwell boundary conditons plus the additional boundary condition of the vanishing normal component of the current $\mathbf{J}$ at the metal surface(s). For further details of the model and the appropriate boundary conditions we refer to our recent theoretical work [16].

3. Computational method and implementation

We first discuss the light extinction properties of infinitely long nanowire structures surrounded by free space. Since the electrons are confined in two directions but not quantum-confined in the nanowires, we should take $\mathbf{D} = 3$ whereby the nonlocal parameter becomes $\beta = \sqrt{3/5}\mathbf{v}_{\text{F}}$ [33].

As the light source, we take a monochromatic plane wave incident normal to the wire axis and with an in-plane polarized electric field (TM polarization).

We solve Eq. (1) numerically with the aid of a finite-element method (FEM). To obtain a reliable and flexible implementation, we have built it as a nonlocal-response extension of a commercially available multi-purpose code for local-response (the RF module of Comsol Multiphysics, version 4.1). The FEM is known to have a high ability to handle complex geometries, and to accurately model small surface details, such as gaps and tips [35]. Furthermore, retardation is automatically taken fully into account, which is important according to the very recent study by David and García de Abajo [17].

The translational invariance of the structure in one spatial dimension simplifies the calculation, since the calculation domain (or 'grid') becomes two-dimensional. Within this plane, the wire geometry can be chosen at will. We imbed the 2D-projection of our metallic nanostructure into a square computational domain. Perfectly-matched layers (PML) at the edges of this domain mimic the reflectionless coupling to the surrounding free space. For the meshing of the geometry we take advantage of the built-in algorithm of the software, paying special attention to mesh refinement needed to account for surface effects and abrupt changes in the surface topography.

Our code runs on a pc. For details about our hardware implementation we refer to the Appendix. The code was first successfully tested in the limit $\beta \to 0$ [see Eq. (1b)], where it correctly reproduces the local scattering response of various standard problems. Below, we report our benchmarking against analytical results, both for local and for nonlocal response.

4. Benchmark problem: a single cylindrical nanowire

First we compare our numerical method against analytical results for a single cylindrical nanowire, where the cylindrical symmetry allows for analytical solutions in terms of Bessel and Hankel functions, both for local and for nonlocal response [16, 18]. Figure 1 summarizes the results of our benchmarking, and illustrates the strong dependence of the nonlocal effects on the subwavelength size of the nanostructure. The figure shows the dimensionless scaled extinction cross section σ_{ext}, defined as the cross section per length of the wire, divided by its diameter. In more detail, $\sigma_{\text{ext}} = (|\mathbf{P}_{\text{abs}}| + |\mathbf{P}_{\text{scat}}|)/(2\mathbf{a}\mathbf{I}_0)$, where $\mathbf{I}_0$ represents the intensity of the incident plane wave, $\mathbf{P}_{\text{abs}}$ the absorbed and $\mathbf{P}_{\text{scat}}$ the scattered power per length of the wire, and $2\mathbf{a}$ is its diameter. The powers are obtained by numerically integrating the Poynting vector on a circle surrounding the nanowire.

Figure 1(a) compares the numerical results for a nanowire of radius $\mathbf{a} = 2\,\text{nm}$ to the exact analytical solution, Eq. (4) in Ref. [16], both for local and nonlocal response. For these tiny nanowires, nonlocal effect can be considerable. To give two examples, the relative difference of σ_{ext} for nonlocal against local response in the figure can be up to 15.33, and the resonant frequency is 6.20 eV for local and 6.39 eV for nonlocal response, a considerable blueshift of $\Delta = 0.19\,\text{eV}$, being more than 2 % of the resonance frequency.

The analytical and numerical curves overlap almost completely for the local-response model, and likewise for the hydrodynamical nonlocal model. Hence only two of the four curves are visible. Thus our numerical model accurately captures the prominent effects of nonlocal response, namely the blueshift of the (localized) surface-plasmon resonance $\omega_{\text{p}}/\sqrt{2}$ [14, 16–18], as well as the confined bulk plasmon resonances above the plasma frequency ω_{p} [16, 18]. More quantitatively, the relative error of the numerically computed cross section for nonlocal response is always smaller than 0.4% in the entire frequency range of the figure, which includes many resonances, while for local response the relative error is always smaller than 0.6%. Further details about the accuracy and convergence of our numerical implementation are given in the Appendix.
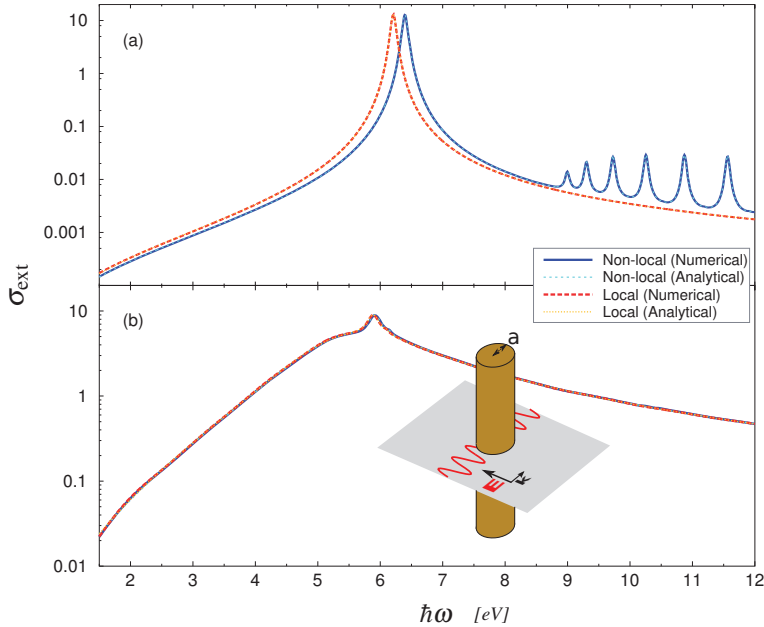
Fig. 1. Extinction-cross section σ_{ext} (logarithmic scale) versus frequency for cylindrical nanorods for two radii: (a) radius **a** = 2 nm, (b) **a** = 25 nm. σ_{ext} is normalized to the diameter of the rod. Both panels show comparisons of numerical simulations of Eq. (1) to analytical results both for local response ($\beta = 0$) and for nonlocal response ($\beta = \sqrt{3/5}\mathbf{v}_F$). All numerical curves overlap the corresponding analytical curves.

Figure 1(b) shows the analogous four curves as Fig. 1(a), but now for a larger cylinder with radius **a** = 25 nm. As one can see, the four curves all overlap almost completely. Over the frequency range 1.5 to 12 eV, the maximum relative difference in cross section for the nonlocal against the local model is 7%, which means that for most practical purposes nonlocal effects will be negligible for a single nanowire of this size. However, as we will see in Sec. 5, this conclusion does not carry over to a dimer of two such nanowires! The maximum relative error in the numerically computed cross section for nonlocal response in Fig. 1(b) is 0.89% while for local response it is 0.86%. These numbers show that the numerical method is accurate in a large frequency range also for larger nanostructures, here up to sizes where nonlocal effects can be neglected.

Summarizing, the implementation for the cylindrical nanowire is accurate in a wide range of frequencies and length scales, correctly reproducing the location of resonances and their amplitudes even for high frequencies beyond the plasma frequency.

5. Nonlocal effects in dimers of cylindrical nanowires

Having addressed single isolated nanowires, we now turn to nanowire dimers. For two closely separated nanostructures, the usual local-response model predicts a strong hybridization of the (localized) surface-plasmon resonance [22,24]. Thus dimers can even display resonances in the visible, with strongly enhanced fields in the tiny gap separating the two parts. Here we study the effects of nonlocal response both on the hybridization and on the field enhancement. We

consider dimers of cylindrical nanowires (in this section) and bow-tie nanowires in Sec. 6.

For definiteness, we consider a dimer of two identical cylindrical nanowires, with the same radius $\mathbf{a} = 25\,\text{nm}$ as for the single nanowire of Fig. 1(b), and separated by a few-nm gap of size $\mathbf{d} \ll \mathbf{a}$. When excited by a plane wave normal to the wire axis and with the electric field polarized across the dimer gap, the surface modes for this structure become highly confined to – and enhanced in – the narrow region of the gap. This field configuration is due to the hybridization of the modes of the isolated nanorods [14, 22, 23].

We examine the effects of nonlocal response on energy confinement and field enhancement for several gap sizes of 1 nm and beyond, where quantum tunneling, absent in our model, can be neglected [29]. The results for cylindrical dimers are summarized in Fig. 2. We first discuss the three panels (a1-a3) on the left of Fig. 2, that depict extinction cross sections for increasing gaps, before addressing the average field enhancements in the right-hand panels.

The results in panel (a1) corresponding to a very small gap of $\mathbf{d} = 1\,\text{nm}$ show a strong plasmonic interaction between the two nanowires. This interaction gives rise to a pronounced hybridization and consequently the main surface-plasmon resonance (SPR) now appears at much lower energy of 3.28 eV for local response and 3.40 eV for nonlocal response, as opposed to the SPR in an isolated wire around 5.91 eV in both local and nonlocal case, recall Fig. 1(b). The important point is a pronounced nonlocal blueshift of 0.12 eV of the hybridized dimer resonance. As the separation is doubled to $\mathbf{d} = 2\,\text{nm}$, the hybridization decreases and consequently the SPR appears at higher frequency around 3.63 eV for local and 3.69 eV for nonlocal response. Again the effect of nonlocal response is a noticeable blueshift of the hybridized dimer resonance, still noticeable but smaller than for $\mathbf{d} = 1\,\text{nm}$. Finally, for $\mathbf{d} = 3\,\text{nm}$, the hybridization is again weaker, so that the SPR is again blueshifted in the direction of the single-nanowire SPR (see Fig. 1). In all three cases, there is a nonlocal blueshift of the SP resonance frequency. This shift vanishes for larger $\mathbf{d}$, because the blueshift for single nanowires with radius $\mathbf{a} = 25\,\text{nm}$ also vanishes, as we saw in Fig. 1(b).

Now let us discuss the field enhancement in the right panels of Fig. 2, or more precisely the local field (intensity) enhancement factor $\gamma(\mathbf{r}) = |\mathbf{E}(\mathbf{r})|^2/|\mathbf{E}_0|^2$, where $\mathbf{E}(\mathbf{r})$ is the local electric field and $\mathbf{E}_0$ the amplitude of the incoming plane wave. Dimers support modes that are strongly localized in the gap separating the two nanowires. Due to the strong spatial localization, the amplitude of the local electric field $\mathbf{E}(\mathbf{r})$ may by far exceed the amplitude $\mathbf{E}_0$ of the incoming plane wave. Rather than considering local field enhancements in single points, we will consider spatially averages, because local field probes such as atoms cannot be positioned with infinite precision. The average field enhancements $\langle\gamma\rangle$ in Fig. 2(b) were obtained by line-averaging $\gamma(\mathbf{r})$ over the narrow gap along the axis ℓ of the dimer, i.e.

$$\langle\gamma\rangle = \frac{\int_\ell d\mathbf{r}\,\gamma(\mathbf{r})}{\int_\ell d\mathbf{r}} = \frac{1}{\mathbf{E}_0^2\mathbf{d}} \int_\ell d\mathbf{r}\,|\mathbf{E}(\mathbf{r})|^2. \tag{2}$$

A direct comparison of left and right panels of Fig. 2 shows that the spectral dependence of the field enhancement $\langle\gamma\rangle$ for lower frequencies is similar to the corresponding extinction cross section σ_{ext}. However, $\langle\gamma\rangle$ peaks at higher frequencies than σ_{ext}, both for local and nonlocal response. The agreement between the two types of curves is not complete, because the extinction cross section is the sum of a scattering and an absorption cross section. The latter can be interpreted as a two-dimensional loss average **inside** the cylinders, whereas the field enhancement factor $\langle\gamma\rangle$ of Eq. (2) is a more local one-dimensional spatial average of the empty space **in between** the cylinders. For that reason, the extinction σ_{ext} can be high near 6 eV while the field enhancement $\langle\gamma\rangle$ is low. Indeed, there exists a resonant hybridized mode at this frequency (hence the peak in σ_{ext}) with a mode profile with low intensity on the line joining the cylinder centers (which explains the low value for $\langle\gamma\rangle$); the mode intensity grows away from this line
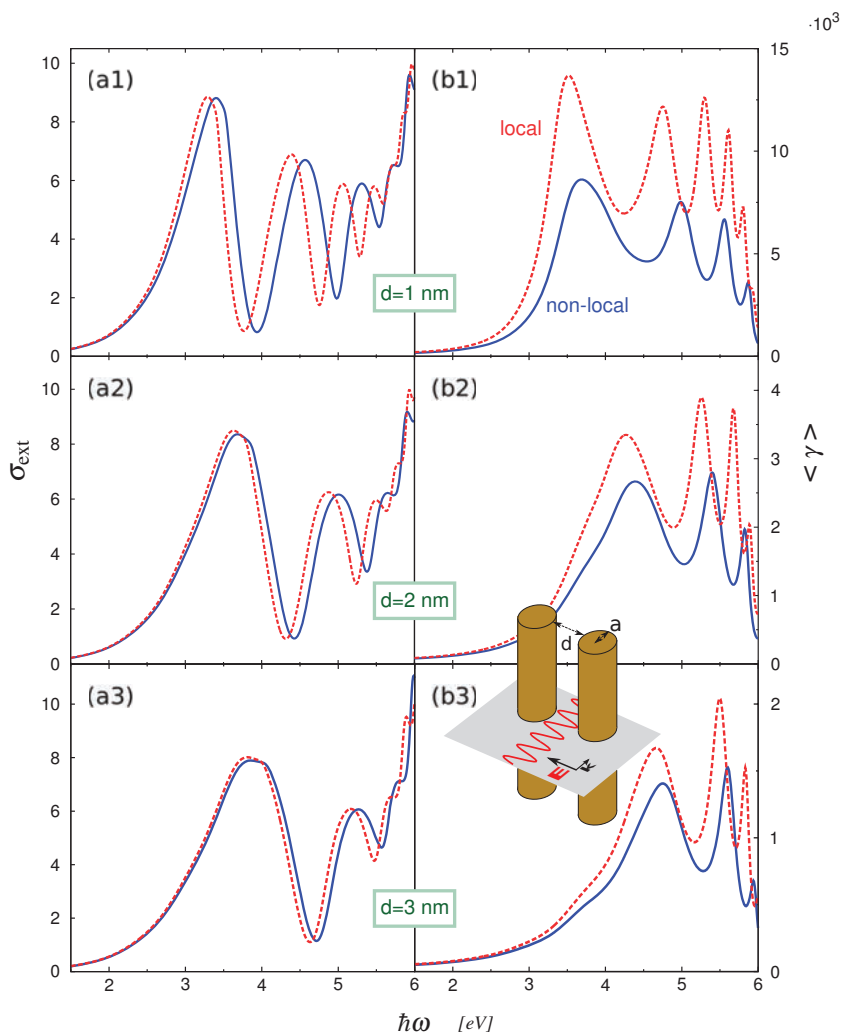
Fig. 2. Extinction-cross section versus frequency for a dimer of two cylindrical nanorods of radius **a** = 25 nm separated by a distance **d**, excited by a TM-polarized plane wave with wave vector perpendicular to the line connecting the centers of the cylinders, as illustrated in the inset with **a**/**d** not to scale. σ_{ext} is normalized to the diameter of the single wire. The left panels labeled (a) depict σ_{ext}, while the (b) panels on the right show the average field enhancement $\langle\gamma\rangle$ as defined in the main text. The upper panels (a1) and (b1) correspond to **d** = 1 nm, where the SPR appears at 3.28 eV and 3.40 eV for the local and nonlocal case, respectively. The middle panels (a2) and (b2) concern **d** = 2 nm where the SPR appears at 3.63 eV in the local case and at 3.69 eV in the nonlocal one. The lower panels (a3) and (b3) correspond to **d** = 3 nm.

(mode profile not shown). Such resonant modes suffer from our definition of field enhancement, one could say: their average field enhancement as we defined it shows no maximum where the extinction does peak.

For the narrowest gap of $\mathbf{d} = 1\,\text{nm}$, Fig. 2(b1) shows a field enhancement of $\langle \gamma \rangle = 1.4 \times 10^4$ at the main SPR (i.e. at the lowest-energy peaks) for local response, and of $\langle \gamma \rangle = 8.6 \times 10^3$ for nonlocal response. Thus, the nonlocal response gives a strong average field enhancement, yet it is considerably smaller than for local response. As the gap distance increases to $\mathbf{d} = 2\,\text{nm}$, the maxima of $\langle \gamma \rangle$ decrease for both types of material response. Finally in Fig.2(b3) the gap has been increased further to $\mathbf{d} = 3\,\text{nm}$, and we still find considerable differences for nonlocal response, even though there is a further decrease both of the peak amplitudes of $\langle \gamma \rangle$ and of their relative differences.

Thus we find for the scattering off cylindrical nanowire dimers with radius $\mathbf{a} = 25\,\text{nm}$ separated by 1 to 3 nm that nonlocal-response effects are considerable, for cross sections but more so for field enhancements, even though in Sec. 4 we found that nonlocal effects were negligible for the single cylindrical nanowire with the same radius.

The above discussion compares peak enhancements, which are significantly lower for non-local response. Since the nonlocal peaks also shift in frequency, the nonlocal effects are even more pronounced when studying observables at fixed frequencies. For then Fig. 2(a1) shows that σ_{ext} can be reduced by a factor of 3.1 at 4.0 eV, and enhanced by a factor of 3.4 at 3.7 eV. Nonlocal field enhancements for some frequencies can also turn out to be just a bit larger, for example by a factor 1.34 at 5.95 eV in Fig. 2(b3), even though we mostly find smaller nonlocal values for the field enhancement $\langle \gamma \rangle$ in between the cylinders. Finally, it is interesting to notice frequencies in Fig. 2(b) at which the local-response field enhancement peaks while the nonlocal-response field enhancement goes through a minimum.

6. Nonlocal effects in bow-tie nanowires

Let us now consider light scattering off the bow-tie nanowire dimer, the geometry as sketched in the inset of Fig. 3. Bow-tie structures can give rise to high field enhancement near the almost touching sharp tips of the two triangles [32,36–38]. Sharp features in nanoplasmonic structures are known to give strong field enhancements. The cylindrical dimer of the previous section did not have this type of field enhancement, and therefore it is interesting to compare nonlocal effects on field enhancement for the two types of dimers.

In particular, we consider a dimer of two equilateral triangular nanowires with side $\mathbf{L} = 45\,\text{nm}$. The tips of the triangles have been rounded with a radius of curvature of 1 nm. Such rounding for computational reasons is common practice [10,39,40]. In Fig. 3 we present extinction cross sections and average field enhancements for bow-tie dimers, analogous to Fig. 2. The field enhancements are averaged over the line connecting the almost touching tips of the triangles.

The results resemble those for the circular dimers, but with narrower and thus less overlapping plasmon resonances. One main feature is again that all (hybridized) surface-plasmon resonances are blueshifted due to nonlocal response. The case $\mathbf{d} = 1\,\text{nm}$ shows a strong interaction between the plasmons localized on the tip of the triangles, and the main SPR appears at 2.86 eV for local and 2.96 eV for nonlocal response. Larger distances imply weaker hybridization so that lowest-energy resonances shift to higher energies. Indeed for $\mathbf{d} = 2\,\text{nm}$ the resonance frequency of the main SPR is 3.08 eV in the local model but blueshifted by 0.07 eV in the nonlocal one. Finally for $\mathbf{d} = 3\,\text{nm}$ the main SPR occurs at 3.24 eV in the local case and 3.29 eV in the non-local one. As for the dimer of cylinders, for the bow-tie nanowire dimer we find larger nonlocal blueshifts of peaks in σ_{ext} in case of increased hybridization of surface-plasmon resonances.

As to the importance of nonlocal effects in the field enhancement for the bow-tie dimer,
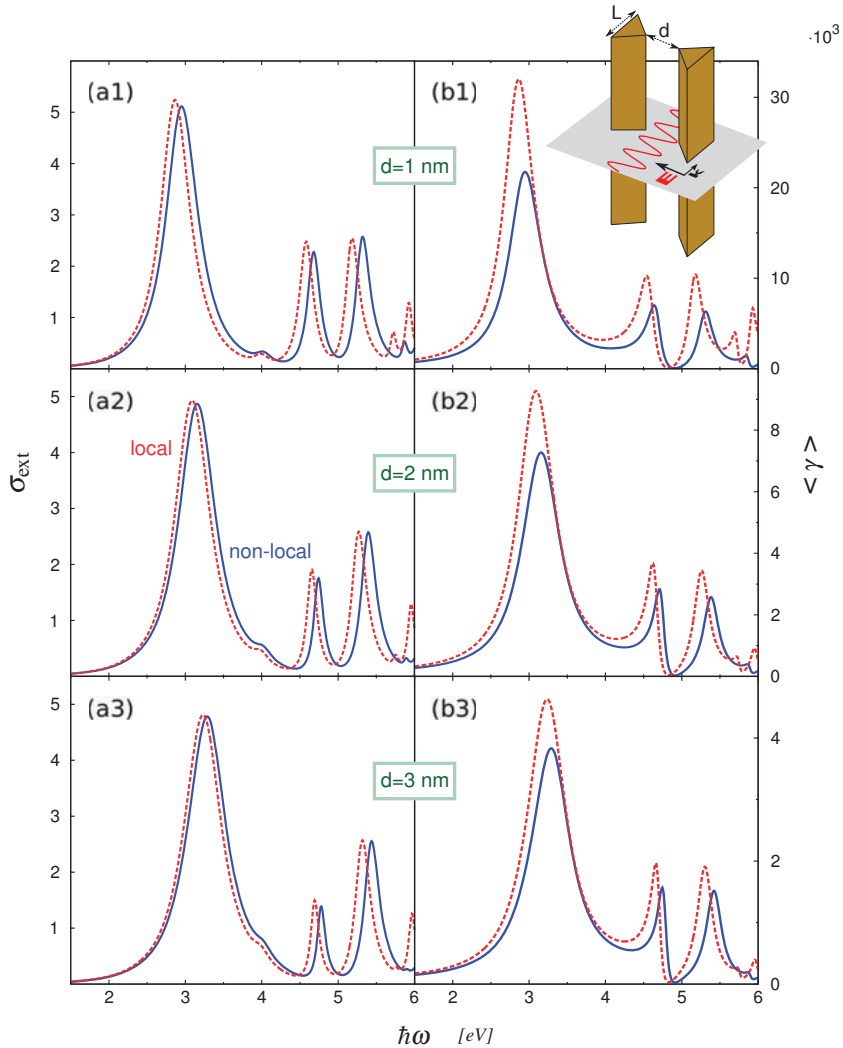
Fig. 3. Extinction-cross section versus frequency for a dimer of two equilateral triangles nanowires of side $L = 45$ nm separated by a distance d, excited by perpendicularly incident TM-polarized light. The inset shows a sketch with d/L not to scale. As in Fig. 2, the left and right panels show extinction cross sections σ_{ext} and average field enhancements $\langle\gamma\rangle$, respectively. Upper, middle, and lower panels again correspond to $d = 1, 2$ and 3 nm.

Fig. 3(b) shows that $\langle\gamma\rangle$ peaks at 3.2×10^4 in the local case and at 2.17×10^4 in the nonlocal case for $d = 1$ nm. For the tip distance $d = 2$ nm these values are 9.2×10^3 and 7.2×10^3, respectively, and they become 4.7×10^3 and 4.6×10^3 for $d = 3$ nm. For field enhancement, like for cross sections, nonlocal effects turn out to be more important in case of stronger hybridization.

If instead of focusing on peak values we compare again nonlocal with local response at fixed

frequencies, then for bow-tie dimers we can easily identify frequency intervals for which the field enhancement is larger for nonlocal than for local response, in contrast to what we found for the cylindrical dimers. For $\mathbf{d} = 3$ nm at 4.81 eV, $\langle \gamma \rangle$ is even 14.3 times larger for nonlocal than for local response. And for some frequencies, the nonlocal cross section is larger while for other frequencies it is smaller than the local response, and all differences are roughly within a factor of 5. Near 4.8 eV the field enhancements vanish even though the cross section peaks. Again this combination is a fingerprint of a resonant mode with low mode density near the center of the dimer.

The peak field enhancements $\langle \gamma \rangle$ for the bow-tie dimers in Fig. 3(b) are roughly a factor 2 higher than for the cylindrical dimers in Fig. 2(b), both for local and for nonlocal response. Thus the quite different shapes of the dimers give rise to non-negligible but not too big differences in field enhancement, considering that all enhancement peaks $\langle \gamma \rangle$ are of order 10^4 or higher. This applies both to local and to nonlocal response.

7.   Discussion and conclusions

We have implemented the hydrodynamical Drude model for arbitrary nanowire geometries as an extension of state-of-the-art numerical software in nanoplasmonics. Our code was tested against analytical results and was shown to be very accurate. We advocate the use of such benchmark problems, to be able to present results for more complex geometries with confidence.

We studied tiny cylindrical nanowires, their dimers, as well as bow-tie dimers. In all cases we find that (hybridized) surface-plasmon resonances are blue-shifted due to nonlocal response. It is not simply the size of the plasmonic nanostructure that determines whether nonlocal effects are important. For example, we found that nonlocal effects were negligible for the extinction cross section of 25 nm cylinders, but important for their closely spaced dimers.

We find that the usual explanations of plasmonic hybridization carry over to nonlocal theories. Below the plasma frequency we do not find new resonances due to nonlocal response, in agreement with our Ref. [16], but the hybridized resonances occur at higher frequencies than expected based on a local-response picture, with modified mode profiles. The nonlocal blueshifts are a correction to the larger hybridization energy splittings. As an important conclusion, we find that the nonlocal blueshifts are larger for more strongly hybridized dimer structures. It is a package deal, so to say: one cannot have the one without the other, at least for dimers for which the individual parts are too big to exhibit any nonlocal blueshift.

Bow-tie dimers have sharp tips and cylindrical dimers do not, but somewhat surprisingly this did not result in large differences in nonlocal shifts in both cases. For the extinction cross sections of the dimers we found blueshifts in resonance peaks but hardly a change in their amplitudes. For the average field enhancements on the other hand, we find both blueshifts and a reduction in height of resonance peaks, roughly by a factor of 2 for cylindrical dimers and a factor of 1.5 for the bow-tie nanowires. Nevertheless this general conclusion is fully consistent with the fact that for some fixed frequencies, the field intensities in between the cylinders or bow-ties are extra enhanced due to nonlocal as compared to local response, by up to factors of 14. We also found frequencies for which the field enhancement peaks for nonlocal response but has minimum for local response. Thus it is important to take effects of nonlocal response into account in the context of spontaneous emission rates of nearby quantum dot emitters, fluorescence of dye molecules, and surface-enhanced Raman scattering (SERS) of bio-molecules, especially in the close vicinity of strongly hybridized plasmonic nanostructures.

An important difference between the two types of dimers, we find that the gap-line averaged field enhancements of cylindrical dimers are significantly blueshifted as compared to the corresponding extinction peaks, whereas bow-tie dimers exhibit their extinction and field enhance-

ment peaks at practically the same energies. This is related to the fact that for cylinders, there exist resonant modes with low field enhancement in the gap, whereas for bowties all resonant modes have corresponding high field enhancements in the gap. There is an element of choice in the definition of "field enhancement": either one considers maximal values, line-, area-, or volume-averaged values, and on top of that there may be some arbitrariness in the respective choice of the line, area or volume that one averages over. Using a different definition of field enhancement, Ref. [41] reports redshifts of field enhancements as compared to extinction peaks, in contrast to the blueshifts that we see in Fig. 3 for the cylindrical dimers. This illustrates that the definition of the field enhancement may influence the results even qualitatively.

In this work we neglected quantum tunneling effects [29, 34]. In their quantum many-body calculations, Zuloaga **et al.** [29] identify a cross-over regime for dimer gaps between 0.5 and 1.0 nm, where narrow-barrier quantum tunneling effects strongly reduce the classical hybridization energies, and a conductive regime for $\mathbf{d} < 0.5$ nm. The classical (local-response) limit is also found in their calculations for large dimer separations. The message of our hydrodynamical calculations is that significant departures from classical local-response theory will already occur at larger dimer separations in the range 1 to 10 nm, where quantum tunneling between the dimers is negligible, and that the local-response limit is found for large separations (i.e. for the individual $\mathbf{a} = 25$ nm cylindrical wires for example). It would be gratifying to see experimental nonlocal blueshifts for dimers, and to see many-body quantum calculations confirming not only the large-separation local-response limit, but also the hydrodynamical nonlocal-response blueshifts for dimers with separations in the range 1-3 nm as presented here.

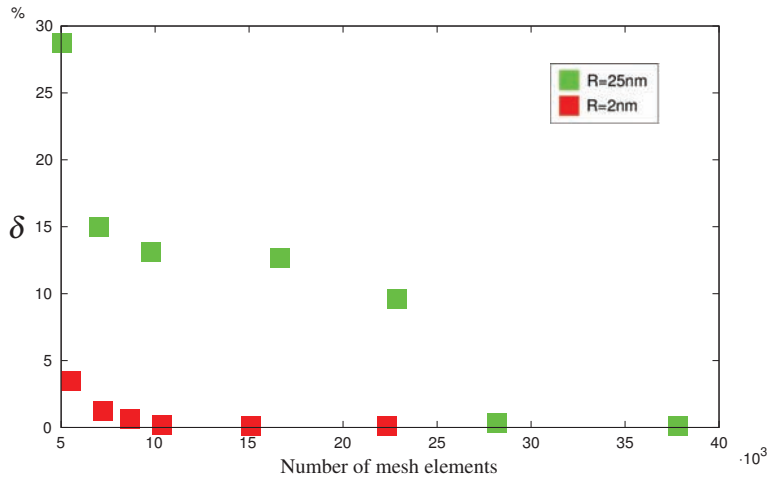## 8. Appendix: hardware implementation and accuracy studies

Fig. 4. Relative error δ of the numerically calculated extinction cross section $\sigma_{\text{ext}}^{\text{num}}$ for a single cylinder of radius $\mathbf{a} = 2$ nm at the nonlocal-response resonant frequency $\omega_{\text{sp}} = 6.38$ eV, and for a single cylinder of radius $\mathbf{a} = 25$ nm at the frequency 5.91 eV, as a function of the number of mesh elements. Modeled with parameters of Au as given in Sec. 2.

All the presented results are obtained on a personal computer equipped with four Intel 2Ghz processors and 24Gb of RAM. Single-frequency calculations typically take about one minute for regular geometries with smooth boundaries. The frequency step used to make the spectra is

0.0088 eV, and with this value all the data presented can be harvested in less than three days on our pc.

The code that we have developed has undergone several reliability tests. In Fig. 4 we present a convergence study that has been carried out for the nanorod of radius $\mathbf{a} = 2$ nm with nonlocal response. The simulation box is a square of side $\mathbf{W} = 300$ nm, surrounded by a PML that is 30 nm thick. The walls of the box are in the far-field zone of the scatterer, so that they cannot influence the field scattered away from our system under test.

First we studied the convergence of the nonlocally blueshifted value of the surface-plasmon resonance frequency, and we found that it converged to the analytical value 6.38 eV without much mesh refinement. Then at this resonance frequency, being a challenging spot, we studied the dimensionless convergence parameter $\delta = |\sigma_{\text{ext}}^{\text{num}} - \sigma_{\text{ext}}^{\text{an}}|/\sigma_{\text{ext}}^{\text{an}}$ as a function of the number of mesh elements used in the calculation. Meanwhile the number of mesh elements of both the box and the PML were kept fixed. The parameter δ represents the relative error of $\sigma_{\text{ext}}^{\text{num}}$ with respect to the $\sigma_{\text{ext}}^{\text{an}}$, so that a vanishing δ not just signifies convergence but rather convergence to the analytical value.

Figure 4 depicts δ versus the number of mesh elements. It shows that the convergence sets in for less than 8000 mesh elements, a small number for modern pc's. In particular, $\delta = 1.3\%$ for 7241 mesh elements and 0.12% for 15106 mesh elements. This means that our code could easily run on a laptop, at least for the small structures considered here. The non-uniform mesh size allows also convergence on a pc for a larger cylinder with $\mathbf{a} = 25$ nm, with $\delta = 0.11\%$ for 37830 mesh elements. Much larger structures can of course be handled on a powerful workstation.

Acknowledgments

Paper C

G. Toscano, S. Raza, S. Xiao, M. Wubs, A.-P. Jauho,
S. I. Bozhevolnyi, and N. A. Mortensen,

Surface-enhanced Raman spectroscopy: nonlocal limitations

G. Toscano,[1] S. Raza,[1,2] S. Xiao,[1] M. Wubs,[1] A.-P. Jauho,[3] S. I. Bozhevolnyi,[4] and N. A. Mortensen[1,*]

[1]*Department of Photonics Engineering, Technical University of Denmark, DK-2800 Kgs. Lyngby, Denmark*
[2]*Center for Electron Nanoscopy, Technical University of Denmark, DK-2800 Kgs. Lyngby, Denmark*
[3]*Department of Micro and Nanotechnology, Technical University of Denmark, DK-2800 Kgs. Lyngby, Denmark*
[4]*Institute of Sensors, Signals and Electrotechnics, University of Southern Denmark, DK-5230 Odense, Denmark*
*Corresponding author: asger@mailaps.org

Giant field enhancement and field singularities are a natural consequence of the commonly employed local-response framework. We show that a more general nonlocal treatment of the plasmonic response leads to new and possibly fundamental limitations on field enhancement with important consequences for our understanding of surface-enhanced Raman spectroscopy (SERS). The intrinsic length scale of the electron gas serves to smear out assumed field singularities, leaving the SERS enhancement factor finite, even for geometries with infinitely sharp features. For silver nanogroove structures, mimicked by periodic arrays of half-cylinders (up to 120 nm in radius), we find no enhancement factors exceeding 10 orders of magnitude (10^{10}).   © 2012 Optical Society of America
OCIS codes: 240.6680, 290.5860, 300.6450.

While the Raman response of (bio)molecules is inherently weak, nanostructures may be used to tailor and tremendously enhance the light–matter interactions. This is the key electromagnetic element of surface-enhanced Raman spectroscopy (SERS) [1]. In particular, metallic nanostructures [2] are known to support plasmonic field-enhancement phenomena that are beneficial for SERS [3]. In many cases, field singularities arise in geometries with abrupt changes in the surface topography. While such singularities constitute the basic electromagnetic mechanism behind SERS, the singularities are, on the other hand, an inherent consequence of the common local-response approximation (LRA) of the plasmons [4]. In this Letter, we relax this approximation and allow for nonlocal dynamics of the plasmons. To illustrate the consequences, we revisit the model geometry in Fig. 1, initially put forward by García-Vidal and Pendry [5] to qualitatively explain the electromagnetic origin of the large enhancement factors observed experimentally. The metallic surface topography is composed of a periodic structure of infinitely long metallic half-cylinders of radius R, resting shoulder-by-shoulder on a semi-infinite metal film. The steep trenches or grooves support localized surface plasmon resonances (LSPRs). Near the bottom of the groove the surfaces of the two touching half-cylinders become tangential to each other and a field singularity forms within the traditional LRA of the dielectric function. In the common treatment, the field enhancement thus eventually turns infinite [6], while it remains finite, albeit large, in any experiment reported so far. Geometrical smoothening is known to remove the singularity within the LRA and, in quantitative numerical studies, a rounding needs to be added to make numerical convergence feasible [7,8]. Thus, within the LRA framework the field enhancement would just grow without bound the sharper one could make the geometry confining the plasmon oscillations. Nonlocal effects have been shown to result in large blueshifts and considerably reduced field enhancements (as compared to a local description) in conical tips [9], metallic dimers involving small gaps below a

few nanometers [10,11], or even vanishing gaps [12]. What is the limit in field enhancements that can be achieved with (geometrically) ideal structures? This question is important not only from the fundamental but also from the applied perspective, as the answer to it would allow one to determine technological tolerances in fabrication of nanostructures designed for achieving record-high field enhancements. In this Letter we show how nonlocal response introduces a new intrinsic length scale that serves to remove the field singularities, leaving field enhancements finite even in geometries with arbitrarily sharp changes in the surface topography. For the particular geometry of Fig. 1 we evaluate $\gamma(\mathbf{r}, \omega) = |\mathbf{E}(\mathbf{r}, \omega)|^4/|\mathbf{E}_0(\omega)|^4$ and find no (surface-averaged) SERS enhancement factors $\langle \gamma \rangle$ exceeding 10 orders of magnitude.

The electromagnetic response of a metal is commonly divided into intraband contributions [13] and the dispersive Drude free-electron response

$$\varepsilon_D(\omega) = 1 + i\frac{\sigma}{\varepsilon_0 \omega} = 1 - \frac{\omega_p^2}{\omega(\omega + i/\tau_D)},$$
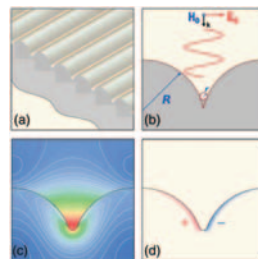

Fig. 1. (Color online) (a) Groove structure formed by an infinite periodic array of half-cylindrical nanorods. (b) Cross section of the unit cell. (c) and (d) Typical electric-field intensity and charge distributions for a dipole mode.

where σ is the complex conductivity also appearing in Ohm's law $\mathbf{J} = \sigma \mathbf{E}$. We relax the latter local-response constitutive equation and turn to a linearized hydrodynamic nonlocal treatment [10,11,14,15] where the usual Maxwell wave equation is coupled to a hydrodynamic equation for the current density; see [11] for the full details of our numerical approach. This is the simplest nontrivial extension of the common LRA Drude model, which, in addition to the usual metal parameters (ω_p, τ_D, etc.), now also carries information about the kinetics of the charge carriers at the Fermi level. The strength of the nonlocal correction to Ohm's law depends on the Fermi velocity v_F, which introduces a new length scale, being a factor v_F/c of the free-space wavelength $\lambda = 2\pi c/\omega$. For the noble metals, v_F/c is of the order 10^{-2}, which explains the overall success of the LRA. However, when exploiting plasmonics at the true nanoscale, effects due to the nonlocal dynamics start to manifest themselves. Field-enhancement structures turn out to be prime examples of this.

We consider the metallic groove structure shown in Fig. 1, which has previously been considered as a model system to mimic corrugated metal surfaces [5]. Alternatively, it may be viewed as a model for arrays of the more recent groove or channel waveguides [7,16]. In our numerical study, the structure is excited by an incoming plane wave $\mathbf{E}_0(\omega)$, normal to the substrate and with the field polarized perpendicularly to the axis of the half-cylinders, i.e., across the groove cross section. Noble metals are common choices for plasmonics and in the following we focus our attention on silver [13]. The grooves have been shown to support LSPRs [7], which we have previously explored in the context of SERS, using a LRA and with the necessary addition of geometrical smoothening [8]. To quantify the SERS effect and the consequences of nanoscale spatial dispersion, we solve the nonlocal wave equation numerically [11]. As an example of our results, Fig. 2 shows the spectral dependence of $\langle\gamma\rangle$ throughout the visible regime for groove structures with $R = 75$ nm and with a radius of curvature of the crevice given by $r = 0.1$ nm. The LSPR at $\lambda = 700$ nm allows the (surface-averaged) Raman rate to

be enhanced by a factor of 10^8. For comparison, the dashed curve shows results when treating the plasmonic response within the common LRA. In both cases, the resonant behavior is well pronounced, being caused by interference of the incoming field with the gap surface plasmon mode reflected at the bottom, similarly to that described for V grooves [16]. As a general fingerprint of nonlocal response, the peak is blueshifted compared to the expectations from a local-response treatment of the problem (this happens due to a decrease in the gap plasmon index caused by nonlocal effects [10]). In this particular case, the LSPR by the common treatment is off by more than 25 nm, which illustrates the importance of nonlocal effects for quantitative SERS predictions. Even more importantly, the common LRA is seen to significantly overestimate the enhancement factor; for some wavelengths by more than 1 order of magnitude. The large quantitative differences between the nonlocal treatment and the traditional LRA are associated with changes in the induced-charge distribution (insets of Fig. 2). In the common treatment, the charge is strictly a surface charge, while in the general nonlocal case the intrinsic scale v_F/ω serves to spatially smear out the charge distribution. Effectively, this smearing increases the electric-field penetration into the metal (silver) and thereby increases the field absorption (ohmic loss) and damping of resonant oscillations. Interpreting the field enhancement in a capacitor picture, the finite thickness of the charge distribution near the surface increases the effective separation (beyond that given by the metal-surface geometry) and, consequently, the capacitor supports a lower electrical field compared to in the LRA. In general, the intrinsic length scale of the electron gas allows one to resolve the field also in the proximity of very sharp corners and tips. On the other hand, by relaxing the sharpness of the trench the influence of spatial dispersion becomes less pronounced, as illustrated in Fig. 2 in the lower set of curves ($r = 5$ nm), where the LRA accounts well for the results obtained from a full nonlocal treatment. We note a drastic change in the field-enhancement spectrum, with the fundamental resonance now appearing at around 450 nm, due to a very rapid decrease in the gap plasmon index when the gap width increases (at the groove bottom) from 0.1 to 5 nm.

With less geometrical smoothening (i.e., when r is made smaller and smaller), the shortcomings of the LRA become more severe. The LRA anticipates a monotonically increasing enhancement factor [8], and decreasing r also causes a stronger interaction between neighboring half-cylinders and, consequently, a redshift [5]. Note that, in the interpretation based on gap surface plasmons [16], the redshift is simply related to an increase in the gap plasmon index when the gap width decreases at the groove bottom. In Fig. 3 we decrease r from 1 nm down to zero and see how nonlocal effects cause a different trend (indicated by the dashed curve) due to the competing length scales. In particular, for $r \lesssim v_F/\omega$, there is a fundamental saturation of the enhancement factor rather than a monotonic increase and, for our particular choice of the cylinder radius R, we see that the $\langle\gamma\rangle$ does not exceed 2×10^9.

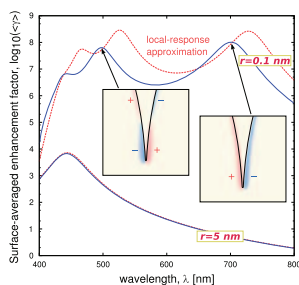To explore the ultimate limitations on the SERS in this geometry, Fig. 4 shows results where we have completely

Fig. 2. (Color online) Surface-averaged SERS enhancement factor $\langle\gamma\rangle$ for the case of $R = 75$ nm with $r = 0.1$ nm (upper curves) and $r = 5$ nm (lower curves). For comparison, the dashed curves show the results of the commonly employed LRA.
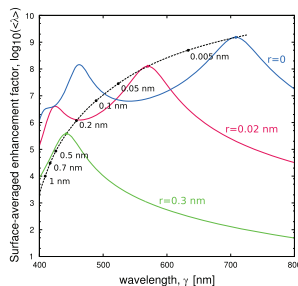
Fig. 3. (Color online) Surface-averaged SERS enhancement factor $\langle \gamma \rangle$ for the case of $R = 15$ nm and with r varying from 1 to 0 nm. The dashed curve connecting fundamental dipole resonances for different values of r serves as a guide to the eyes, clearly illustrating both a redshift and the saturation effect in the field enhancement as $r \to 0$.

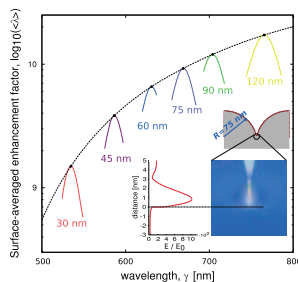Fig. 4. (Color online) Near-resonance plots of the surface-averaged SERS enhancement factor $\langle \gamma \rangle$ for arbitrarily well-defined grooves without smoothening ($r = 0$) for six cases with R varying from 30 to 120 nm. The inset shows the field-amplitude distribution $|\mathbf{E}|/|\mathbf{E}_0|$ for $R = 75$ nm.

refrained from any geometrical smoothening ($r = 0$) and where v_F/ω is the only length scale that puts fundamental limitations on the field enhancement. As the radius R of the half-cylinders is increased from 30 to 120 nm we see a redshift of the peak, as also anticipated in the LRA [8]. At the same time, the enhancement factor exhibits an increasing trend where larger cylinders support larger

field enhancement by harvesting the incoming field from larger areas. We emphasize that in all examples the field enhancement remains finite despite the fact that the crevice is arbitrarily sharp and well defined ($r = 0$). For the largest radius R considered the electromagnetic SERS enhancement factor does not exceed 2×10^{10}. This illustrates the fundamental limitations imposed by nonlocal response in our specific SERS configuration.

In conclusion, we have shown that a nonlocal treatment of the plasmonic response leads to new and possibly fundamental limitations on the electromagnetic SERS enhancement factor, thereby completely changing the message of the commonly employed LRA of the plasmons. The intrinsic length scale of the electron gas serves to smear out the field singularity that otherwise would arise from a local-response treatment and, as a consequence, the enhancement remains finite even for geometries with infinitely sharp features. Finally, beyond the linear response, fundamental limitations may arise due to nonlinearities [17].

References

1. M. Moskovits, Rev. Mod. Phys. **57**, 783 (1985).
2. S. Lal, S. Link, and N. J. Halas, Nat. Photon. **1**, 641 (2007).
3. K. Kneipp, Phys. Today **60**(11), 40 (2007).
4. Y. Luo, J. B. Pendry, and A. Aubry, Nano Lett. **10**, 4186 (2010).
5. F. García-Vidal and J. B. Pendry, Phys. Rev. Lett. **77**, 1163 (1996).
6. I. Romero, J. Aizpurua, G. W. Bryant, and F. J. García de Abajo, Opt. Express **14**, 9988 (2006).
7. E. Moreno, F. J. García-Vidal, S. G. Rodrigo, L. Martín-Moreno, and S. I. Bozhevolnyi, Opt. Lett. **31**, 3447 (2006).
8. S. Xiao, N. A. Mortensen, and A.-P. Jauho, J. Eur. Opt. Soc. Rapid Pub. **3**, 08022 (2008).
9. R. Ruppin, Phys. Lett. A **340**, 299 (2005).
10. F. J. García de Abajo, J. Phys. Chem. C **112**, 17983 (2008).
11. G. Toscano, S. Raza, A.-P. Jauho, N. A. Mortensen, and M. Wubs, Opt. Express **20**, 4176 (2012).
12. A. I. Fernández-Domínguez, A. Wiener, F. J. García-Vidal, S. A. Maier, and J. B. Pendry, Phys. Rev. Lett. **108**, 106802 (2012).
13. S. G. Rodrigo, F. García-Vidal, and Martín-Moreno, Phys. Rev. B **77**, 075401 (2008).
14. J. M. Pitarke, V. M. Silkin, E. V. Chulkov, and P. M. Echenique, Rep. Prog. Phys. **70**, 1 (2007).
15. S. Raza, G. Toscano, A.-P. Jauho, M. Wubs, and N. A. Mortensen, Phys. Rev. B **84**, 121412(R) (2011).
16. T. Søndergaard, S. I. Bozhevolnyi, J. Beermann, S. M. Novikov, E. Devaux, and T. W. Ebbesen, Nano Lett. **10**, 291 (2010).
17. P. Ginzburg, A. Hayat, N. Berkovitch, and M. Orenstein, Opt. Lett. **35**, 1551 (2010).

Paper D

Regular article

Giuseppe Toscano, Søren Raza, Wei Yan, Claus Jeppesen, Sanshui Xiao, Martijn Wubs,
Antti-Pekka Jauho, Sergey I. Bozhevolnyi and N. Asger Mortensen*

Nonlocal response in plasmonic waveguiding with extreme light confinement

Abstract: We present a novel wave equation for linearized plasmonic response, obtained by combining the coupled real-space differential equations for the electric field and current density. Nonlocal dynamics are fully accounted for, and the formulation is very well suited for numerical implementation, allowing us to study waveguides with subnanometer cross-sections exhibiting extreme light confinement. We show that groove and wedge waveguides have a fundamental lower limit in their mode confinement, only captured by the nonlocal theory. The limitation translates into an upper limit for the corresponding Purcell factors, and thus has important implications for quantum plasmonics.

Keywords: Nanoplasmonics; nonlocal response; light confinement; waveguides; light-matter interactions.

PACS numbers: 78.67.Uh; 78.67.Lt; 71.45.Lr; 73.20.Mf; 41.20.Jb.

────

*Corresponding author: N. Asger Mortensen, Department of
Photonics Engineering, Technical University of Denmark, DK-2800
Kgs. Lyngby, Denmark; and Center for Nanostructured Graphene
(CNG), Technical University of Denmark, DK-2800 Kgs. Lyngby,
Denmark, e-mail: asger@mailaps.org
Giuseppe Toscano and Claus Jeppesen: Department of Photonics
Engineering, Technical University of Denmark, DK-2800 Kgs.
Lyngby, Denmark
Søren Raza: Department of Photonics Engineering, Technical
University of Denmark, DK-2800 Kgs. Lyngby, Denmark; and Center
for Electron Nanoscopy, Technical University of Denmark, DK-2800
Kgs. Lyngby, Denmark
Wei Yan, Sanshui Xiao and Martijn Wubs: Department of Photonics
Engineering, Technical University of Denmark, DK-2800 Kgs.
Lyngby, Denmark; and Center for Nanostructured Graphene (CNG),
Technical University of Denmark, DK-2800 Kgs. Lyngby, Denmark
Antti-Pekka Jauho: Center for Nanostructured Graphene (CNG),
Technical University of Denmark, DK-2800 Kgs. Lyngby, Denmark;
and Department of Micro and Nanotechnology, Technical University
of Denmark, DK-2800 Kgs. Lyngby, Denmark
Sergey I. Bozhevolnyi: Institute of Technology and Innovation,
University of Southern Denmark, DK-5230 Odense, Denmark

Edited by Jennifer A. Dionne

Wave propagation along dielectric waveguide structures has over the years been extended also to plasmonic systems with waveguide modes in the form of surface-plasmon polaritons. Plasmonic waveguides have attracted considerable attention during the past decade, primarily due to their ability to support extremely confined modes, i.e., modes that do not exhibit a diffraction-limited cutoff for progressively smaller waveguide cross sections but transform themselves into their electrostatic counterparts [1]. Investigations of nanowire [2], groove [3] and wedge [4] waveguides, shown to ensure extreme light confinement, raise a natural interest in the influence of nonlocal effects on strongly confined plasmonic modes [5]. Waveguiding by metal nanowires [6] and more recently plasmonic focusing by conical tips [7, 8] have been studied in the context of nonlocal response. However, with the exception of few analytical studies of simple planar geometries [9, 10], nonlocal effects in the dispersion properties of complex waveguides remain unexplored, a circumstance that can partly be explained by the added complexity due to nonlocal effects as compared to the widespread framework of the local-response approximation (LRA) [11].

There is also another good reason to look for nonlocal effects in extreme light confinement. Subwavelength mode confinement implies large effective Purcell factors and thereby strong coupling of single emitters to nearby plasmonic waveguide modes [12]. The latter opens a doorway to quantum optics with surface plasmons, including the possibilities for realization of single-photon transistors [13] and long-distance entanglement of qubits [14]. Since one would expect that the plasmonic mode confinement is fundamentally limited by nonlocal effects, similarly to nonlocal limits in the field enhancement of localized plasmon excitations [15, 16], studies of the plasmonic mode confinement beyond the LRA are of great interest for quantum plasmonics. More specifically, in the LRA higher single-photon efficiencies [12] and Purcell factors [13] have been found to occur for smaller waveguide radii R, and the $R \rightarrow 0$ limit is commonly taken to estimate the strongest light-matter interactions. Nonlocal response effects

become increasingly important in this $R\to0$ limit, which is an important motivation for our present study of nonlocal effects for highly confined plasmonic waveguides.

In this Letter, we derive a novel wave equation which fully takes into account the nonlocal dynamics of an often-employed hydrodynamical model (HDM). We apply the wave equation to plasmonic waveguides (Figure 1) with extreme light confinement, defined by the subnanometer dimensions of the waveguide cross section. After stringent bench-marking of our approach against the analytically tractable case of nanowires with circular cross-section, we analyze in detail groove and wedge waveguides and demonstrate the existence of fundamental limits in their mode confinement and Purcell factors, imposed by the nonlocal effects. At the same time, our results reveal that there is room for downsizing present-day quantum plasmonic devices before these fundamental limitations set in.

The nonlocal response, or spatial dispersion, is a consequence of the quantum many-body properties of the electron gas, which we here take into account within a semi-classical model [17–20]. In this model the equation-of-motion for an electron in an electrical field is supplemented with a hydrodynamic pressure term originating from the quantum kinetics of the electron gas. By linearization, the plasmonic response is governed by the following pair of coupled real-space differential equations [21]:

$$\nabla\times\nabla\times\mathbf{E}(\mathbf{r})=\left(\frac{\omega}{c}\right)^{2}\mathbf{E}(\mathbf{r})+i\omega\mu_{0}\mathbf{J}(\mathbf{r}),\tag{1a}$$

$$\frac{\beta^{2}}{\omega(\omega+i/\tau)}\nabla[\nabla\cdot\mathbf{J}(\mathbf{r})]+\mathbf{J}(\mathbf{r})=\sigma(\mathbf{r})\mathbf{E}(\mathbf{r}).\tag{1b}$$

Here, the term $\nabla[\nabla\cdot\mathbf{J}]=\nabla\times\nabla\times\mathbf{J}+\nabla^{2}\mathbf{J}$ is a correction to Ohm's law and scales as $\beta^{2}=(3/5)v_{F}^{2}$ within the Thomas–Fermi model [22] with v_{F} being the Fermi velocity. For simplicity we neglect here any interband effects present in

real metals; these can be included straightforwardly [23, see Supplemental material]. In our numerical solutions we will consider Drude parameters appropriate for silver [24]. Assuming a hard-wall confinement associated with a high work function, the boundary conditions for the current at the metal surface become particularly simple: the tangential component is unrestricted while the normal component vanishes due to the current continuity and vanishing of all electron wave functions at the surface [10, 21].

For analytical progress one can eliminate the current from Eq. (1a), thereby arriving at an integral equation where a dyadic Green's function accounts for the nonlocal dynamics of the electron gas [25, 26]. Alternatively, the coupled equations (1a) and (1b) form a natural starting point for a numerical treatment of arbitrarily shaped metallic nanostructures, e.g., with a state-of-the-art finite-element method [23, 27]. Recently, we employed this approach to study field enhancement and SERS in groove structures [15]. However, for waveguiding geometries we seek solutions of the form $\mathbf{E}(\mathbf{r})\propto\exp(ik_{z}z)$ leading to an eigenvalue problem for $k_{z}(\omega)$ with a six-component eigenvector $\{\mathbf{E},\mathbf{J}\}$. In that context the coupled-equation formulation is numerically less attractive. Here, instead, we eliminate the current from Eq. (1b), a procedure that, after straightforward manipulations using standard vector calculus (see Supplemental material), results in an appealingly compact, but yet entirely general nonlocal wave equation:

$$\nabla\times\nabla\times\mathbf{E}(\mathbf{r})=\left(\frac{\omega}{c}\right)^{2}\hat{\varepsilon}_{NL}(\mathbf{r})\mathbf{E}(\mathbf{r}),\tag{2a}$$

$$\hat{\varepsilon}_{NL}(\mathbf{r})=\varepsilon_{D}(\mathbf{r})+\frac{\beta^{2}}{\omega(\omega+i/\tau)}\nabla^{2}.\tag{2b}$$

Here, the operator $\hat{\varepsilon}_{NL}(\mathbf{r})$ contains the nonlocal effects. In the limit $\beta\to0$, $\hat{\varepsilon}_{NL}(\mathbf{r})$ reduces to the usual Drude dielectric function $\varepsilon_{D}(\mathbf{r})=1+i\sigma(\mathbf{r})/(\varepsilon_{0}\omega)=1-\omega_{p}^{2}(\mathbf{r})/[\omega(\omega+i/\tau)]$ used in the LRA. Thus, with a simple rewriting we have turned the coupled-wave equations into a form reminiscent of the usual wave equation, with all aspects of nonlocal response contained in the Laplacian term $\beta^{2}\nabla^{2}$ in $\hat{\varepsilon}_{NL}(\mathbf{r})$. This is the main theoretical result of this Letter. In passing, we note that with Eq. (2b) we immediately recover the dispersion relation $\omega(k)=\sqrt{\omega_{p}^{2}+\beta^{2}k^{2}}$ for bulk plasmons in translationally invariant plasma (see Supplemental material). Clearly, the single-line form is beneficial for the conceptual understanding and further analytical progress, as well as for numerical implementations: the additional Laplacian does not add any complications beyond those already posted by the double-curl operator on the left-hand side equation. Likewise the boundary condition that was imposed on the current $\mathbf{J}$ in Eq. (1)
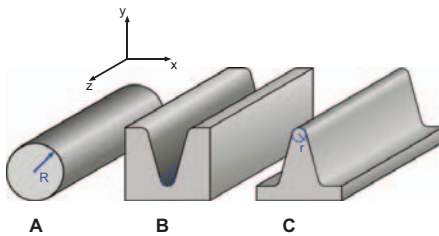
Figure 1 Generic plasmonic waveguiding geometries with wave propagation in the z-direction and extreme transverse confinement in the xy-plane due to subnanometer geometric dimensions, e.g., the nanowire radius R or the edge radius-of-curvature r.

translates into an additional boundary condition on the electric field in Eq. (2), see (Supplemental material). While Eq. (1) can be solved numerically for scattering problems [15, 23, 27] and some waveguide problems [28], the result in Eq. (2) is clearly a major advancement for efficient and accurate numerical eigenvalue solutions in waveguiding geometries with arbitrarily shaped waveguide cross sections. In particular, differential operations reduce to a Laplacian and the dimension of the eigenvalue problem is reduced from six field components to only three.

We now apply the developed formalism to the waveguide configurations of Figure 1 which can provide extreme light confinement [1]: i) metal nanowires with circular cross sections [2] where analytical solutions [7] are available for benchmarking of the numerics, ii) grooves in metal [3], and iii) metal wedges [4]. In addition to the usual mode characteristics, effective index and propagation length, we also evaluate the effective mode area: $A_{eff} = V_{eff}/L$, where V_{eff} is the effective mode volume associated with the Purcell effect, i.e.,

$$A_{eff} = \frac{\int_{V_m + V_a} \mathrm{d}x\mathrm{d}y\, u(\mathbf{r})}{\max_{V_a} \{u(\mathbf{r})\}}, \qquad (5)$$

where $u(\mathbf{r})$ is the electromagnetic energy functional (see Supplemental material). The cross-sectional integral extends over the volumes V_m and V_a occupied by metal and air, respectively, while the evaluation of the maximal energy density is restricted to the air region where dipole emitters can be placed.

The dispersion curves and effective mode areas (normalized to the nanowire cross section) calculated for silver nanowires of different radii (Figure 2A,B) exhibit a blueshift and increased mode area (for fixed k_z) when taking nonlocal effects into account. The numerical results of Eq. (2) show excellent agreement with the corresponding analytical results previously derived from Eq. (1) [7]. Importantly, nonlocal dynamics influences strongly the mode field distribution (see Figure 2C), because, contrary to the LRA case, the normal component of the electrical field within the HDM is continuous across the interfaces (this is a special case for a Drude metal without interband effects and surrounded by vacuum [See Supplemental material]). It is indeed seen (Figure 2C) that $|\mathbf{E}_\rho|$ is discontinuous on the boundary in the local case, while it varies continuously across the boundary in the nonlocal case. This variation occurs in a region extending over ≈0.1 nm, that is of the order of the Fermi wavelength of silver.

The results for cylindrical nanowires, while demonstrating the main effects of nonlocal dynamics on the mode characteristics, indicate that the quantitative
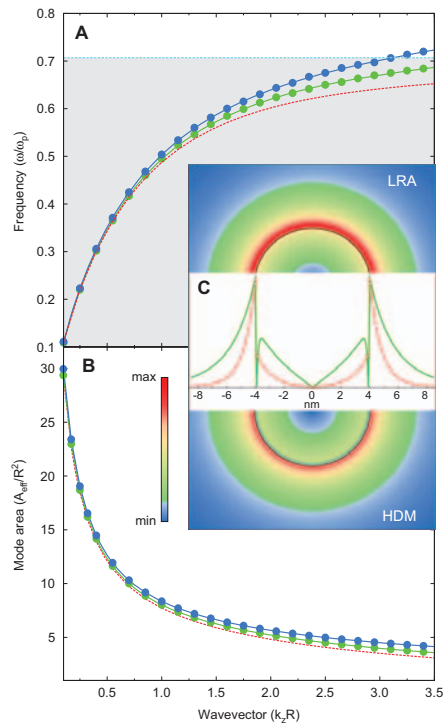
Figure 2 Fundamental waveguide mode of a cylindrical silver nanowire embedded in air. (A) Dispersion relation $\omega(k_z)$ and (B) normalized effective mode area within the HDM for the nanowire radius R=2 nm (blue) and 4 nm (green), respectively, showing excellent agreement between numerical solutions of Eq. (2) (solid points) and analytical results (solid lines). For comparison, the red-dashed curve shows the universal result of the nonretarded LRA, with its large-k_z limiting value of $\omega_p/\sqrt{2}$ indicated in (A) by the horizontal line. (C) Radial distribution of the electric field $|\mathbf{E}_\rho|$ at ω=0.6 ω_p for R=4 nm, contrasting the continuous field variation in the HDM with its usual boundary discontinuity in the LRA.

changes are modest even for very small radii (Figure 2). In order to explore *fundamental* limitations, one has to consider the limit of vanishing radii of curvature. While subnanometer radii appear unrealistic for nanowires, fabrication of grooves cut in metal and metal wedges, e.g., by nanoimprint lithography [29], can in fact result in nm-sharp edges with corresponding nm-sized wedge modes [4]. We expect that nonlocal effects then come into play.

Rather surprisingly, the mode effective index and propagation length calculated for silver grooves and

wedges (Figure 3) exhibit even weaker influence of the nonlocal effects as compared to the case of nanowires (Figure 2). In fact, there is no noticeable difference between the LRA- and HDM-based results obtained for 1-nm-radius of edges. In the limit of mathematically sharp edges, the mode effective index becomes only slightly larger and the propagation length slightly smaller than those calculated for 1 nm edge radius (Figure 3). We explain this result by the fact that groove and wedge plasmonic modes are only partially affected by the very tip, being distributed also and predominantly over flat edges (see insets in Figure 3).

The situation changes drastically when one considers the mode confinement, using the mode area associated with the Purcell factor, Eq. (3). We recall that the field enhancement calculated within the LRA grows without bound for progressively sharper pointed structures while it remains finite when calculated within HDM [15, 16]. Analogously, in the present case, one may expect that the mode area calculated within the LRA decreases without bound for a decreasing edge radius, while it may
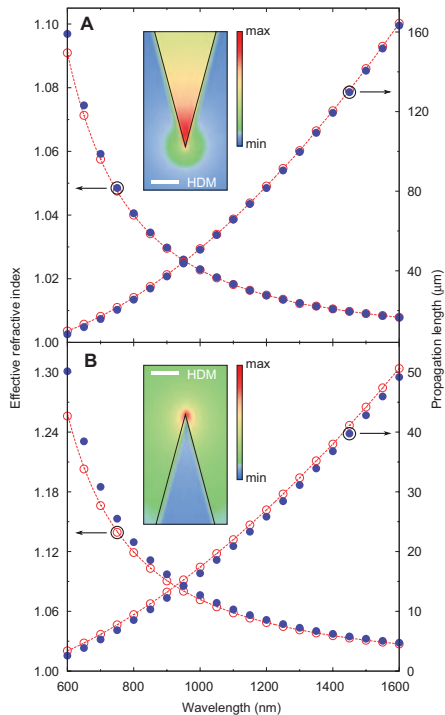
Figure 3 Effective index (left axis) and propagation length (right axis) versus wavelength for the fundamental mode in complimentary (A) V-groove and (B) wedge silver waveguides, both with an opening angle of 30°. The nonlocal results (solid circular symbols) obtained with Eq. (2) are contrasted to the LRA (open circles), with dashed lines serving as eye guides. Results for mathematically sharp structures with $r=0$ (blue solid circles) are contrasted to finite rounding with $r=1$ nm (red open circles). Insets show field-intensity distributions (white scale bars are 1 nm long) calculated within the HDM ($\lambda=600$ nm) for infinitely sharp edges. The fingerprint of nonlocal effects is clearly visible as the field penetrates into the metal by a distance of the order of the Fermi wavelength of silver.
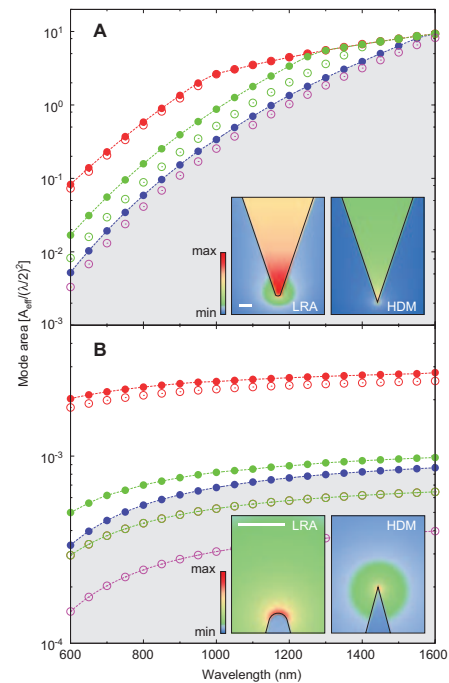
Figure 4 Normalized mode area versus wavelength for the fundamental mode in complimentary (A) V-groove and (B) wedge silver waveguides, both with opening angles of 30°. The HDM results (solid symbols) are contrasted to the LRA (open circles) for $r=1$ nm (red) and $r=0.2$ nm (green). Results for mathematically sharp structures with $r=0$ (blue solid circles) define a lower limit in the HDM (gray-shaded regions are inaccessible). For the LRA, the $r=0.1$ nm results (magenta) exceed this limit and the mode area tends to zero when $r\rightarrow0$. Insets show field-intensity distributions (white scale bars are 5 nm long) at $\lambda=600$ nm. The LRA intensities are with rounding $r=1$ nm, while $r=0$ is used for the HDM maps.

saturate within the HDM. LRA-based simulations for sub-nanometer radii of edges show (Figure 4) that the mode area indeed tends to zero, without any apparent saturation. This trend is more pronounced for wedges than for grooves, because the wedge geometry ensures generally a better mode confinement (cf. Figure 4A and B), as was also noted previously [4]. At the same time, the simulations conducted within the HDM demonstrate clearly the existence of a lower bound for the mode area which remains finite even for mathematically sharp edges (blue circles in Figure 4). The associated Purcell factors can be estimated by inverse of the normalized mode areas displayed in Figure 4 [30]. Thus, our calculations show that there is a fundamental limit for the maximum Purcell factors achievable with plasmonic waveguides. It is interesting that the upper limit of Purcell factors evaluated in this way decreases noticeably in the long-wavelength regime. This feature is related to a general weakening of all plasmonic effects, including waveguiding [1], for longer wavelengths (with metals approaching the limiting case of perfect conductors). At the same time, in the case of wedges, these factors remain substantial even at telecom wavelengths, with the propagation lengths becoming considerably long (Figure 3) and amenable for circuitry application. It should also be borne in mind that the plasmonic field confinement in both grooves and wedges increases for smaller opening angles [3, 4], so

that even larger Purcell factors can be achieved, albeit at the expense of shorter propagation.

In conclusion, using a novel wave equation accounting for nonlocal dynamics, we considered plasmonic waveguides with extreme light confinement and demonstrated the existence of a fundamental limit in their mode confinement imposed by nonlocal effects. Our results imply fundamental limitations in the corresponding Purcell factors, showing at the same time the possibility of achieving very high Purcell factors with V-groove and wedge waveguides that ensure sufficiently long propagation lengths for applications in quantum plasmonics. Here, we have focused on single-connected metal geometries where dominating currents are naturally of an Ohmic nature, whereas tunneling currents may cause important limitations too in e.g., closely spaced metallic objects [31]. Finally, beyond the linear response fundamental limitations may arise due to nonlinearities [32].

References

[1] Gramotnev DK, Bozhevolnyi SI. Plasmonics beyond the diffraction limit. Nat Photonics 2010;4:83–91.

[2] Ditlbacher H, Hohenau A, Wagner D, Kreibig U, Rogers M, Hofer F, Aussenegg FR, Krenn JR. Silver nanowires as surface plasmon resonators. Phys Rev Lett 2005;95:257403.

[3] Bozhevolnyi SI, Volkov VS, Devaux E, Ebbesen TW. Channel plasmon-polariton guiding by subwavelength metal grooves. Phys Rev Lett 2005;95:046802.

[4] Moreno E, Rodrigo SG, Bozhevolnyi SI, Martín-Moreno L, García-Vidal FJ. Guiding and focusing of electromagnetic fields with wedge plasmon polaritons. Phys Rev Lett 2008;100:023901.

[5] García de Abajo FJ. Nonlocal effects in the plasmons of strongly interacting nanoparticles, dimers, and waveguides. J Phys Chem C 2008;112:17983–7.

[6] Aers GC, Boardman AD, Paranjape BV. Non-radiative surface plasma-polariton modes of inhomogeneous metal circular cylinders. J Phys F: Metal Phys 1980;10:53.

[7] Ruppin R. Effect of non-locality on nanofocusing of surface plasmon field intensity in a conical tip. Phys Lett A 2005;340:299–302.

[8] Wiener A, Fernández-Domínguez AI, Horsfield AP, Pendry JB, Maier SA. Nonlocal effects in the nanofocusing performance of plasmonic tips. Nano Lett 2012;12:3308–14.

[9] Boardman AD, Paranjape BV, Nakamura YO. Surface plasmon-polaritons in a spatially dispersive inhomogeneous medium. Phys Stat Sol B 1976;75:347–59.

[10] Yan W, Wubs M, Mortensen NA. Hyperbolic metamaterials: nonlocal response regularizes broadband supersingularity. Phys Rev B 2012;86:205429.

[11] Maier SA. Plasmonics: fundamentals and applications. New York: Springer, 2007.

[12] Chang DE, Sørensen AS, Hemmer PR, Lukin MD. Quantum optics with surface plasmons. Phys Rev Lett 2006;97: 053002.

[13] Chang DE, Sørensen AS, Demler EA, Lukin MD. A single-photon transistor using nanoscale surface plasmons. Nat Phys 2007;3:807–12.

[14] González-Tudela A, Martín-Cano D, Moreno E, Martín-Moreno L, Tejedor C, García-Vidal FJ. Entanglement of two qubits mediated by one-dimensional plasmonic waveguides. Phys Rev Lett 2011;106:020501.

[15] Toscano G, Raza S, Xiao S, Wubs M, Jauho A-P, Bozhevolnyi SI, Mortensen NA. Surface-enhanced Raman spectroscopy: nonlocal limitations. Opt Lett 2012;37:2538–40.

[16] Ciracì C, Hill RT, Mock JJ, Urzhumov Y, Fernández-Domínguez AI, Maier SA, Pendry JB, Chilkoti A, Smith DR. Probing the ultimate limits of plasmonic enhancement. Science 2012;337:1072–4.

[17] Bloch F. Stopping power of atoms with several electrons. Z Phys A 1933;81:363.

[18] Barton G. Some surface effects in the hydrodynamic model of metals. Rep Prog Phys 1979;42:963.

[19] Boardman A. Electromagnetic surface modes. Hydrodynamic theory of plasmon-polaritons on plane surfaces. Chichester: John Wiley and Sons, 1982.

[20] Pitarke J, Silkin V, Chulkov E, Echenique P. Theory of surface plasmons and surface-plasmon polaritons. Rep Prog Phys 2007;70:1.

[21] Raza S, Toscano G, Jauho A-P, Wubs M, Mortensen NA. Unusual resonances in nanoplasmonic structures due to nonlocal response. Phys Rev B 2011;84:121412(R).

[22] Halevi P. Hydrodynamic model for the degenerate free-electron gas: generalization to arbitrary frequencies. Phys Rev B 1995;51:7497–9.

[23] Toscano G, Raza S, Jauho A-P, Mortensen NA, Wubs M. Modified field enhancement and extinction by plasmonic nanowire dimers due to nonlocal response. Opt Express 2012;20:4176–88.

[24] Rodrigo SG, García-Vidal FJ, Martín-Moreno L. Influence of material properties on extraordinary optical transmission through hole arrays. Phys Rev B 2008;77:075401.

[25] Mortensen NA, Toscano G, Raza S, Stenger N, Yan W, Jauho A-P, Xiao S, Wubs M. Nanoplasmonics beyond Ohm's law. AIP Conf Proc 2012;1475:28–32.

[26] Mortensen NA. Nonlocal formalism for nanoplasmonics: phenomenological and semi-classical considerations. 2013; arXiv:1306.4651. DOI:10.1016/j.photonics.213.06.002.

[27] Hiremath KR, Zschiedrich L, Schmidt F. Numerical solution of nonlocal hydrodynamic Drude model for arbitrary shaped nano-plasmonic structures using Nédélec finite elements. J Comp Phys 2012;231:5890–6.

[28] Huang Q, Bao F, He S. Nonlocal effects in a hybrid plasmonic waveguide for nanoscale confinement. Opt Express 2013;21:1430–9.

[29] Nielsen RB, Fernandez-Cuesta I, Boltasseva A, Volkov VS, Bozhevolnyi SI, Klukowska A, Kristensen A. Channel plasmon polariton propagation in nanoimprinted V-groove waveguides. Opt Lett 2008;33:2800–2.

[30] Oulton RF, Bartal G, Pile DFP, Zhang X. Confinement and propagation characteristics of subwavelength plasmonic modes. New J Phys 2008;10: 105018.

[31] Esteban R, Borisov AG, Nordlander P, Aizpurua J. Bridging quantum and classical plasmonics with a quantum-corrected model. Nat Commun 2012;3:825.

[32] Ginzburg P, Hayat A, Berkovitch N, Orenstein M. Nonlocal ponderomotive nonlinearity in plasmonics. Opt Lett 2010;35:1551–3.

Nonlocal response in plasmonic waveguiding with extreme light confinement:
SUPPLEMENTAL MATERIAL

G. Toscano,[1] S. Raza,[1,2] C. Jeppesen,[1] S. Xiao,[1,3]
M. Wubs,[1,3] A.-P. Jauho,[4,3] S. I. Bozhevolnyi,[5] and N. A. Mortensen[1,3*]

[1]*Department of Photonics Engineering, Technical University of Denmark, DK-2800 Kgs. Lyngby, Denmark*
[2]*Center for Electron Nanoscopy, Technical University of Denmark, DK-2800 Kgs. Lyngby, Denmark*
[3]*Center for Nanostructured Graphene (CNG), Technical University of Denmark, DK-2800 Kgs. Lyngby, Denmark*
[4]*Department of Micro and Nanotechnology, Technical University of Denmark, DK-2800 Kgs. Lyngby, Denmark*
[5]*Institute of Technology and Innovation, University of Southern Denmark, DK-5230 Odense, Denmark*

In this supplemental material we offer further details on 1) the derivation of the nonlocal wave equation, 2) the formulation of boundary conditions associated with the hydrodynamic model, 3) the derivation of a generalized energy density expression, and 4) the numerical implementation and its convergence properties.

THE NONLOCAL WAVE EQUATION

In this section of our supplemental material we derive Eq. (2) in our Letter. We start from the coupled hydro-dynamic equations, i.e. Eq. (1) in our Letter. Our first step is to isolate $\mathbf{J}$ from Eq. (1a),

$$\mathbf{J} = \frac{1}{i\omega\mu_0}\left\{\nabla\times\nabla\times\mathbf{E} - \left(\tfrac{\omega}{c}\right)^2\varepsilon_\infty\mathbf{E}\right\}, \quad (1)$$

where for generality we have included the ε_∞ interband contribution usually appearing in the Drude permittivity $\varepsilon_D = \varepsilon_\infty - \omega_p^2/[\omega(\omega+i/\tau)]$. Substituting this expression into Eq. (1b) we get

$$\tfrac{\beta^2}{\omega(\omega+i/\tau)}\nabla\left[\nabla\cdot\left\{\nabla\times\nabla\times\mathbf{E} - \left(\tfrac{\omega}{c}\right)^2\varepsilon_\infty\mathbf{E}\right\}\right]$$
$$+ \left\{\nabla\times\nabla\times\mathbf{E} - \left(\tfrac{\omega}{c}\right)^2\varepsilon_\infty\mathbf{E}\right\} = i\omega\mu_0\sigma\mathbf{E}. \quad (2)$$

Next, for any vector field $\mathbf{F}$, the divergence of its curl is zero, i.e. $\nabla\cdot(\nabla\times\mathbf{F}) = 0$. Thus, without loss of generality the expression now simplifies to

$$-\tfrac{\beta^2}{\omega(\omega+i/\tau)}\left(\tfrac{\omega}{c}\right)^2\varepsilon_\infty\nabla\left[\nabla\cdot\mathbf{E}\right]$$
$$+ \left\{\nabla\times\nabla\times\mathbf{E} - \left(\tfrac{\omega}{c}\right)^2\varepsilon_\infty\mathbf{E}\right\} = i\omega\mu_0\sigma\mathbf{E}. \quad (3)$$

Furthermore, utilizing that in general $\nabla\left[\nabla\cdot\mathbf{F}\right] = \nabla\times\nabla\times\mathbf{F} + \nabla^2\mathbf{F}$ we get

$$-\tfrac{\beta^2}{\omega(\omega+i/\tau)}\left(\tfrac{\omega}{c}\right)^2\varepsilon_\infty\left\{\nabla\times\nabla\times\mathbf{E} + \nabla^2\mathbf{E}\right\}$$
$$+ \left\{\nabla\times\nabla\times\mathbf{E} - \left(\tfrac{\omega}{c}\right)^2\varepsilon_\infty\mathbf{E}\right\} = i\omega\mu_0\sigma\mathbf{E}. \quad (4)$$

Re-grouping the double-curl terms on the left-hand side (as in the common LRA wave equation) and re-introducing the local-response Drude permittivity as $\varepsilon_D = \varepsilon_\infty + i\sigma/(\varepsilon_0\omega)$ we get

$$\nabla\times\nabla\times\mathbf{E} = \left(\tfrac{\omega}{c}\right)^2\mathcal{K}\left[\varepsilon_D + \tfrac{\beta^2\varepsilon_\infty}{\omega(\omega+i/\tau)}\nabla^2\right]\mathbf{E}. \quad (5)$$

For the re-normalization on the right-hand side we note that $\mathcal{K} = \frac{c^2}{c^2-\beta^2\varepsilon_\infty(1+i/\omega\tau)^{-1}} = 1 + \mathcal{O}(\varepsilon_\infty[\beta/c]^2[1-i/\omega\tau]^{-1})$ and for all practical purposes involving the common noble metals it is close to unity. In this way we end up with Eq. (2) in our Letter.

TRANSLATIONALLY INVARIANT SYSTEMS

For infinite systems with translational invariance it is convenient to work in Fourier space and this has been the common approach in most of the early literature. To connect our result in Eq. (5) to $\mathbf{k}$-space formalism we Fourier transform the wave equation which gives

$$-\mathbf{k}\times\mathbf{k}\times\mathbf{E} = \left(\tfrac{\omega}{c}\right)^2\left(1-\tfrac{\omega_p^2}{\omega^2}\right)\mathbf{E} - \left(\tfrac{\beta}{c}\right)^2\mathbf{k}\left(\mathbf{k}\cdot\mathbf{E}\right), \quad (6)$$

where for simplicity we have suppressed the interband contribution and the damping. Below, we will use the Helmholtz decomposition $\mathbf{E} = \mathbf{E}_t + \mathbf{E}_l$ and to clearly distinguish between transverse fields ($\mathbf{k}\cdot\mathbf{E}_t = 0$) and longitudinal fields ($\mathbf{k}\times\mathbf{E}_l = 0$) we have above in the Laplacian term deliberately used the identity given below Eq. (3).

For longitudinal fields we now get

$$0 = \left(\omega^2 - \omega_p^2 - \beta^2 k_l^2\right)\mathbf{E}_l, \quad (7a)$$

or alternatively, pulling a factor $(\omega^2 - \beta^2 k_l^2)$ outside the parenthesis, we get

$$0 = \left(1 - \tfrac{\omega_p^2}{\omega^2-\beta^2 k_l^2}\right)\mathbf{E}_l. \quad (7b)$$

Thus, we immediately find that the non-trivial longitudinal solutions have dispersion relation $\omega(k_l) = \sqrt{\omega_p^2 + \beta^2 k_l^2}$, i.e. we exactly recover the classical solution for longitudinal bulk plasmons commonly derived from $\varepsilon_l(\omega, k_l) \equiv 0$ where $\varepsilon_l(\omega, k_l) = 1 - \omega_p^2/(\omega^2 - \beta^2 k_l^2)$.

Likewise, for transverse fields we get

$$k_t^2\mathbf{E}_t = \left(\tfrac{\omega}{c}\right)^2\left(1-\tfrac{\omega_p^2}{\omega^2}\right)\mathbf{E}_t, \quad (8)$$

so that we arrive at the common transverse dispersion relation $k_t = (\omega/c)\sqrt{\epsilon_t(\omega)}$ where $\varepsilon_t(\omega) = \varepsilon_l(\omega, k \to 0) = 1 - \omega_p^2/\omega^2$.

BOUNDARY CONDITIONS

The Eq. (2) in our Letter must be equipped with a physically appropriate boundary condition, as we discussed in Ref. [1] and more recently in detail in an appendix of Ref. [2]. This condition can be easily worked out from the continuity of the normal component of the displacement vector $\mathbf{D}$ across the boundaries, that reads:

$$\mathbf{D}_m \cdot \hat{\mathbf{n}} = \mathbf{D}_d \cdot \hat{\mathbf{n}} \qquad (9)$$

where m indicates the metal and d refers to the surrounding dielectric material. The displacement vector in the metal is defined as:

$$\mathbf{D}_m = \varepsilon_0 \varepsilon_\infty \mathbf{E} + \frac{i}{\omega}\mathbf{J}, \qquad (10)$$

where $\mathbf{J}$ is the free-electron current density. The displacement vector in the dielectric material reads:

$$\mathbf{D}_m = \varepsilon_0 \varepsilon_d \mathbf{E}, \qquad (11)$$

where ε_d is the permittivity of the surrounding material.

Equation (9) can now be rewritten as:

$$\left(\varepsilon_0 \varepsilon_\infty \mathbf{E}_m + \frac{i}{\omega}\mathbf{J} \right) \cdot \hat{\mathbf{n}} = \varepsilon_0 \varepsilon_d \mathbf{E}_d \cdot \hat{\mathbf{n}} \qquad (12)$$

Next, we impose the boundary condition $\mathbf{J} \cdot \hat{\mathbf{n}} = 0$, discussed in detail in Refs. [1, 2], which gives

$$\varepsilon_\infty \mathbf{E}_m \cdot \hat{\mathbf{n}} = \varepsilon_d \mathbf{E}_d \cdot \hat{\mathbf{n}}. \qquad (13)$$

This equation states that the normal component of the electric field is continuous across the boundaries only when interband contributions are neglected and the surrounding material is free space. Eq. (2) in our Letter is solved subject to this boundary condition. We emphasize that this is fully consistent with original requirement that $\mathbf{J} \cdot \hat{\mathbf{n}} = 0$ on the boundary.

GENERALIZED ENERGY DENSITY

In this section of our supplemental material we derive a generalized expression for the electromagnetic energy density, including the contributions stored in the hydrodynamics of the free-electron gas. We start from the Poynting theorem in time domain [3]

$$\int_S \mathbf{E} \times \mathbf{H} \cdot \hat{\mathbf{n}}\, d\mathbf{S} = -\int_V \left[\varepsilon_0 \mathbf{E} \cdot \dot{\mathbf{E}} + \mathbf{E} \cdot \dot{\mathbf{P}} + \mu_0 \mathbf{H} \cdot \dot{\mathbf{H}} \right] dV \quad (14)$$

where $\mathbf{P}$ is the polarization vector, V is the volume of the electron gas, and S is its boundary. The polarization current $\mathbf{J}$ is linked to $\mathbf{P}$ by

$$\mathbf{J} = \frac{\partial \mathbf{P}}{\partial t} = \dot{\mathbf{P}}. \qquad (15)$$

At the same time, the polarization current is related to the electric field by means of the hydrodynamic equation. In time domain, the linearized hydrodynamic Euler equation for the electron dynamics is

$$m_e \frac{\partial \mathbf{v}}{\partial t} = -\beta^2 \frac{m_e}{n_o}\nabla n - m_e \gamma \mathbf{v} - e\mathbf{E} \qquad (16)$$

where $\mathbf{v}$ is the electron velocity, n is the electron density, n_0 is the electron density at rest, and m_e the electron mass. If we introduce the polarization current $\mathbf{J} = -e n_0 \mathbf{v}$ and the charge density $\rho = -en$, the Eq. (16) becomes

$$\frac{\partial \mathbf{J}}{\partial t} = -\beta^2 \nabla \rho - \gamma \mathbf{J} + \varepsilon_0 \omega_p^2 \mathbf{E}. \qquad (17)$$

Next, if we use the definition (15), and the continuity equation $\rho = -\nabla \cdot \mathbf{P}$, we get

$$\beta^2 \nabla \nabla \cdot \mathbf{P} - \frac{\partial^2 \mathbf{P}}{\partial t^2} - \gamma \frac{\partial \mathbf{P}}{\partial t} + \varepsilon_0 \omega_p^2 \mathbf{E} = 0. \qquad (18)$$

We can now isolate $\mathbf{E}$ in this expression,

$$\mathbf{E} = -\frac{1}{\varepsilon_0 \omega_p^2}\left[\beta^2 \nabla \nabla \cdot \mathbf{P} - \frac{\partial^2 \mathbf{P}}{\partial t^2} - \gamma \frac{\partial \mathbf{P}}{\partial t} \right] \qquad (19)$$

and multiplying by $\dot{\mathbf{P}}$, we get

$$\mathbf{E} \cdot \dot{\mathbf{P}} = -\frac{1}{\varepsilon_0 \omega_p^2}\left[\beta^2 \nabla \nabla \cdot \mathbf{P} \cdot \dot{\mathbf{P}} - \frac{1}{2}\frac{d\dot{\mathbf{P}}^2}{dt} - \gamma \dot{\mathbf{P}}^2 \right]. \quad (20)$$

In the spirit of Eq. (14) we now integrate Eq. (20) over the metallic volume,

$$\int_V \mathbf{E} \cdot \dot{\mathbf{P}}\, dV = -\frac{1}{\varepsilon_0 \omega_p^2}\int_V \left[\beta^2 \nabla \nabla \cdot \mathbf{P} \cdot \dot{\mathbf{P}} - \frac{1}{2}\frac{d\dot{\mathbf{P}}^2}{dt} - \gamma \dot{\mathbf{P}}^2 \right] dV. \qquad (21)$$

Our next step is to integrate by part,

$$\int_V \nabla \nabla \cdot \mathbf{P} \cdot \dot{\mathbf{P}}\, dV = -\int_V \nabla \cdot \mathbf{P}\, \nabla \cdot \dot{\mathbf{P}}\, dV + \int_S \nabla \cdot \mathbf{P}\, \dot{\mathbf{P}} \cdot \hat{\mathbf{n}}\, d\mathbf{S}$$

To further proceed, we now apply the physical boundary condition $\mathbf{J} \cdot \hat{\mathbf{n}} = 0$ [1], i.e. no electrons leaving the metal volume. This gives

$$\int_V \nabla \nabla \cdot \mathbf{P} \cdot \dot{\mathbf{P}}\, dV = -\int_V \frac{1}{2}\frac{d(\nabla \cdot \mathbf{P})^2}{dt}\, dV.$$

In this way Eq. (21) now reads

$$\int_V \mathbf{E} \cdot \dot{\mathbf{P}}\, dV = \frac{1}{\varepsilon_0 \omega_p^2}\int_V \left[\frac{\beta^2}{2}\frac{d(\nabla \cdot \mathbf{P})^2}{dt} + \frac{1}{2}\frac{d\dot{\mathbf{P}}^2}{dt} + \gamma \dot{\mathbf{P}}^2 \right] dV \qquad (22)$$

and substituting into the Poynting theorem, Eq. (14), we get

$$\int_S \mathbf{E} \times \mathbf{H} \cdot \hat{\mathbf{n}}\, d\mathbf{S} + \int_V \frac{\gamma}{\varepsilon_0 \omega_p^2} \dot{\mathbf{P}}^2\, dV = -\int_V \dot{u}\, dV. \quad (23)$$

Here, u is the electromagnetic energy density defined as

$$u = \frac{1}{2}\varepsilon_0 \mathbf{E}^2 + \frac{\beta^2}{2\varepsilon_0 \omega_p^2}\left(\nabla \cdot \mathbf{P}\right)^2 + \frac{1}{2\varepsilon_0 \omega_p^2}\dot{\mathbf{P}}^2 + \frac{1}{2}\mu_0 \mathbf{H}^2. \quad (24)$$

Finally, if we recall the continuity equation for the polarization charge density, given by $\rho = -\nabla \cdot \mathbf{P}$, and we use Eq. (15), then

$$u = \frac{1}{2}\varepsilon_0 \mathbf{E}^2 + \frac{\beta^2}{2\varepsilon_0 \omega_p^2}\rho^2 + \frac{1}{2\varepsilon_0 \omega_p^2}\mathbf{J}^2 + \frac{1}{2}\mu_0 \mathbf{H}^2. \quad (25)$$

This is our generalization of the common energy-density to account for the energy stored in the additional degrees of freedom associated with the nonlocal hydrodynamics of the electron gas. For time harmonic fields, this expression can easily be time-averaged.

In our Letter, we focus on electrical dipole emitters where the $\mathbf{H}$ contribution can be neglected. For our accurate numerical evaluation we rely on Eqs. (1) in our Letter, i.e. an eigenvalue-problem with a six-element eigenvector $\{\mathbf{E}, \mathbf{J}\}$, rather than Eqs. (2) where one would in a subsequent (and less accurate) step have to numerically derive $\mathbf{J}$ from the obtained 3-element eigenvector $\{\mathbf{E}\}$.

NUMERICAL IMPLEMENTATION AND CONVERGENCE

In this section of our supplemental material we offer some details on the numerical implementation and the convergence tests for the waveguides that we have analyzed in our Letter. For scattering problems involving arbitrarily shaped metal geometries, Eq. (1) can be solved numerically with the aid of finite-element methods [4]. In particular, the hydrodynamic model can conveniently be integrated into commercially available software such as Comsol Multiphysics. For the scattering problem we have already made such an add-on to Comsol Multiphysics freely available [5]. Here, we extend this approach to an eigenvalue problem appropriate for waveguiding problems. Our code for solving Eq. (2) in our Letter is an add-on to Comsol Multiphysics 4.1, employing the PDE Weak form module and the standard MUMPS eigenvalue solver.

For our discussion of the numerical convergence we first note that in Fig. 2 of our Letter, the agreement between the analytical and numerical solutions is very good. More quantitatively, the relative error of the numerically calculated propagation constant k_z with respect to the analytical value is always smaller than 0.3% in the entire frequency range of Fig. 2. Likewise, the relative error for the effective mode area A_{eff} is always smaller than 0.12% within the same frequency range.

The convergence analysis for the circular nanowire waveguides is based on the methodology that we have described in previous work for the scattering problem [4]. In the present case we have two observables, i.e. the propagation constant k_z and the effective mode area A_{eff}. Thus, we define the relative errors δ_k^{num} and δ_A^{num} according to the definition $\delta_x^{\mathrm{num}} = |x_{\mathrm{mesh}} - x_{\mathrm{reg}}|/x_{\mathrm{reg}}$ where x_{mesh} is the observable value at fixed mesh edge number and x_{reg} is the value in the convergence regime. To illustrate the convergence performance we consider a relatively high frequency $\omega = 0.6\omega_p$, because in this case the field is mainly localized in the metal. This represents a "worst-case" condition for the calculations because a high number of edge elements is needed. The results are shown in Fig. S1 for a varying number η of triangular elements while we for late convenience introduce $\bar{\eta}$ as the normalized number of triangular elements. It is important to underline that the propagation constant k_z is calculated by means of the Eq. (2) in our Letter, while the mode area is calculated with Eq. (1) of our Letter, i.e. providing us with both the electrical field and the current density. As clearly seen, both codes show a convergence of the calculated parameters for $\eta > 250$. The corresponding simulation time is about 5 min for both codes. The faster convergence of Eq. (2) over Eq. (1) is also noted when comparing panels (a) and (b).

The convergence test for the V-groove is performed for the case $\lambda = 600\,\mathrm{nm}$, because it corresponds to the maximum field localization in the visible spectrum, and a high mesh density is needed. The observables are the effective refractive index n_{eff} and the propagation length L. As seen in Fig. S2, both relative errors δ_n^{num} and δ_L^{num} converge for $\bar{\eta} > 200$, and the simulation time is about 10 min. These dispersion results were calculated from Eq. (2) in our Letter.

The convergence test for the Λ-wedge structure follows the same lines. Also in this case, we show the test performed at $\lambda = 600\,\mathrm{nm}$, that corresponds to the highest field confinement in the metal. The results are shown in Fig. S3 and we notice that the propagation length converges at higher η with respect to the effective refractive index. The Λ-wedge presents high losses at this wavelength, and the simulations can be very sensitive on the mesh density. The results are obtained from Eq. (2) in our Letter, and the typical computation time is about 10 min.

Finally, we consider the convergence of the effective mode area for both V-groove and Λ-wedge. The results are shown in Fig. S4. Note that the mesh densities in the two cases are relative to different geometrical entities, so they cannot be compared directly. The results for the mode area are calculated with Eq. (1) of our Letter, i.e. providing us with both the electrical field and the current

density. The simulation time is about 10 min also in this case.

———————

[1] S. Raza, G. Toscano, A.-P. Jauho, M. Wubs, and N.A. Mortensen, Phys. Rev. B **84**, 121412(R) (2011).
[2] W. Yan, M. Wubs, and N.A. Mortensen, Phys. Rev. B **86**, 205429 (2012).
[3] R. Ruppin, Phys. Lett. A **299**, 309-312 (2002).
[4] G. Toscano, S. Raza, A.-P. Jauho, N. A. Mortensen, and M. Wubs, Opt. Express **20**, 4176 (2012).
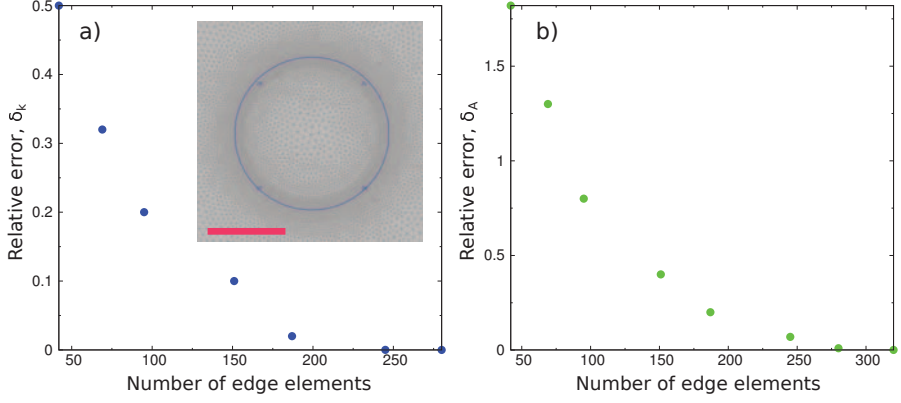[5] www.nanopl.org

FIG. 1: Convergence test for a cylindrical nanowire with radius $R = 2$ nm. Panel a) Relative error δ_k^{num} of the propagation constant k_z versus number of edge elements for cylindrical nanowires. The convergence occurs for $\eta > 200$. Panel b) Relative error δ_A^{num} of the effective mode area A_{eff} versus number of edge elements for cylindrical nanowires. The convergence occurs for $\eta > 250$. The scale bar is 1 nm long. The inset refers to $\eta = 250$.
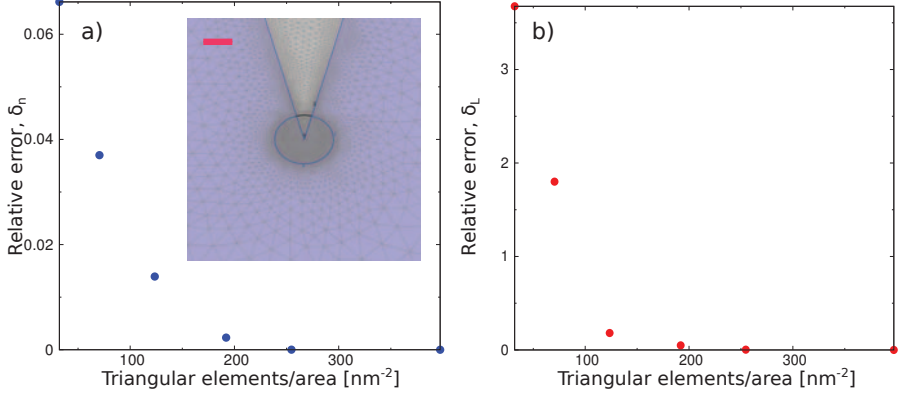

FIG. 2: Convergence test for a V-groove structure with aperture angle $\theta = 30°$. The radius of the meshing circle $R_{\text{mesh}} = 10$ nm, and it is kept constant while varying the number of triangular elements. Panel a) Relative error δ_n^{num} of the effective refractive index versus the normalized number of triangular elements $\bar{\eta}$. The convergence occurs for $\bar{\eta} > 200$, that corresponds to 6283 elements. Panel b) Relative error δ_L^{num} of the propagation length L versus $\bar{\eta}$. The convergence occurs for $\bar{\eta} > 200$. The scale bar is 10 nm long. The inset refers to $\bar{\eta} = 200$, and the shaded blue area indicates the metal.
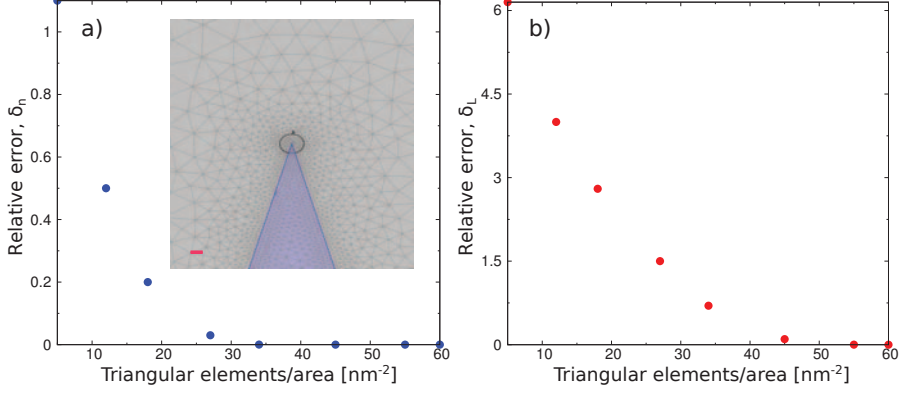
FIG. 3: Convergence test for a Λ-wedge structure with aperture angle $\theta = 30°$. The radius of the meshing circle $R_{\mathrm{mesh}} = 1\,\mathrm{nm}$, and it varies, while the number of triangular elements is kept constant. Panel a) Relative error $\delta_{\mathrm{n}}^{\mathrm{num}}$ of the effective refractive index versus the normalized number of triangular elements η. The convergence occurs for $\bar{\eta} > 30$, that corresponds to $\eta > 94$ elements. Panel b) Relative error $\delta_{L}^{\mathrm{num}}$ of the propagation length L versus $\bar{\eta}$. The convergence occurs for $\bar{\eta} > 45$, i.e. $\eta > 141$. The scale bar is $1\,\mathrm{nm}$ long. The inset refers to $\bar{\eta} = 141$, and the shaded blue area indicates the metal.
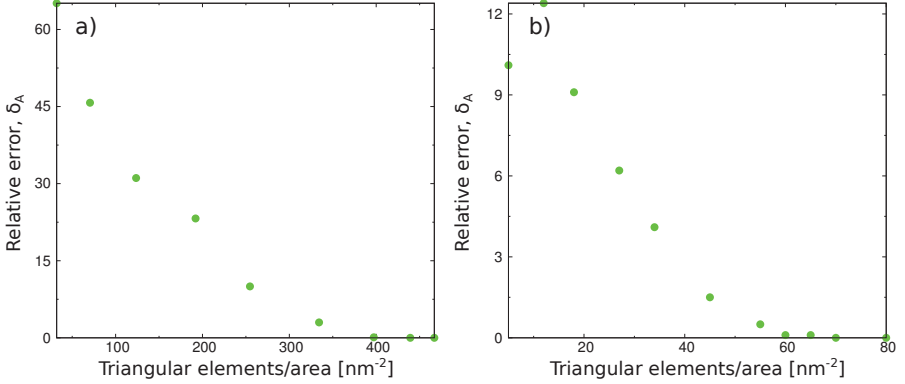

FIG. 4: Convergence test for the effective mode area for V-groove and Λ-wedge waveguides. Panel a) Relative error $\delta_{A}^{\mathrm{num}}$ of the effective mode area A_{eff} versus number of edge element for the V-groove. The convergence occurs for $\bar{\eta} > 400$, i.e. $\eta > 12566$. Panel b) Relative error $\delta_{A}^{\mathrm{num}}$ of the effective mode area A_{eff} versus number of edge elements for the Λ-wedge waveguide. The convergence occurs for $\bar{\eta} > 60$, i.e. $\eta > 188$.

Bibliography

[1] E. Abbe, "Über einen neuen beleuchtungsapparat am mikroskop," *Archiv für mikroskopische Anatomie*, vol. 9, p. 469–480, 1873.

[2] ——, "Beiträge zur theorie des mikroskops und der mikroskopischen wahrnehmung," *Archiv für mikroskopische Anatomie*, vol. 9, pp. 413–418, 1873.

[3] R. H. Ritchie, "Plasma losses by fast electrons in thin films," *Phys. Rev.*, vol. 106, p. 874, 1957.

[4] J. M. Pitarke, V. M. Silkin, E. V. Chulkov, and P. M. Echenique, "Theory of surface plasmons and surface plasmon polaritons," *Rep. Prog. Phys.*, vol. 70, pp. 1–87, 2007.

[5] C. J. Powell and J. B. Swan, "Origin of the characteristic electron energy losses in aluminum," *Phys. Rev.*, vol. 115, pp. 869–875, 1959.

[6] ——, "Origin of the characteristic electron energy losses in magnesium," *Phys. Rev.*, vol. 116, pp. 81–83, 1959.

[7] E. A. Stern and R. A. Ferrell, "Surface plasma oscillations of a degenerate electron gas," *Phys. Rev.*, vol. 120, pp. 130–136, 1960.

[8] "Beyond the diffraction limit," *Nat Photon*, vol. 3, p. 361, 2009.

[9] D. K. Gramotnev and S. I. Bozhevolnyi, "Plasmonics beyond the diffraction limit," *Nature Photonics*, vol. 4, no. 2, pp. 83–91, 2010.

[10] E. Ozbay, "Plasmonics: Merging photonics and electronics at nanoscale dimensions," *Science*, vol. 311, no. 189, pp. 189–193, 2006.

[11] H. Choo, M.-K. Kim, M. Staffaroni, T. J. Seok, J. Bokor, S. Cabrini, P. J. Schuck, M. C. Wu, and E. Yablonovitch, "Nanofocusing in a metal-insulator-metal gap plasmon waveguide with a three-dimensional linear taper," *Nat Photon*, vol. 6, pp. 838–844, 2012.

[12] S. A. Maier, *Plasmonics: Fundamentals and Applications*. Springer, 2007.

[13] M. Fox, *Optical Properties of Solids*. Oxford University Press, 2010.

[14] F. J. García de Abajo, "Nonlocal effects in the plasmons of strongly interacting nanoparticles, dimers, and waveguides," *The Journal of Physical Chemistry C*, vol. 112, no. 46, pp. 17 983–17 987, 2008.

[15] J. Zuloaga, E. Prodan, and P. Nordlander, "Quantum plasmonics: Optical properties and tunability of metallic nanorods," *ACS Nano*, vol. 4, no. 9, pp. 5269–5276, 2010.

[16] Z. Jacob and V. Shalaev, "Plasmonics goes quantum," *Science*, vol. 334, pp. 463–464, 2011.

[17] R. Esteban, A. G. Borisov, P. Nordlander, and J. Aizpurua, "Bridging quantum and classical plasmonics with a quantum-corrected model," *Nat Commun*, vol. 3, p. 825, 2012.

[18] Z. Jacob, "Quantum plasmonics," *MRS Bulletin*, vol. 37, pp. 761–767.

[19] P. Song, S. Meng, P. Nordlander, and S. Gao, "Quantum plasmonics: Symmetry-dependent plasmon-molecule coupling and quantized photoconductances," *Phys. Rev. B*, vol. 86, p. 121410, 2012.

[20] A. Manjavacas, P. Nordlander, and F. J. García de Abajo, "Plasmon blockade in nanostructured graphene," *ACS Nano*, vol. 6, no. 2, pp. 1724–1731, 2012.

[21] S. Thongrattanasiri, A. Manjavacas, and F. J. García de Abajo, "Quantum finite-size effects in graphene plasmons," *ACS Nano*, vol. 6, no. 2, pp. 1766–1775, 2012.

[22] D. Marinica, A. Kazansky, P. Nordlander, J. Aizpurua, and A. G. Borisov, "Quantum plasmonics: Nonlinear effects in the field enhancement of a plasmonic nanoparticle dimer," *Nano Letters*, vol. 12, no. 3, pp. 1333–1339, 2012.

[23] K. J. Savage, M. M. Hawkeye, R. Esteban, A. G. Borisov, J. Aizpurua, and J. J. Baumberg, "Revealing the quantum regime in tunnelling plasmonics," *Nature*, vol. 491, pp. 574–577, 2012.

[24] H. Duan, A. I. Fernández-Domínguez, M. Bosman, S. A. Maier, and J. K. W. Yang, "Nanoplasmonics: Classical down to the nanometer scale," *Nano Letters*, vol. 12, no. 3, pp. 1683–1689, 2012.

[25] J. A. Scholl, A. L. Koh, and J. A. Dionne, "Quantum plasmon resonances of individual metallic nanoparticles," *Nature*, vol. 483, pp. 421–427, 2012.

[26] J. Zuloaga, E. Prodan, and P. Nordlander, "Quantum description of the plasmon resonances of a nanoparticle dimer," *Nano Letters*, vol. 9, no. 2, pp. 887–891, 2009.

[27] F. Bloch, "Bremsvermögen von atomen mit mehreren elektronen," *Zeitschrift für Physik*, vol. 81, pp. 363–376, 1933.

[28] A. D. Boardman, *Electromagnetic Surface Modes*. John Wiley Sons Ltd, 1982.

[29] R. Fuchs and K. L. Kliewer, "Surface plasmon in a semi-infinite free-electron gas," *Phys. Rev. B*, vol. 3, pp. 2270–2278, 1971.

[30] R. Fuchs and F. Claro, "Multipolar response of small metallic spheres: Nonlocal theory," *Phys. Rev. B*, vol. 35, pp. 3722–3727, 1987.

[31] P. Halevi, *Spatial Dispersion in Solids and Plasmas*. North-Holland, 1992.

[32] S. Raza, G. Toscano, A.-P. Jauho, M. Wubs, and N. A. Mortensen, "Unusual resonances in nanoplasmonic structures due to nonlocal response," *Phys. Rev. B*, vol. 84, p. 121412(R), 2011.

[33] C. David and F. J. García de Abajo, "Spatial nonlocality in the optical response of metal nanoparticles," *The Journal of Physical Chemistry C*, vol. 115, no. 40, pp. 19 470–19 475, 2011.

[34] A. I. Fernández-Domínguez, A. Wiener, F. J. García-Vidal, S. A. Maier, and J. B. Pendry, "Transformation-optics description of nonlocal effects in plasmonic nanostructures," *Phys. Rev. Lett.*, vol. 108, p. 106802, 2012.

[35] A. Wiener, A. I. Fernández-Domínguez, A. P. Horsfield, J. B. Pendry, and S. A. Maier, "Nonlocal effects in the nanofocusing performance of plasmonic tips," *Nano Letters*, vol. 12, no. 6, pp. 3308–3314, 2012.

[36] A. Moreau, C. Ciracì, and D. R. Smith, "Impact of nonlocal response on metallodielectric multilayers and optical patch antennas," *Phys. Rev. B*, vol. 87, p. 045401, 2013.

[37] A. I. Fernández-Domínguez, Y. Luo, A. Wiener, J. B. Pendry, and S. A. Maier, "Theory of three-dimensional nanocrescent light harvesters," *Nano Letters*, vol. 12, no. 11, pp. 5946–5953, 2012.

[38] A. I. Fernández-Domínguez, P. Zhang, Y. Luo, S. A. Maier, F. J. García-Vidal, and J. B. Pendry, "Transformation-optics insight into nonlocal effects in separated nanowires," *Phys. Rev. B*, vol. 86, p. 241110, 2012.

[39] T. Dong, X. Ma, and R. Mittra, "Optical response in subnanometer gaps due to nonlocal response and quantum tunneling," *Applied Physics Letters*, vol. 101, no. 23, p. 233111, 2012.

[40] J. a. T. Costa and M. G. Silveirinha, "Macroscopic electromagnetic response of arbitrarily shaped spatially dispersive

bodies formed by metallic wires," *Phys. Rev. B*, vol. 86, p. 075129, 2012.

[41] R. T. Hill, J. J. Mock, A. Hucknall, S. D. Wolter, N. M. Jokerst, D. R. Smith, and A. Chilkoti, "Plasmon ruler with angstrom length resolution," *ACS Nano*, vol. 6, no. 10, pp. 9237–9246, 2012.

[42] K. R. Hiremath, L. Zschiedrich, and F. Schmidt, "Numerical solution of nonlocal hydrodynamic Drude model for arbitrary shaped nano-plasmonic structures using Nédélec finite elements," *Journal of Computational Physics*, vol. 231, no. 17, pp. 5890 – 5896, 2012.

[43] S. Raza, G. Toscano, A.-P. Jauho, N. Mortensen, and M. Wubs, "Refractive-index sensing with ultrathin plasmonic nanotubes," *Plasmonics*, vol. 8, no. 2, pp. 193–199, 2013.

[44] W. Yan, M. Wubs, and N. A. Mortensen, "Hyperbolic metamaterials: Nonlocal response regularizes broadband supersingularity," *Phys. Rev. B*, vol. 86, p. 205429, 2012.

[45] A. I. Fernández-Domínguez, S. A. Maier, and J. B. Pendry, "Transformation optics description of touching metal nanospheres," *Phys. Rev. B*, vol. 85, p. 165148, 2012.

[46] C. Ciracì, R. T. Hill, J. J. Mock, Y. Urzhumov, A. I. Fernández-Domínguez, S. A. Maier, J. B. Pendry, A. Chilkoti, and D. R. Smith, "Probing the ultimate limits of plasmonic enhancement," *Science*, vol. 337, no. 6098, pp. 1072–1074, 2012.

[47] G. Toscano, S. Raza, A.-P. Jauho, N. A. Mortensen, and M. Wubs, "Modified field enhancement and extinction in plasmonic nanowire dimers due to nonlocal response," *Opt. Express*, vol. 20, pp. 4176 – 4188, 2012.

[48] G. Toscano, S. Raza, S. Xiao, M. Wubs, A.-P. Jauho, S. I. Bozhevolnyi, and N. A. Mortensen, "Surface-enhanced Raman spectroscopy: nonlocal limitations," *Opt. Lett.*, vol. 37, no. 13, pp. 2538–2540, 2012.

[49] C. Ciracì, E. Poutrina, M. Scalora, and D. R. Smith, "Origin of second-harmonic generation enhancement in optical split-ring resonators," *Phys. Rev. B*, vol. 85, p. 201403, 2012.

[50] ——, "Second-harmonic generation in metallic nanoparticles: Clarification of the role of the surface," *Phys. Rev. B*, vol. 86, p. 115451, 2012.

[51] G. Toscano, S. Raza, W. Yan, C. Jeppesen, S. Xiao, M. Wubs, A.-P. Jauho, S. Bozhevolnyi, and N. Mortensen, "Nonlocal response in plasmonic waveguiding with extreme light confinement," *Nanophotonics*, vol. 2, pp. 161–166, 2013.

[52] J. Kern, S. Großmann, N. V. Tarakina, T. Häckel, M. Emmerling, M. Kamp, J.-S. Huang, P. Biagioni, J. C. Prangsma, and B. Hecht, "Atomic-scale confinement of resonant optical fields," *Nano Letters*, vol. 12, no. 11, pp. 5504–5509, 2012.

[53] H. Jensen, "Eigenschwingungen eines Fermi-gases und anwendung auf die blochsche bremsformel für schnelle teilchen," *Zeitschrift für Physik*, vol. 106, pp. 620–632, 1937.

[54] S. Lundqvist and N. H. March, *Theory of the Inhomogeneous Electron Gas.* Springer-Verlag New York, 1983.

[55] P. Drude, "Zur elektronentheorie der metalle," *Annalen der Physik*, vol. 306, no. 3, pp. 566–613, 1900.

[56] ——, "Zur elektronentheorie der metalle; II. Teil. Galvanomagnetische und thermomagnetische effecte," *Annalen der Physik*, vol. 308, no. 11, pp. 369–402, 1900.

[57] A. L. Fetter, "Electrodynamics of a layered electron gas. I. Single layer," *Annals of Physics*, vol. 81, no. 2, pp. 367 – 393, 1973.

[58] N. A. Mortensen, G. Toscano, S. Raza, N. Stenger, W. Yan, A.-P. Jauho, S. Xiao, and M. Wubs, "Nanoplasmonics beyond Ohm's law," *AIP Conference Proceedings*, vol. 1475, no. 1, pp. 28–32, 2012.

[59] L. D. Landau, L. P. Pitaevskii, and E. M. Lifshitz, *Electro-dynamics of Continuous Media*. Butterworth-Heinemann, 1984.

[60] D. Swanson, *Plasma Waves*. Taylor & Francis, 2003.

[61] R. Ruppin, "Electromagnetic energy density in a dispersive and absorptive material," *Physics Letters A*, vol. 299, pp. 309 – 312, 2002.

[62] M. S. Gockenbach, *Understanding and Implementing the Finite Element Method*. SIAM, 2006.

[63] P. B. Johnson and R. W. Christy, "Optical constants of the noble metals," *Phys. Rev. B*, vol. 6, pp. 4370–4379, 1972.

[64] R. Ruppin, "Extinction properties of thin metallic nanowires," *Optics Communications*, vol. 190, pp. 205–209, 2001.

[65] C. F. Bohren and D. R. Huffman, *Absorption and Scattering of Light by Small Particles*. Wiley-VCH, 2012.

[66] J. Smajic, C. Hafner, L. Raguin, and M. Tavzarashvili, K. Mishrikey, "Comparison of numerical methods for the analysis of plasmonic structures," *J. Comput. Theor. Nanosci*, vol. 6, no. 3, pp. 1–12, 2009.

[67] X. Cui and D. Erni, "The influence of particle shapes on the optical response of nearly touching plasmonic nanoparticle dimers," *J. Comput. Theor. Nanosci*, vol. 7, pp. 16 101–12, 2010.

[68] H. Wallén, H. Kettunen, and A. Sihvola, "Surface modes of negative-parameter interfaces and the importance of rounding sharp corners," *Metamaterials*, vol. 2, no. 2–3, pp. 113 – 121, 2008.

[69] K. Kneipp, H. Kneipp, I.Itzkan, R. R. Dasari, and M. S. Feld, "Surface-enhanced Raman scattering and biophysics," *J. Phys.: Condens. Matter*, vol. 14, pp. R597–R624, 2002.

[70] H. K. K. Kneipp, M. Moskovits, *Surface-enhanced Raman Scattering: Physics and Applications.* Springer, 2006.

[71] K. Kneipp, "Surface-enhanced Raman scattering," *Phys. Today*, vol. 60, no. 11, pp. 40–46, 2007.

[72] S. Xiao, N. A. Mortensen, and A.-P. Jauho, "Nanostructure design for surface-enhanced Raman spectroscopy - prospects and limits," *J. Europ. Opt. Soc. Rap. Public.*, vol. 3, p. 08022, 2008.

[73] F. García-Vidal and J. B. Pendry, "Collective theory for surface enhanced Raman scattering," *Phys. Rev. Lett.*, vol. 77, p. 1183, 1996.

[74] S. G. Rodrigo, F. García-Vidal, and Martín-Moreno, "Influence of material properties on extraordinary optical transmission through hole arrays," *Phys. Rev. B*, vol. 77, p. 075401, 2008.

[75] E. N. Economou, "Surface plasmons in thin films," *Phys. Rev.*, vol. 182, pp. 539–554, 1969.

[76] J. J. Burke, G. I. Stegeman, and T. Tamir, "Surface-polariton-like waves guided by thin, lossy metal films," *Phys. Rev. B*, vol. 33, pp. 5186–5201, 1986.

[77] M. Quinten, A. Leitner, J. R. Krenn, and F. R. Aussenegg, "Electromagnetic energy transport via linear chains of silver nanoparticles," *Opt. Lett.*, vol. 23, no. 17, pp. 1331–1333, 1998.

[78] S. A. Maier, P. G. Kik, H. A. Atwater, S. Meltzer, E. Harel, B. E. Koel, and A. A. Requicha, "Local detection of electromagnetic energy transport below the diffraction limit in metal nanoparticle plasmon waveguides," *Nat Mater*, vol. 2, pp. 229–232, 2003.

[79] A. F. Koenderink, "Plasmon nanoparticle array waveguides for single photon and single plasmon sources," *Nano Letters*, vol. 9, no. 12, pp. 4228–4233, 2009.

[80] J. Takahara, S. Yamagishi, H. Taki, A. Morimoto, and T. Kobayashi, "Guiding of a one-dimensional optical beam with nanometer diameter," *Opt. Lett.*, vol. 22, no. 7, pp. 475–477, 1997.

[81] P. Berini, "Plasmon-polariton waves guided by thin lossy metal films of finite width: Bound modes of asymmetric structures," *Phys. Rev. B*, vol. 63, p. 125417, 2001.

[82] R. Zia, J. A. Schuller, and M. L. Brongersma, "Near-field characterization of guided polariton propagation and cutoff in surface plasmon waveguides," *Phys. Rev. B*, vol. 74, p. 165415, 2006.

[83] E. Verhagen, A. Polman, and L. K. Kuipers, "Nanofocusing in laterally tapered plasmonic waveguides," *Opt. Express*, vol. 16, no. 1, pp. 45–57, Jan 2008.

[84] P. Berini, "Figures of merit for surface plasmon waveguides," *Opt. Express*, vol. 14, no. 26, pp. 13 030–13 042, Dec 2006.

[85] A. D. Boardman, G. C. Aers, and R. Teshima, "Retarded edge modes of a parabolic wedge," *Phys. Rev. B*, vol. 24, pp. 5703–5712, 1981.

[86] D. F. P. Pile, T. Ogawa, D. K. Gramotnev, T. Okamoto, M. Haraguchi, M. Fukui, and S. Matsuo, "Theoretical and experimental investigation of strongly localized plasmons on triangular metal wedges for subwavelength waveguiding," *Applied Physics Letters*, vol. 87, no. 6, p. 061106, 2005.

[87] A. Boltasseva, V. S. Volkov, R. B. Nielsen, E. Moreno, S. G. Rodrigo, and S. I. Bozhevolnyi, "Triangular metal wedges for subwavelength plasmon-polariton guiding at telecom wavelengths," *Opt. Express*, vol. 16, no. 8, pp. 5252–5260, Apr 2008.

[88] E. Moreno, F. J. García-Vidal, S. G. Rodrigo, L. Martín-Moreno, and S. I. Bozhevolnyi, "Channel plasmon-polaritons: modal shape, dispersion, and losses," *Opt. Lett.*, vol. 31, no. 23, pp. 3447–3449, 2006.

[89] M. Yan and M. Qiu, "Guided plasmon polariton at 2D metal corners," *J. Opt. Soc. Am. B*, vol. 24, no. 9, pp. 2333–2342, Sep 2007.

[90] I. V. Novikov and A. A. Maradudin, "Channel polaritons," *Phys. Rev. B*, vol. 66, p. 035403, 2002.

[91] D. F. P. Pile and D. K. Gramotnev, "Channel plasmon-polariton in a triangular groove on a metal surface," *Opt. Lett.*, vol. 29, no. 10, pp. 1069–1071, May 2004.

[92] D. K. Gramotnev and D. F. P. Pile, "Single-mode subwavelength waveguide with channel plasmon-polaritons in triangular grooves on a metal surface," *Applied Physics Letters*, vol. 85, no. 26, pp. 6323–6325, 2004.

[93] S. I. Bozhevolnyi, V. S. Volkov, E. Devaux, and T. W. Ebbesen, "Channel plasmon-polariton guiding by subwavelength metal grooves," *Phys. Rev. Lett.*, vol. 95, p. 046802, 2005.

[94] D. Garoli, P. Zilio, M. Natali, M. Carli, F. Enrichi, and F. Romanato, "Wedge nanostructures for plasmonic nanofocusing," *Opt. Express*, vol. 20, no. 15, pp. 16 224–16 233, 2012.

[95] A. D. Boardman, B. V. Paranjape, and Y. O. Nakamura, "Surface plasmon-polaritons in a spatially dispersive inhomogeneous medium," *phys. stat. sol. (b)*, vol. 75, no. 347, pp. 1521–3951, 1976.

[96] S. I. Bozhevolnyi and K. V. Nerkararyan, "Channel plasmon polaritons guided by graded gaps: closed-form solutions," *Opt. Express*, vol. 17, no. 12, pp. 10 327–10 334, 2009.

[97] ——, "Analytic description of channel plasmon polaritons," *Opt. Lett.*, vol. 34, no. 13, pp. 2039–2041, 2009.

[98] R. Ruppin, "Effect of non-locality on nanofocusing of surface plasmon field intensity in a conical tip," *Phys. Lett. A*, vol. 340, no. 1-4, pp. 299–302, 005.

[99] I. Villó-Pérez and N. R. Arista, "Hydrodynamical model for bulk and surface plasmons in cylindrical wires," *Surf. Sci.*, vol. 603, pp. 1–13, 2009.

[100] R. F. Oulton, G. Bartal, D. F. P. Pile, and X. Zhang, "Confinement and propagation characteristics of subwavelength plasmonic modes," *New Journal of Physics*, vol. 10, no. 10, p. 105018, 2008.

[101] S. A. Maier, "Plasmonic field enhancement and SERS in the effective mode volume picture," *Opt. Express*, vol. 14, no. 5, pp. 1957–1964, 2006.

[102] "Proceedings of the American Physical Society," *Phys. Rev.*, vol. 69, pp. 674–674, 1946.

[103] A. F. Koenderink, "On the use of Purcell factors for plasmon antennas," *Opt. Lett.*, vol. 35, no. 24, pp. 4208–4210, 2010.

[104] D. E. Chang, A. S. Sørensen, P. R. Hemmer, and M. D. Lukin, "Quantum optics with surface plasmons," *Phys. Rev. Lett.*, vol. 97, p. 053002, 2006.

[105] E. Moreno, S. G. Rodrigo, S. I. Bozhevolnyi, L. Martín-Moreno, and F. J. García-Vidal, "Guiding and focusing of electromagnetic fields with wedge plasmon polaritons," *Phys. Rev. Lett.*, vol. 100, p. 023901, 2008.

[106] J. Scholl, A. García-Etxarri, A. L. Koh, and J. A. Dionne, "Observation of quantum tunneling between two plasmonic nanoparticles," *Nano Letters*, vol. 13, no. 2, pp. 564–569, 2013.

[107] K. Andersen, K. W. Jacobsen, and K. S. Thygesen, "Spatially resolved quantum plasmon modes in metallic nano-films from first-principles," *Phys. Rev. B*, vol. 86, p. 245129, 2012.
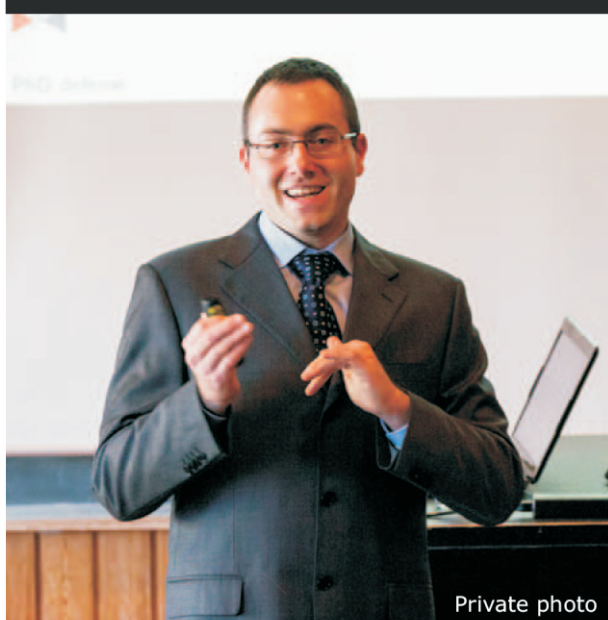
Private photo

Giuseppe Toscano is a visiting research associate at the School of Physics and Technology of Wuhan University, China. His research interest is the mathematical and numerical modeling of light-matter interactions, with a particular focus on plasmonics. He received his PhD in Physics from DTU, Technical University of Denmark. He holds a MScE in "Engineering Science" from the University of Rome "La Sapienza", and a BScE in "Electronic Engineering" from the University of Naples, "Federico" II.

DTU Fotonik
Department of Photonics Engineering